Quorum-Sensing Induced Transitions Between Bistable Steady-States for a Cell-Bulk ODE-PDE Model with Lux Intracellular Kinetics

Wesley Ridgway *, Michael J. Ward †, and Brian T. Wetton ‡

Abstract. Intercellular signaling and communication are used by bacteria to regulate a variety of behaviors. In a type of cell-cell communication known as quorum sensing (QS), which is mediated by a diffusible signaling molecule called an autoinducer, bacteria can undergo sudden changes in their behavior at a colony-wide level when the density of cells exceeds a critical threshold. In mathematical models of QS behavior, these changes can include the switch-like emergence of intracellular oscillations through a Hopf bifurcation, or sudden transitions between bistable steady-states as a result of a saddle-node bifurcation of equilibria. As an example of this latter type of QS transition, we formulate and analyze a cell-bulk ODE-PDE model in a 2-D spatial domain that incorporates the prototypical LuxI/LuxR QS system for a collection of stationary bacterial cells, as modeled by small circular disks of a common radius with a cell membrane that is permeable only to the autoinducer. By using the method of matched asymptotic expansions, it is shown that the steady-state solutions for the cell-bulk model exhibit a saddle-node bifurcation structure. The linear stability of these branches of equilibria are determined from the analysis of a nonlinear matrix eigenvalue problem, called the *globally coupled eigenvalue problem* (GCEP). The key role on QS behavior of a bulk degradation of the autoinducer field, which arises from either a Robin boundary condition on the domain boundary or from a constant bulk decay, is highlighted. With bulk degradation, it is shown analytically that the effect of coupling identical bacterial cells to the bulk autoinducer diffusion field is to create an effective bifurcation parameter that depends on the population of the colony, the bulk diffusivity, the membrane permeabilities, and the cell radius. QS transitions occur when this effective parameter passes through a saddle-node bifurcation point of the Lux ODE kinetics for an isolated cell. In the limit of a large but finite bulk diffusivity, it is shown that the cell-bulk system is well-approximated by a simpler ODE-DAE system. This reduced system, which is used to study the effect of cell location on QS behavior, is easily implemented for a large number of cells. Predictions from the asymptotic theory for QS transitions between bistable states are favorably compared with full numerical solutions of the cell-bulk ODE-PDE system.

Key Words: cell-bulk coupling, bulk diffusion, Lux kinetics, quorum-sensing, bistable states, Green's function, globally coupled eigenvalue problem.

Declarations.

Funding: Wesley Ridgway was supported by an NSERC CGS-M Fellowship as a graduate student at UBC. Michael Ward and Brian Wetton gratefully acknowledge the support of the NSERC Discovery Grant Program.

Conficts of Interest/Competing Interests: Not applicable

Ethics approval: Not applicable

Consent to Participate: Not applicable

Consent for Publication: Not applicable. All authors are aware of the submission and approve.

Availability of Data and Material: Not applicable

Code availability: Not applicable.

*Dept. of Mathematics, UBC, Vancouver, Canada. Wesley.Ridgway@maths.ox.ac.uk
†Dept. of Mathematics, UBC, Vancouver, Canada. (corresponding author ward@math.ubc.ca)
‡Dept. of Mathematics, UBC, Vancouver, Canada.

1. Introduction. Many species of bacteria use cell-cell communication, as mediated by the secretion and detection of diffusible signaling molecules called autoinducers (AI), to coordinate a variety of complex behaviors in a colony. By varying the concentration of AI, bacteria are able to adjust their behavior at a colony-wide level via alteration of gene expression. Since AI is produced by the cells, the concentration in the surrounding bulk medium acts as a measure of cell density. At small cell densities, the AI molecules are produced by the cells at a low basal rate. The concentration of AI increases as the colony grows until it reaches a critical level at which the colony undergoes a sudden switch-like transition in behavior. This process of behavioral change in response to increases in cell density is called *quorum sensing* (QS) [28, 1, 35, 33, 13].

It is convenient to distinguish between two types of QS phenomena based on their qualitative mathematical properties. The first kind is characterized by a switch-like response to oscillatory dynamical behavior where the frequency of oscillations is population dependent. Examples of such dynamical QS transitions include chemical oscillations in collections of the social amoebae *Dictyostelium discoideum* (cf. [16, 14, 31]) as well as glycolytic oscillations in colonies of starving yeast cells (cf. [7, 5, 6]). Mathematical models of this type of QS transition are characterized by a Hopf bifurcation, in which the loss of stability of a steady-state is accompanied by the emergence of oscillatory dynamics (cf. [16, 15, 19] and references therein).

Our primary focus in this paper lies in the second kind of QS, as characterized by a sudden transition to a new steady-state as the extracellular AI concentration increases past a threshold. This type of QS behavior is responsible for bioluminescence in the marine bacterium *Vibrio fischeri* (cf. [32, 21, 40, 27, 28]) as well as the production of virulence factors in the human pathogen *Pseudomonas aeruginosa* (cf. [10, 38]). Mathematical models for this type of QS transition involve the disappearance of an "off" or downregulated stable steady-state through a saddle-node bifurcation point as the cell density is increased. This leads to a rapid transition, or jump, to a new "on" or upregulated stable steady-state at some critical value of the cell density (cf. [40, 20, 9, 10, 11]). The existence of bistable steady-states and an S-shaped bifurcation diagram of equilibria, which also results in hysteretic solution behavior, is the common feature in mathematical models for this class of QS transition (see [35] for a survey). An early mathematical model of this type is given in [9] for QS transitions associated with the pathogen *Pseudomonas aeruginosa*.

Many different QS systems have been identified in a range of bacterial species (cf. [28]). However, it is known that the QS systems for gram-negative bacteria, i.e. bacteria that possess an outer cell membrane, share many common features (cf. [33]). In this paper we will focus on developing and analyzing an ODE-PDE cell-bulk model in a 2-D domain that incorporates the LuxI/LuxR QS circuit within a colony of stationary bacterial cells, as modeled by a collection of small circular disks in the domain. This circuit is the one responsible for bioluminescence in *Vibrio fischeri* (cf. [32]). Many other gram-negative bacteria have QS pathways very similar to this prototypical example, and contain counterparts to the key genes *luxI* and *luxR* (cf. [28]). Before formulating our cell-bulk ODE-PDE model in §1.2, we first introduce the LuxI/LuxR circuit as described in [20, 28, 39].

1.1. Quorum sensing and the LuxI/LuxR genetic circuit. The LuxI/LuxR circuit consists of two clusters of genes called operons, usually termed the left and right *lux* operons. The left operon contains the *luxR* gene while the right contains *luxI*, which code for the LuxR and LuxI proteins, respectively. The LuxI protein is involved in synthesizing the AI molecule N-(3-oxohexanoyl)-homoserine lactone, which is a type of acylated homoserine lactone (AHL). When the AI concentration is high enough, the LuxR proteins form a complex with the AI molecules. This LuxR-AHL complex then forms a dimer, denoted by $(\text{LuxR-AHL})_2$. The dimer causes further transcription of the genes in both operons by binding to a site lying between the operons, called the *lux* box. This genetic circuit contains a positive feedback loop since $(\text{LuxR-AHL})_2$ causes transcription of the *luxI* gene which increases production of AI, thereby forming more of the dimer $(\text{LuxR-AHL})_2$. In contrast, the right *lux* operon is involved in expression of bioluminescent behavior

(cf. [28, 39]). The genes *luxCDABE*, which are contained in the right operon, encode luciferase enzymes which are required for light production. Further, *luxI* is located just upstream from the *luxCDABE* gene cluster so that transcription of *luxI* occurs when *luxCDABE* is transcribed. In this way, the dramatic increase in AI concentration that results from the positive feedback is accompanied by a sudden transition to luminescent behavior. The existence of a second feedback loop in the LuxI/LuxR system has also been established (cf. [28]). In this feedback loop, the $(\text{LuxR-AHL})_2$ dimer also affects the production of LuxR. Recent mathematical models of the LuxI/LuxR circuit that include this second feedback loop have assumed positive feedback (cf. [40, 27, 20]).

In [20] an ODE-based model of QS for the LuxI/LuxR circuit in a single cell was formulated in terms of the intracellular concentrations of AI, LuxR, and $(\text{LuxR-AHL})_2$, and where the extracellular AI concentration was treated as a parameter. Without extracellular AI, the ODE system was shown to have either one or two stable steady-states, depending on the parameter values, which correspond to the luminescent and non-luminescent phenotypes. As the extracellular AI concentration was increased, the system can transition from having a single non-luminescent state to one possessing both states (cf. [20]). Similar results were obtained in [40] for an extended ODE model that includes the second feedback loop in the LuxI/LuxR circuit.

A significant extension of the ODE model in [40] with Lux kinetics is developed in [27] to model a colony of bacteria that are confined within a thin 3-D domain that approximates a small micro-fluidic chamber. In [27], bacteria are modeled as rod-like particles that can grow and divide, and which interact with each other via mechanical forces and through bulk chemical signaling. However, in their mixed model, the autoinducer bulk diffusion field is modeled not by a continuum-based PDE, but instead by a large collection of ODEs derived from a discrete flux balance, regulated by permeability parameters, across box-shaped spatial elements that discretize the thin 3-D domain. A Dirichlet boundary condition, allowing for loss of the autoinducer, is imposed on the outer domain boundary, as is consistent with the micro-fluidic chamber design (cf. [27]). A steady-state analysis for the Lux kinetics of an isolated cell in the absence of bulk coupling reveals bistable solution behavior for certain parameter sets. From a detailed numerical study of the mixed ODE-model, QS behavior in [27] is observed as a sudden increase in AI concentration.

As an approximation of a thin 3-D domain, we formulate and study an analytically tractable 2-D variant of the model of [27]. In our simplified theoretical framework, bacterial cells are modeled as a collection of small circular disks of a common radius where the cell membrane is permeable to the autoinducer, as regulated by permeability parameters. Within each cell, the Lux ODE kinetics of [27] is imposed, while the cell-cell chemical communication is mediated by an autoinducer bulk-diffusion field that is not discretized, but which instead satisfies a continuum-based PDE. Although our bacterial cells are assumed to be stationary, we can allow for an arbitrary number of cells centered at arbitrary, but well-separated, locations in the 2-D domain. For this ODE-PDE system, our goal is to develop a hybrid asymptotic-numerical theory to predict QS transitions between bistable steady-states in the dimensionless limit of small bacterial cell radius. Our theoretical framework is inspired by the cell-bulk ODE-PDE models that were originally introduced in [29] (see also [30]) to more realistically model bulk-diffusion induced QS transitions in 3-D cell-cell signaling. In a 2-D setting, this modeling framework of [29] has recently been used in [15] and [19] to study QS transitions involving the switch-like emergence of intracellular oscillations for a collection of cells with Sel'kov kinetics.

1.2. Formulation of the model. We now formulate our ODE-PDE cell-bulk model by recasting the system of [27] into the framework of [29, 15, 19]. The model is formulated in terms of dimensional quantities and is non-dimensionalized in Appendix A. We remark that the dependent variables in the model below are in units of concentration, whereas the model in [15] uses both concentration and mass quantities. This difference has no impact on the analysis of the dimensionless model, but is important in determining numerical values for the dimensionless parameters (see Appendix A).

Let $\Omega_L \subset \mathbb{R}^2$ be a bounded domain with a characteristic length scale of L, and suppose that there are m bacteria centered at $\mathbf{X}_1, \ldots, \mathbf{X}_m \in \Omega_L$, which we model as non-overlapping stationary disks of a common radius. We denote the jth bacterial cell with radius σ as $\Omega_{\sigma j}$, for $j = 1, \ldots, m$, so that the extracellular, or bulk, region is $\Omega_L \setminus \cup_{j=1}^m \Omega_{\sigma j}$. We let $\mathcal{U}(\mathbf{X}, T)$ denote the concentration of AI in the bulk region, where we assume AI undergoes passive diffusion with diffusion constant D_B. It is known that AHL can be degraded by lactonases (cf. [35]), so we allow for bulk decay at the rate γ_B. We assume that each cell membrane, $\partial\Omega_{\sigma j}$, for $j = 1, \ldots, m$, is permeable to AI, but not to the other chemical species (cf. [21]). The possibility of AI flux through the outer boundary, $\partial\Omega_L$, is modeled by a Robin boundary condition. In this way, the concentration of AI in the bulk region satisfies

$$\text{(1.1a)} \qquad \mathcal{U}_t = D_B \Delta_{\mathbf{X}} \mathcal{U} - \gamma_B \mathcal{U}\,, \quad \mathbf{X} \in \Omega_L \setminus \cup_{j=1}^m \Omega_{\sigma j}\,; \qquad D_B \partial_{n\mathbf{X}} \mathcal{U} + \kappa_B \mathcal{U} = 0\,, \quad \mathbf{X} \in \partial\Omega_L\,,$$

$$\text{(1.1b)} \qquad D_B \partial_{n\mathbf{X}} \mathcal{U} = p_{1j}\mathcal{U} - p_{2j} v_{1j}\,, \quad \mathbf{X} \in \partial\Omega_{\sigma j}\,, \quad \text{for} \quad j = 1, \ldots, m\,.$$

Here p_{1j} and p_{2j} are the permeabilities for the jth cell, in which the AI concentration is v_{1j}. They represent the rate at which AI molecules are absorbed and secreted, respectively. In some bacteria, such as *Vibrio fischeri*, there is no active transport system for the autoinducer across the cell membrane (cf. [21]), which implies that we should set $p_{1j} = p_{2j}$. However, active transport is present in other bacteria, such as *Pseudomonas aeruginosa* (cf. [34]). Hence, we retain p_{1j} and p_{2j} as model parameters. In (1.1), the unit normal points either out of Ω_L or out of $\Omega_{\sigma j}$ on the appropriate boundaries.

Within the jth cell, we assume that there are n chemical species with concentrations denoted by $\mathbf{v}_j \equiv (v_{1j}, \ldots, v_{nj})^T$. These species are assumed to be well-mixed and undergo reactions according to

$$\text{(1.2)} \qquad \frac{\mathrm{d}\mathbf{v}_j}{\mathrm{d}T} = k_R v_c \mathbf{F}_j(\mathbf{v}_j/v_c) + \mathbf{e}_1 \int_{\partial\Omega_{\sigma j}} (p_{1j}\mathcal{U} - p_{2j} v_{1j})\, ds_{\mathbf{X}}\,, \quad \text{for} \quad j = 1, \ldots, m\,,$$

where $\mathbf{e}_1 \equiv (1, 0, \ldots, 0)^T$. Here, the vector field $\mathbf{F}_j$ describes the reaction kinetics within the jth cell as if it was isolated completely from the bulk region. The integral source term in (1.2) and the boundary condition in (1.1b) represent the exchange of AI across the cell membrane. The constants v_c and k_R represent a characteristic concentration and reaction rate of the intracellular kinetics, respectively.

In Appendix A we non-dimensionalize the ODE-PDE system (1.1) and (1.2) to obtain the following PDE diffusion equation for the dimensionless extracellular AI concentration, denoted by $U(\mathbf{x}, t)$:

$$\text{(1.3a)} \qquad U_t = D\Delta U - \gamma U\,, \quad \mathbf{x} \in \Omega \setminus \cup_{j=1}^m \Omega_{\varepsilon_j}\,; \qquad D\partial_n U + \kappa U = 0\,, \quad \mathbf{x} \in \partial\Omega\,,$$

$$\text{(1.3b)} \qquad \varepsilon D \partial_n U = d_{1j} U - d_{2j} u_{1j}\,, \quad \mathbf{x} \in \partial\Omega_{\varepsilon_j}\,, \quad \text{for} \quad j = 1, \ldots, m\,,$$

where $\gamma \geq 0$ and $\kappa \geq 0$. Here, $\Omega \equiv \Omega_1$ and $\varepsilon \equiv \sigma/L$. We will assume that $\varepsilon \ll 1$, so that the cells are much smaller than the $\mathcal{O}(1)$ length-scale of the domain Ω. The dimensionless ODEs within the cells are

$$\text{(1.4)} \qquad \frac{\mathrm{d}\mathbf{u}_j}{\mathrm{d}t} = \mathbf{F}_j(\mathbf{u}_j) + \mathbf{e}_1 \varepsilon^{-1} \int_{\partial\Omega_{\varepsilon j}} (d_{1j} U - d_{2j} u_{1j})\, ds_{\mathbf{x}}\,, \quad \text{for} \quad j = 1, \ldots, m\,.$$

The ε-dependent scalings in both the membrane boundary condition in (1.3b) and in the boundary integral in (1.4) are required for an $\mathcal{O}(1)$ coupling effect, without which the cells would behave as if they were isolated and QS behavior would not occur. The ODE system in (1.4), coupled indirectly through the bulk medium by (1.3), is of dimension $nm + 1$.

In the analysis below, we will consider a special case of (1.3) and (1.4) where the reaction kinetics are given by the Lux ODE system in [27]. A dimensionless Lux system in the jth cell with bulk coupling, as

derived in Appendix A from the dimensional model in [27], is given by

$$\frac{\mathrm{d}u_{1j}}{\mathrm{d}t} = c + \frac{\kappa_{1A}u_{4j}}{\kappa_{DA}+u_{4j}} - \kappa_{2A_j}u_{1j} - u_{1j}u_{2j} + \kappa_5 u_{3j} + \varepsilon^{-1}\int_{\partial\Omega_{\varepsilon_j}} (d_{1j}U - d_{2j}u_{1j})\, ds_{\mathbf{x}}\,, \tag{1.5a}$$

$$\frac{\mathrm{d}u_{2j}}{\mathrm{d}t} = 1 + \frac{\kappa_{1R}u_{4j}}{\kappa_{DR}+u_{4j}} - \kappa_{2R}u_{2j} - u_{1j}u_{2j} + \kappa_5 u_{3j}\,, \tag{1.5b}$$

$$\frac{\mathrm{d}u_{3j}}{\mathrm{d}t} = u_{1j}u_{2j} - \kappa_5 u_{3j} - 2\kappa_3 u_{3j}^2 + 2\kappa_4 u_{4j}\,, \qquad \frac{\mathrm{d}u_{4j}}{\mathrm{d}t} = \kappa_3 u_{3j}^2 - \kappa_4 u_{4j}\,, \tag{1.5c}$$

where u_{1j}, u_{2j}, u_{3j}, and u_{4j} are the dimensionless concentrations of AI, LuxR, LuxR-AHL, and (LuxR-AHL)$_2$, respectively. All parameters in (1.5) are positive, while κ_{2A_j} in (1.5a) can be cell-dependent.

The interpretation of the reaction kinetics in (1.5) modeling the LuxI/LuxR genetic circuit follows from [27] (see Fig. 1.1 for a schematic). Both AI and LuxR are produced at a (dimensionless) basal rate of c and 1, respectively. These rates represent the level of production at low cellular concentrations when the *lux* box is empty (cf. [40]). The AI molecules bind to LuxR proteins and form an AHL-LuxR complex with a dimensionless reaction rate of unity. The (AHL-LuxR)$_2$ dimers are formed at a rate κ_3 from the (AHL-LuxR) complexes. The dimers bind to the *lux* box, which stimulates the production of LuxR and AI by initiating transcription of the two *lux* operons. This positive feedback of the (AHL-LuxR)$_2$ dimer on the production of AI and LuxR is captured by the rational terms in (1.5a) and (1.5b), whose precise forms are motivated in [40, 20]. The stimulus is assumed to be proportional to the fraction of time that the *lux* box is occupied by (AHL-LuxR)$_2$, which in turn depends on the concentration of (AHL-LuxR)$_2$ in such a way that it is linear at low concentrations while saturating at high concentrations. The remaining terms in (1.5) represent degradation of the various species through breakdown, dilution, and reversible reaction.

In [29, 15, 19] no flux boundary conditions on $\partial\Omega$ were imposed. The motivation here for including the Robin boundary condition on $\partial\Omega$ in (1.3a) is both biological and mathematical. The effect of absorbing and reflecting boundaries on QS behavior has been studied both experimentally and mathematically (cf. [37, 25]), where it was shown that different boundary types can have a significant impact on steady-state AI concentration and also QS behavior. From a mathematical viewpoint, our analysis will show that QS transitions are not possible for our model without bulk loss terms, for which $\gamma = \kappa = 0$ in (1.3a).

The outline of the paper is as follows. In §2 we calculate the steady-states and analyze their stability properties for the Lux ODE system (1.5) of [27] for an isolated cell with no bulk coupling. This analysis, similar to that in [27], shows the existence of bistability and the possibility of a transition between a down-regulated and an upregulated steady-state as the intracellular AI coefficient, κ_{2A}, is varied. For arbitrary intracellular kinetics, in §3 we use strong localized perturbation theory in the limit $\varepsilon \to 0$ to construct steady-state solutions to the cell-bulk model (1.3) and (1.4). In addition, we both derive and discuss some qualitative results from the GCEP characterizing the linear stability properties of these steady-states. The construction of steady-state solutions and the GCEP is accurate to all orders of ν. However, to provide analytical insight into the role of a bistable intracellular kinetics, as is relevant to the Lux kinetics, in §3.3 we derive and interpret leading-order-in-ν results for the steady-states and their linear stability properties. In §4 we apply the theory of §3 to the Lux kinetics (1.5) both with and without bulk degradation. With bulk degradation, we show analytically that the effect of coupling identical bacterial cells to the bulk autoinducer diffusion field is to create an effective bifurcation parameter that depends on the population of the colony, the bulk diffusivity, the membrane permeabilities, and the cell radius. QS transitions occur when this effective parameter passes through a saddle-node point of the Lux ODE kinetics for an isolated cell. In §5 we simplify the steady-state and linear stability analysis for the large bulk diffusivity regime $D = \mathcal{O}(\nu^{-1}) \gg 1$. For this regime in D, where we obtain simplified QS criteria, we derive a reduced ODE-DAE system that

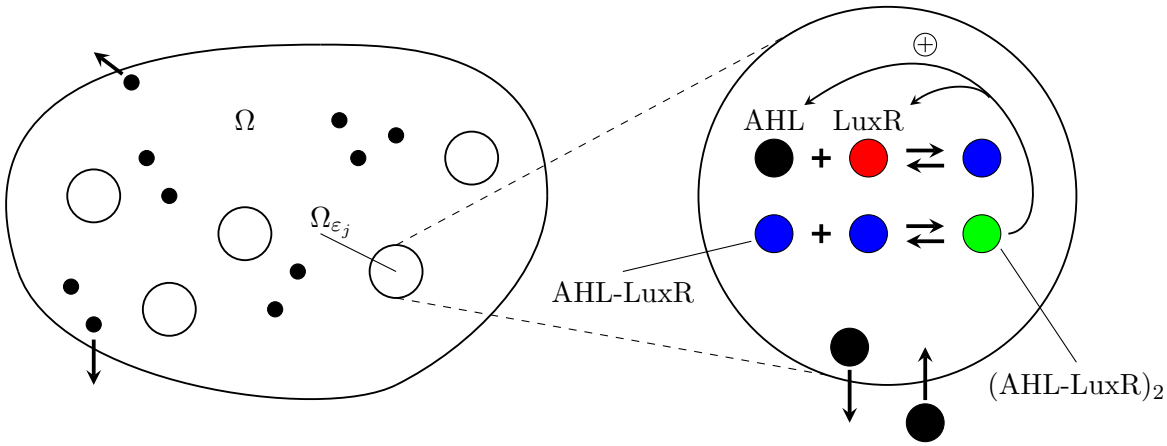

Figure 1.1: Schematic diagram depicting the model geometry and intracellular reactions. The circular regions on the left are cells, while the black dots represent AI molecules. The chemical reactions described by (1.5) occur in each cell, as depicted in the magnified cell on the right. The diffusible AHL molecules that are secreted and absorbed by the cells undergo bulk decay and are allowed to leak out of the bulk domain.

well-approximates the solutions to the cell-bulk ODE-PDE model (1.3) and (1.4). With this reduced ODE-DAE system, which is readily implemented for a large number of cells, we study the effect of cell locations on QS behavior. Throughout this paper, for the special case where the confining domain Ω is a disk, the asymptotic predictions for QS transitions are confirmed from full numerical solutions of the cell-bulk model (1.3)–(1.5).

2. The LUX ODE system with no bulk coupling. We first analyze the steady-states for the Lux reaction kinetics (1.5) for an isolated cell with no coupling to the bulk medium. This analysis provides a point of comparison when we analyze the full coupled cell-bulk model. In particular, we show below that this coupling effectively changes the value of κ_{2A}, causing it to depend on the bulk parameters. As a result, in our ODE analysis of an isolated cell, κ_{2A} is chosen as the bifurcation parameter.

With no bulk coupling, we suppress the cell index j below for clarity, and from (1.5) we obtain

$$\text{(2.1a)} \qquad \frac{\mathrm{d}u_1}{\mathrm{d}t} = c + \frac{\kappa_{1A}u_4}{\kappa_{DA}+u_4} - \kappa_{2A}u_1 - u_1u_2 + \kappa_5 u_3\,, \qquad \frac{\mathrm{d}u_3}{\mathrm{d}t} = u_1u_2 - \kappa_5 u_3 - 2\kappa_3 u_3^2 + 2\kappa_4 u_4\,,$$

$$\text{(2.1b)} \qquad \frac{\mathrm{d}u_2}{\mathrm{d}t} = 1 + \frac{\kappa_{1R}u_4}{\kappa_{DR}+u_4} - \kappa_{2R}u_2 - u_1u_2 + \kappa_5 u_3\,, \qquad \frac{\mathrm{d}u_4}{\mathrm{d}t} = \kappa_3 u_3^2 - \kappa_4 u_4\,.$$

Denoting the steady-states of (2.1) by u_{je}, for $j = 1, \ldots, 4$, we readily calculate from (2.1) that

$$\text{(2.2)} \qquad u_{3e} = \frac{1}{\kappa_5}u_{1e}u_{2e}\,, \quad u_{4e} = \frac{\kappa_3}{\kappa_4}u_{3e}^2\,, \quad u_{1e} = \frac{1}{\kappa_{2A}}\left[c + \frac{\kappa_{1A}u_{3e}^2}{\kappa_{DA}\frac{\kappa_4}{\kappa_3} + u_{3e}^2}\right]\,, \quad u_{2e} = \frac{1}{\kappa_{2R}}\left[1 + \frac{\kappa_{1R}u_{3e}^2}{\kappa_{DR}\frac{\kappa_4}{\kappa_3} + u_{3e}^2}\right]\,.$$

Then, upon substituting these expressions for u_{1e} and u_{2e} into that for u_{3e}, we obtain that u_{3e} satisfies the nonlinear algebraic equation $q(u_{3e}) = 0$, defined by

$$\text{(2.3)} \quad q(u_{3e}) \equiv \frac{1}{\kappa_{2A}\kappa_{2R}\kappa_5}\left(c + \frac{\kappa_{1A}u_{3e}^2}{\kappa_A + u_{3e}^2}\right)\left(1 + \frac{\kappa_{1R}u_{3e}^2}{\kappa_R + u_{3e}^2}\right) - u_{3e}\,, \quad \text{where} \quad \kappa_A \equiv \kappa_{DA}\frac{\kappa_4}{\kappa_3}\,, \quad \kappa_R \equiv \kappa_{DR}\frac{\kappa_4}{\kappa_3}\,.$$

It follows that u_{3e} is determined by the roots of a quintic polynomial. As such, there must be at least one real root to $q(u_{3e}) = 0$. This root is positive since $q(0) > 0$, $q(u) \to -\infty$ as $u \to \infty$, and q is continuous. This steady-state construction for a rescaled version of (2.1) was given previously in [27].

The linear stability properties of each steady-state solution $\boldsymbol{u}_e \equiv (u_{1e}, u_{2e}, u_{3e}, u_{4e})^T$ of (2.1) is determined by the eigenvalues λ of of the Jacobian matrix, J_e, given by

$$J_e = \begin{pmatrix} -\kappa_{2A} - u_{2e} & -u_{1e} & \kappa_5 & \frac{\kappa_{1A}\kappa_{DA}}{(\kappa_{DA}+u_{4e})^2} \\ -u_{2e} & -\kappa_{2R} - u_{1e} & \kappa_5 & \frac{\kappa_{1R}\kappa_{DR}}{(\kappa_{DR}+u_{4e})^2} \\ u_{2e} & u_{1e} & -\kappa_5 - 4\kappa_3 u_{3e} & 2\kappa_4 \\ 0 & 0 & 2\kappa_3 u_{3e} & -\kappa_4 \end{pmatrix}. \tag{2.4}$$

Upon setting $\det(\lambda I - J_e) = 0$, we obtain the characteristic polynomial $\lambda^4 + a_3\lambda^3 + a_2\lambda^2 + a_1\lambda + a_0 = 0$ where, by using Leverrier-Faddeev algorithm [18], the coefficients are $a_0 = \det(J_e)$ and

$$a_1 = -\frac{1}{6}\left[(\mathrm{tr}(J_e))^3 - 3\mathrm{tr}\left(J_e^2\right)\mathrm{tr}(J_e) + 2\mathrm{tr}\left(J_e^3\right)\right], \quad a_2 = \frac{1}{2}\left[(\mathrm{tr}(J_e))^2 - \mathrm{tr}\left(J_e^2\right)\right], \quad a_3 = -\mathrm{tr}(J_e). \tag{2.5}$$

The steady-state $\boldsymbol{u}_e$ for (2.1) is linearly stable if and only if all the eigenvalues of J_e satisfy $\mathrm{Re}(\lambda) < 0$. From the *Routh-Hurwitz criterion* for a quartic polynomial, it follows that all eigenvalues of J_e satisfy $\mathrm{Re}(\lambda) < 0$ if and only if the coefficients in the characteristic polynomial satisfy

$$a_3 > 0, \qquad \det(J_e) > 0, \qquad a_3a_2 - a_1 > 0, \qquad (a_3a_2 - a_1)a_1 - a_3^2\det(J_e) > 0. \tag{2.6}$$

To illustrate the bifurcation structure for steady-state solutions of (2.1) as κ_{2A} is varied, we numerically determine the roots u_{3e} of (2.3) using the continuation software MATCONT [8]. Then, (2.2) yields the bifurcation structure for u_{4e}, u_{1e}, and u_{2e}. At each value of κ_{2A} the Routh-Hurwitz criterion (2.6) is used to examine the linear stability properties of the steady-state.

These bifurcation diagrams are shown in the top row of Fig. 2.1 for the parameter set in [27] but rescaled into our dimensionless form, as given in Table 1 of Appendix A. The saddle-node bifurcations correspond, as expected, to a zero-crossing for one of the eigenvalues of the Jacobian J_e. From the top row of Fig. 2.1, we observe that all of the branches have a double hysteresis structure. However, in the bifurcation diagrams for both u_{1e} and u_{2e} one of these structures possesses two hairpin-like fold points. Although it may appear otherwise from the first two panels of the top row of Fig. 2.1, these fold points are smooth in κ_{2A} owing to the fact that u_{3e} depends smoothly on κ_{2A} while both u_{1e} and u_{2e} depend smoothly on u_{3e} as is evident from (2.2). Due to the hairpin structure, the branches for u_{1e} and u_{2e} both behave as a single biological switch. In particular, it is the lower hysteresis structure that causes switch-like behavior for u_{1e}. This transition corresponds to the upper hysteresis structure for u_{2e}. We will focus primarily on the lower hysteresis structure for u_{1e} when we analyze the ODE-PDE cell-bulk model. As shown in the lower row of Fig. 2.1 the two hysteresis structures can be separated by modifying κ_{DR} to $\kappa_{DR} = 0.0125$. For this value, there are at most three equilibria for any value of κ_{2A}.

In Fig. 2.2a we plot the numerical solution to the Lux ODE system (2.1) when κ_{2A} is slowly ramped in time as in Fig. 2.2b through all the saddle-node bifurcation points in the top row of Fig. 2.1. We observe from Fig. 2.2a that the numerical solution to (2.1) tracks the quasi steady-states, as obtained by solving $q(u_{3e}) = 0$ in (2.3) and then using (2.2), as κ_{2A} is varied until there is a sudden, but delayed, transition as κ_{2A} is ramped past the saddle-node points. This delayed bifurcation behavior is typical for slow passage problems in ODEs (cf. [24]). As expected, the autoinducer concentration, u_1, has a switch-like response corresponding to the lower hysteresis structure shown in the top row of Fig. 2.1.

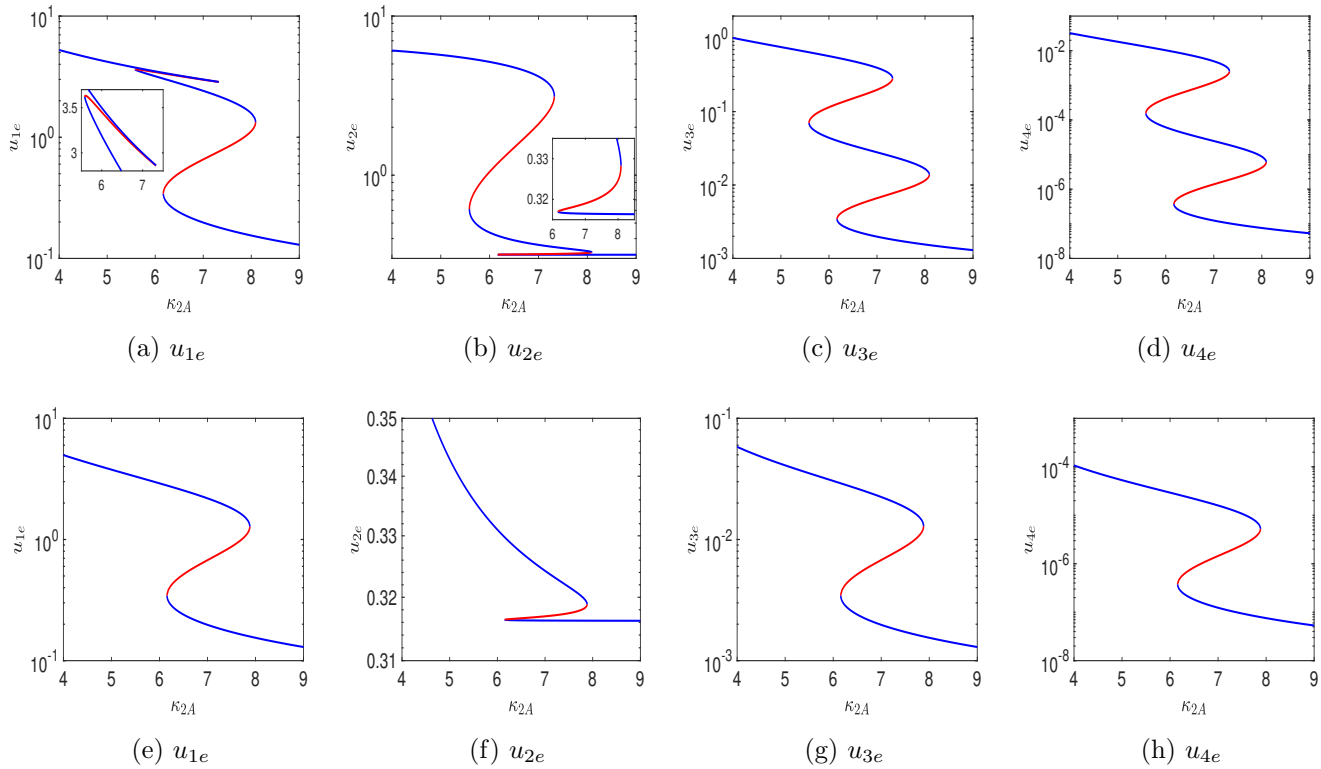

(a) u_{1e} (b) u_{2e} (c) u_{3e} (d) u_{4e}

(e) u_{1e} (f) u_{2e} (g) u_{3e} (h) u_{4e}

Figure 2.1: Top row: Bifurcation diagrams for the steady-states of the Lux ODE system in (2.1), as computed from (2.2) and (2.3), with the parameters in Table 1. The hairpin fold bifurcations are magnified for clarity. Blue and red portions represent linearly stable and unstable steady-state solution branches, respectively. Bottom row: same plot but now with $\kappa_{DR} = 0.0125$, so that the hysteresis structures are separated.

Our analysis below will focus on studying how the cell-bulk coupling modifies the switch-like response due to the saddle-node bifurcations observed in Fig. 2.1. In contrast to the analysis in [15, 19] where oscillatory instabilities are triggered by cell-bulk coupling for Sel'kov intracellular reaction kinetics, in Appendix B of [36] it was shown that there can be no Hopf bifurcations associated with steady-states of the Lux ODE kinetics (2.1) for the parameters used in [27].

3. The cell-bulk model for $D = \mathcal{O}(1)$: Steady states and linear stability. For the $D = \mathcal{O}(1)$ regime, in this section we use the method of matched asymptotic expansions in the limit $\varepsilon \to 0$ to construct the steady-states of the cell-bulk model (1.3) and (1.4) and to derive a globally coupled eigenvalue problem (GCEP) characterizing the linear stability properties of the steady-state solutions. When there is a degradation process in the bulk, corresponding to either $\gamma > 0$ or $\kappa > 0$, the steady-state and linear stability analysis parallels that given in [15, 19] and so we only summarize the main results for this case. Instead we focus on the modifications of the analysis in [15, 19] needed to treat the case where there is no bulk loss mechanism, for which $\gamma = \kappa = 0$. For a collection of identical cells, in §3.3 we perform a two-term perturbation analysis in ν in order to gain analytical insight into the role of a bistable reaction kinetics $\mathbf{F}(\mathbf{u})$ on the asymptotic construction of steady-state solutions and their linear stability properties.

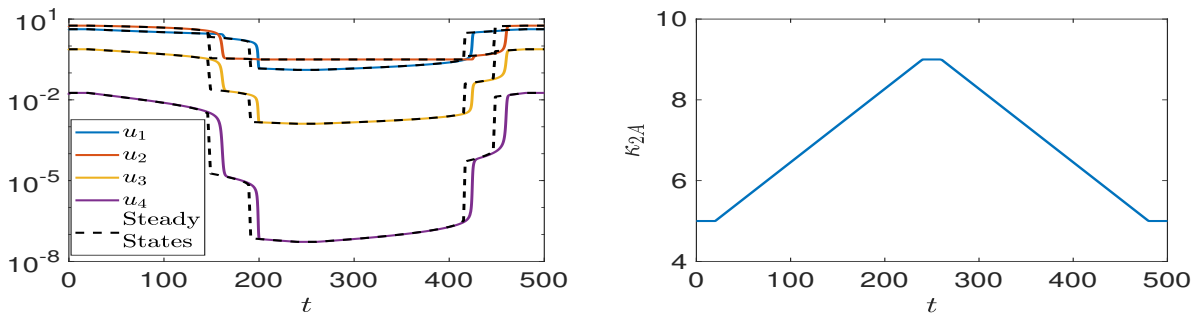

(a) u_j versus t

(b) κ_{2a} versus t

Figure 2.2: Numerical solution of (2.1) (left panel) when the bifurcation parameter κ_{2A} is ramped slowly in time as in the right panel for the parameters in the top row of Fig. 2.1. Observe that there is a sudden, but delayed, transition between the steady-states as the parameter κ_{2A} is slowly ramped through the fold points.

3.1. Steady-state solutions. We assume that the cells are well-separated in the sense that $|\mathbf{x}_i - \mathbf{x}_j| = \mathcal{O}(1)$ for all $i \neq j$ and $\text{dist}(\mathbf{x}_j, \partial\Omega) = \mathcal{O}(1)$ as $\varepsilon \to 0$. We now construct steady-state solutions for (1.3) and (1.4) that are accurate to all orders in $\nu \equiv -1/\log\varepsilon$.

Within an $\mathcal{O}(\varepsilon)$ inner region near the jth cell we define the inner variables $\mathbf{y}_j \equiv \varepsilon^{-1}(\mathbf{x} - \mathbf{x}_j)$, $\rho \equiv |\mathbf{y}_j|$, and $U_j(\mathbf{y}_j) = U(\mathbf{x}_j + \varepsilon\mathbf{y}_j)$. From the steady-state problem for (1.3), we obtain to leading order that $\Delta_{\mathbf{y}_j} U_j = 0$ for $\rho \geq 1$, subject to $D\,\partial_\rho U_j = d_{1j}U_j - d_{2j}u_{1j}$ on $\rho = 1$. Here $\Delta_{\mathbf{y}_j}$ is the Laplacian in the inner variable. In terms of constants S_j, for $j = 1, \ldots, m$, to be found, the radially symmetric solution is

$$U_j(\rho) = S_j \log\rho + \frac{1}{d_{1j}}\left(D\,S_j + d_{2j}u_{1j}\right), \qquad j = 1, \ldots, m, \tag{3.1}$$

Upon substituting (3.1) into (1.4) we obtain the nonlinear algebraic system

$$\mathbf{F}_j(\mathbf{u}_j) + 2\pi D S_j \mathbf{e}_1 = \mathbf{0}, \quad \text{for} \quad j = 1, \ldots, m, \quad \text{where} \quad \mathbf{e}_1 \equiv (1, 0, \ldots, 0)^T. \tag{3.2}$$

The far-field behavior of the inner solution (3.1), when written in the outer variable, imposes a specific singularity structure as $\mathbf{x} \to \mathbf{x}_j$ for the steady-state outer bulk solution in terms of the logarithmic gauge $\nu \equiv -1/\log\varepsilon \ll 1$. When there is no bulk loss, i.e. $\gamma = \kappa = 0$, we obtain from (3.1) and the steady-state problem for (1.3), that this outer solution satisfies

$$\begin{gathered} \Delta U = 0, \quad \mathbf{x} \in \Omega \setminus \{\mathbf{x}_1, \ldots, \mathbf{x}_m\}; \qquad \partial_n U = 0, \quad \mathbf{x} \in \partial\Omega; \\ U \sim S_j \log|\mathbf{x} - \mathbf{x}_j| + \frac{S_j}{\nu} + \frac{1}{d_{1j}}(DS_j + d_{2j}u_{1j}), \quad \text{as} \quad \mathbf{x} \to \mathbf{x}_j, \quad j = 1, \ldots, m. \end{gathered} \tag{3.3}$$

The divergence theorem yields $\sum_{j=1}^m S_j = 0$, and when this condition holds we can represent U as

$$U = -2\pi \sum_{i=1}^m S_i G_N(\mathbf{x}; \mathbf{x}_i) + \overline{U}, \tag{3.4}$$

where $\overline{U} \equiv |\Omega|^{-1}\int_\Omega U d\mathbf{x}$ is the unknown spatial average of U over Ω. Here $G_N(\mathbf{x}; \mathbf{x}_i)$ is the Neumann

Green's function with regular part R_{Ni}, which is defined uniquely in terms of the area $|\Omega|$ of Ω by

$$\begin{aligned} &\Delta G_N = \frac{1}{|\Omega|} - \delta(\mathbf{x}-\mathbf{x}_i)\,, \quad \mathbf{x}\in\Omega\,; \qquad \partial_n G_N = 0\,, \quad \mathbf{x}\in\partial\Omega\,; \\ &G_N(\mathbf{x};\mathbf{x}_i) = -\frac{1}{2\pi}\log|\mathbf{x}-\mathbf{x}_i| + R_{Ni} + o(1)\,, \quad \text{as} \quad \mathbf{x}\to\mathbf{x}_i\,; \qquad \int_\Omega G_N\,\mathrm{d}\mathbf{x} = 0\,. \end{aligned} \tag{3.5}$$

To determine a linear algebraic system for $S_1,\ldots,S_m$ and $\overline{U}$, we simply enforce the matching condition that (3.4) agrees, as $\mathbf{x}\to\mathbf{x}_j$ and for each $j=1,\ldots,m$, with the pre-specified regular part of each singularity structure in (3.3). In matrix form, these constraints yield that

$$(I + 2\pi\nu\mathcal{G}_N + \nu D\mathcal{D}_1)\,\mathbf{S} = -\nu\mathcal{D}_{21}\mathbf{u}^1 + \nu\overline{U}\mathbf{e}\,, \qquad \mathbf{e}^T\mathbf{S} = \mathbf{0}\,, \tag{3.6}$$

where $\mathbf{S}\equiv(S_1,\ldots,S_m)^T$. In (3.6), the diagonal matrices $\mathcal{D}_1$ and $\mathcal{D}_{21}$, the vectors $\mathbf{e}$ and $\mathbf{u}^1$, and the entries $(\mathcal{G}_N)_{ij}$ of the Neumann Green's matrix $\mathcal{G}_N$ are defined by

$$(\mathcal{G}_N)_{ij} \equiv G_N(\mathbf{x}_i;\mathbf{x}_j) \quad i\neq j\,; \qquad (\mathcal{G}_N)_{ii} \equiv R_{Ni}\,; \qquad \mathbf{e}\equiv(1,\ldots,1)^T\,, \tag{3.7a}$$

$$\mathcal{D}_1 \equiv \mathrm{diag}\left(\frac{1}{d_{11}},\ldots,\frac{1}{d_{1m}}\right)\,, \qquad \mathcal{D}_{21} \equiv \mathrm{diag}\left(\frac{d_{21}}{d_{11}},\ldots,\frac{d_{2m}}{d_{1m}}\right)\,; \qquad \mathbf{u}^1 \equiv (u_{11},\ldots,u_{1m})^T\,. \tag{3.7b}$$

By taking an inner product with $\mathbf{e}$ in (3.6) we can then use the solvability condition $\mathbf{e}^T\mathbf{S}=0$ to isolate $\overline{U}$. Upon substituting the resulting expression for $\overline{U}$ back into (3.6) we obtain an algebraic system for $\mathbf{S}$ in terms of $\mathbf{u}^1$. Together with (3.2) this leads to an $m(n+1)$ dimensional *nonlinear algebraic system* (NAS) for $\mathbf{S}$ and $\mathbf{u}_j$, for $j=1,\ldots,m$. We summarize this steady-state construction as follows:

Principal Result 1. *In the limit $\varepsilon\to 0$, and assuming that there is no bulk degradation, i.e. $\gamma=\kappa=0$, the steady-states for the cell-bulk model (1.3) in the outer bulk region are given by (3.4) with $\overline{U} = m^{-1}\mathbf{e}^T\left[(2\pi\mathcal{G}_N + D\mathcal{D}_1)\,\mathbf{S} + \mathcal{D}_{21}\mathbf{u}^1\right]$, where $\mathbf{S}\equiv(S_1,\ldots,S_m)^T$ and the steady-state intracellular species $\mathbf{u}_j$ for $j=1,\ldots,m$ satisfy the NAS*

$$[I + \nu D\,(I-E)\,\mathcal{D}_1 + 2\pi\nu\,(I-E)\,\mathcal{G}_N]\,\mathbf{S} = -\nu\,(I-E)\,\mathcal{D}_{21}\mathbf{u}^1\,, \quad \textit{where} \quad E\equiv\frac{1}{m}\mathbf{e}\mathbf{e}^T\,, \tag{3.8a}$$

$$\mathbf{F}_j(\mathbf{u}_j) + 2\pi D S_j\mathbf{e}_1 = \mathbf{0}\,, \quad j=1,\ldots,m\,. \tag{3.8b}$$

Here $\mathcal{G}_N$, $\mathcal{D}_1$, $\mathcal{D}_{21}$, $\mathbf{e}$, and $\mathbf{u}^1$ are as defined in (3.7).

When the cells are identical, i.e. $d_{1j}=d_1$, $d_{2j}=d_2$, and $\mathbf{F}_j=\mathbf{F}$, for $j=1,\ldots,m$, then (3.8) becomes

$$\left[I + \nu\frac{D}{d_1}\,(I-E) + 2\pi\nu\,(I-E)\,\mathcal{G}_N\right]\mathbf{S} = -\nu\frac{d_2}{d_1}\,(I-E)\,\mathbf{u}^1\,, \quad \mathbf{F}(\mathbf{u}_j) + 2\pi D S_j\mathbf{e}_1 = \mathbf{0}\,, \tag{3.9}$$

for $j=1,\ldots,m$. For identical cells, and when there exists a $\mathbf{u}_c$ with $\mathbf{F}(\mathbf{u}_c)=0$, then (3.9) has a solution with $\mathbf{u}^1 = u_{c1}\mathbf{e}$ so that $(I-E)\mathbf{u}^1=\mathbf{0}$, and consequently $\mathbf{S}=\mathbf{0}$ from (3.9). This corresponds to a branch of steady-state solutions that are identical to that without any bulk coupling. Moreover, when $\mathbf{S}=\mathbf{0}$ we obtain from (3.4), together with the expression for $\overline{U}$ in Principal Result 1, that $U=\overline{U}=d_2/(d_1u_{c1})$ in the outer region. For this solution branch we conclude that there is no flux of AI into or out of any of the cells and that the steady-states are not only independent of the number, m, of cells, but also independent of all bulk parameters. The existence of such a solution branch for identical cells holds for arbitrary kinetics. Although this strongly hints that no QS behavior can occur on this branch, we must first consider the stability properties of the steady-states, as is done below in §3.2.

Alternatively, when there is a bulk loss mechanism, corresponding to either $\gamma>0$ or $\kappa>0$ in (1.3), the steady-state analysis parallels that in [19] and is summarized as follows:

Principal Result 2. *In the limit $\varepsilon \to 0$, and assuming that either $\gamma > 0$ or $\kappa > 0$, the steady-states for the cell-bulk model (1.3) in the outer bulk region are given by*

$$U = -2\pi \sum_{i=1}^{m} S_i G(\mathbf{x}; \mathbf{x}_i)\,, \tag{3.10}$$

where G is the reduced-wave Green's function with regular part R_i satisfying

$$\begin{gathered} \Delta G - \frac{\gamma}{D} G = -\delta(\mathbf{x} - \mathbf{x}_i)\,, \quad \mathbf{x} \in \Omega\,; \qquad D\partial_n G + \kappa G = 0\,, \quad \mathbf{x} \in \partial\Omega\,, \\ G(\mathbf{x}; \mathbf{x}_i) = -\frac{1}{2\pi} \log|\mathbf{x} - \mathbf{x}_i| + R_i + o(1) \quad \text{as} \quad \mathbf{x} \to \mathbf{x}_i\,. \end{gathered} \tag{3.11}$$

Here $\mathbf{S} \equiv (S_1, \ldots, S_m)^T$ and the steady-state intracellular species $\mathbf{u}_j$ satisfy the NAS

$$(I + \nu D \mathcal{D}_1 + 2\pi\nu\mathcal{G})\,\mathbf{S} = -\nu \mathcal{D}_{21} \mathbf{u}^1\,, \qquad \mathbf{F}_j(\mathbf{u}_j) + 2\pi D S_j \mathbf{e}_1 = 0\,, \quad j = 1, \ldots, m\,, \tag{3.12}$$

where $\mathcal{D}_1$ and $\mathcal{D}_{21}$ are defined in (3.7b). The Green's matrix $\mathcal{G}$ is defined analogously to $\mathcal{G}_N$ as in (3.7a). For the case of identical cells, (3.12) reduces to

$$\left[\left(1 + \nu \frac{D}{d_1}\right) I + 2\pi\nu\mathcal{G}\right] \mathbf{S} = -\nu \frac{d_2}{d_1} \mathbf{u}^1\,, \qquad \mathbf{F}(\mathbf{u}_j) + 2\pi D S_j \mathbf{e}_1 = \mathbf{0}\,, \quad j = 1, \ldots, m\,. \tag{3.13}$$

The simplest pattern to analyze for the identical cell case with bulk degradation is when Ω is the unit disk and the cells are equally-spaced on a concentric ring within the disk. In this case, where $\mathbf{e}$ is an eigenvector of $\mathcal{G}$, there is a solution branch where $\mathbf{S} = S_c \mathbf{e}$ (with nonzero S_c) and $\mathbf{u}_j = u_c \mathbf{e}$ for $j = 1, \ldots, m$. In §4, we will consider these solution branches in detail for the Lux kinetics.

3.2. The linear stability problem. Next, we derive the *globally coupled eigenvalue problem* (GCEP) characterizing the linear stability of the steady-state solutions in Principal Results 1–2. We begin by introducing a perturbation from the steady-states U_e and $\mathbf{u}_{je}$ as

$$U = U_e(\mathbf{x}) + \eta(\mathbf{x}) e^{\lambda t}\,, \qquad \mathbf{u}_j = \mathbf{u}_{je} + \mathbf{w}_j e^{\lambda t}\,, \quad j = 1, \ldots, m\,. \tag{3.14}$$

Upon substituting (3.14) into (1.3) and (1.4) and linearizing, we obtain the eigenvalue problem

$$\lambda\eta = D\Delta\eta - \gamma\eta\,, \quad \mathbf{x} \in \Omega \setminus \cup_{j=1}^{m} \Omega_{\varepsilon_j}\,, \qquad D\partial_n \eta + \kappa\eta = 0\,, \quad \mathbf{x} \in \partial\Omega\,, \tag{3.15a}$$

$$\varepsilon D \partial_n \eta = d_{1j}\eta - d_{2j} w_{1j}\,, \quad \mathbf{x} \in \partial\Omega_{\varepsilon_j}\,, \quad j = 1, \ldots, m\,, \tag{3.15b}$$

$$\lambda \mathbf{w}_j = J_j \mathbf{w}_j + \mathbf{e}_1 \varepsilon^{-1} \int_{\partial\Omega_{\varepsilon_j}} (d_{1j}\eta - d_{2j} w_{1j})\, ds_{\mathbf{x}}\,, \quad \text{for} \quad j = 1, \ldots, m\,, \tag{3.15c}$$

where $J_j \equiv \mathbf{F}_{j\mathbf{u}}(\mathbf{u}_{je})$ denotes the Jacobian of $\mathbf{F}_j$ evaluated at $\mathbf{u}_{je}$.

The singular perturbation analysis of (3.15) as $\varepsilon \to 0$ is similar to that given in [15, 19] and leads to the following characterization for the linear stability properties of the steady-state solutions:

Principal Result 3. *In the limit $\varepsilon \to 0$, we obtain for (3.15) that in the outer bulk region, and within each cell, the perturbations in (3.14) satisfy*

$$\eta = -2\pi \sum_{i=1}^{m} c_i G_\lambda(\mathbf{x}; \mathbf{x}_i)\,, \qquad \mathbf{w}_j = -2\pi D c_j (J_j - \lambda I)^{-1} \mathbf{e}_1\,, \quad \text{for} \quad j = 1, \ldots, m\,, \tag{3.16}$$

provided that λ is not an eigenvalue of J_j for any $j = 1, \ldots, m$. Here the eigenvalue-dependent Green's function G_λ and its regular part $R_{\lambda i}$ satisfy

$$\Delta G_\lambda - \frac{(\gamma+\lambda)}{D} G_\lambda = -\delta(\mathbf{x}-\mathbf{x}_i)\,, \quad \mathbf{x}\in\Omega\,; \qquad D\partial_n G_\lambda + \kappa G = 0\,, \quad \mathbf{x}\in\partial\Omega\,, \tag{3.17}$$
$$G_\lambda(\mathbf{x};\mathbf{x}_i) = -\frac{1}{2\pi}\log|\mathbf{x}-\mathbf{x}_i| + R_{\lambda i} + o(1) \quad \text{as} \quad \mathbf{x}\to\mathbf{x}_i\,.$$

Then, λ is an approximation as $\varepsilon \to 0$ to a discrete eigenvalue of the linearization (3.15) if and only if there is a nontrivial solution $\mathbf{c} \equiv (c_1, \ldots, c_m)^T \neq \mathbf{0}$ to the GCEP, defined by

$$\mathcal{M}(\lambda)\mathbf{c} = \mathbf{0}\,, \qquad \text{where} \qquad \mathcal{M}(\lambda) \equiv I + \nu D\mathcal{D}_1 + 2\pi\nu D\mathcal{D}_{21}\mathcal{K}(\lambda) + 2\pi\nu\mathcal{G}_\lambda\,. \tag{3.18a}$$

Such nontrivial solutions occur if and only if λ satisfies $\det\mathcal{M}(\lambda) = 0$. The set $\Lambda(\mathcal{M})$ of all such roots is

$$\Lambda(\mathcal{M}) \equiv \{\lambda \,|\, \det\mathcal{M}(\lambda) = 0\}\,. \tag{3.18b}$$

In (3.18a), $\nu \equiv -1/\log\varepsilon$, the diagonal matrices $\mathcal{D}_1$ and $\mathcal{D}_{21}$ are defined in (3.7b), the Green's matrix $\mathcal{G}_\lambda$ is defined analogously to $\mathcal{G}_N$ as in (3.7a), and the diagonal matrix $\mathcal{K}(\lambda) \equiv diag(\mathcal{K}_1(\lambda), \ldots, \mathcal{K}_m(\lambda))$ is defined in terms of the Jacobians J_j of the intracellular kinetics by

$$\mathcal{K}_j = \mathbf{e}_1^T(\lambda I - J_j)^{-1}\mathbf{e}_1 = \frac{M_{j,11}}{\det(\lambda I - J_j)}\,; \qquad M_{j,11} \equiv \det\begin{pmatrix} \lambda - \frac{\partial F_{2j}}{\partial u_{2j}}\Big|_{\mathbf{u}_j=\mathbf{u}_{je}} & \cdots & -\frac{\partial F_{2j}}{\partial u_{nj}}\Big|_{\mathbf{u}_j=\mathbf{u}_{je}} \\ \vdots & \ddots & \vdots \\ -\frac{\partial F_{nj}}{\partial u_{2j}}\Big|_{\mathbf{u}_j=\mathbf{u}_{je}} & \cdots & \lambda - \frac{\partial F_{nj}}{\partial u_{nj}}\Big|_{\mathbf{u}_j=\mathbf{u}_{je}} \end{pmatrix}. \tag{3.18c}$$

The GCEP defined by (3.18), in which $\mathcal{M}$ is a symmetric but non-Hermitian matrix when $\lambda \in \mathbb{C}$, is a nonlinear matrix eigenvalue problem for λ. Numerical solution strategies for special classes of nonlinear matrix eigenvalue problems arising in various applications are discussed in [17, 3].

We remark that $\mathcal{M}(\lambda)$ in (3.18a) is not defined at $\lambda = 0$ for the case $\gamma = \kappa = 0$ when there is no bulk degradation. For this special case, and setting $\lambda = 0$, we can readily derive in place of (3.16) that

$$\eta = -2\pi\sum_{i=1}^{m} c_i G_N(\mathbf{x};\mathbf{x}_i) + \overline{\eta}\,, \qquad J_j\mathbf{w}_j = -2\pi D c_j \mathbf{e}_1\,, \quad \text{for} \quad j = 1, \ldots, m\,, \tag{3.19}$$

where G_N is the Neumann Green's function of (3.5). Here $\mathbf{c} \equiv (c_1, \ldots, c_m)^T$ and the constant $\overline{\eta}$ satisfy

$$(I + 2\pi\nu\mathcal{G}_N + \nu D\mathcal{D}_1)\,\mathbf{c} + \nu\mathcal{D}_{21}\mathbf{w}^1 = \nu\overline{\eta}\,, \qquad \mathbf{e}^T\mathbf{c} = 0\,, \tag{3.20}$$

where $\mathbf{w}^1 \equiv (w_{11}, \ldots, w_{1m})^T$ and $\mathcal{G}_N$ is the Neumann Green's matrix. Under the assumption that J_j is invertible for $j = 1, \ldots, m$, we obtain from (3.19) and (3.18c) that $\mathbf{w}^1 = 2\pi D\mathcal{K}(0)\mathbf{c}$, where $\mathcal{K}(0) = -\text{diag}\left(\mathbf{e}_1^T J_1^{-1}\mathbf{e}_1, \ldots, \mathbf{e}_1^T J_m^{-1}\mathbf{e}_1\right)$. Then, upon eliminating $\overline{\eta}$ in (3.20) by using the constraint $\mathbf{e}^T\mathbf{c} = 0$, we conclude that $\lambda = 0$ is an eigenvalue of (3.15) under the assumption of no bulk degradation ($\gamma = \kappa = 0$) if and only if there is a nontrivial solution $\mathbf{c} \neq 0$ to

$$\mathcal{M}_0\mathbf{c} = \mathbf{0}\,, \qquad \text{where} \qquad \mathcal{M}_0 \equiv I + \nu D(I-E)\mathcal{D}_1 + 2\pi\nu D(I-E)\mathcal{D}_{21}\mathcal{K}(0) + 2\pi\nu(I-E)\mathcal{G}_N\,. \tag{3.21}$$

Based on the GCEP formulation in (3.18) and (3.21), a specific criterion for the linear stability of a steady-state solution of (1.3) and (1.4), and the relationship between zero-eigenvalue crossings and the local solvability of the NAS in (3.12) and (3.8) with and without bulk degradation, respectively, can be established as in the proof of Proposition 1 of [19] for the case where $\kappa = 0$. Our result is as follows:

Principal Result 4. *For $\varepsilon \to 0$, a steady-state solution to (1.3) and (1.4) as characterized in Principal Result 2 and 1 with and without bulk degradation, respectively, is linearly stable if and only if for all $\lambda \in \Lambda(\mathcal{M})$ we have $Re(\lambda) < 0$. With bulk degradation, then for any non-degenerate solution $\mathbf{S}_e$ and $\mathbf{u}_{ej}$, for $j = 1, \ldots, m$, of (3.12), for which the Jacobians J_j for $j = 1, \ldots, m$ are non-singular, we have that $\lambda = 0 \notin \Lambda(\mathcal{M})$. Similarly, with no bulk degradation, then for any non-degenerate solution $\mathbf{S}_e$ and $\mathbf{u}_{ej}$, for $j = 1, \ldots, m$, to (3.8), we have $\det \mathcal{M}_0 \neq 0$ in (3.21), so that $\lambda = 0$ is not an eigenvalue of (3.15).*

The proof of this result in [19] regarding zero-crossings for the case of bulk degradation follows by observing that the Jacobian associated with linearizing the NAS (3.12) around a solution is the GCEP matrix $\mathcal{M}(0)$ in (3.18a) for $\lambda = 0$. For a non-degenerate solution this Jacobian is non-singular and so $\det \mathcal{M}(0) \neq 0$ and $\lambda = 0 \notin \Lambda(\mathcal{M})$. A similar argument applies for the case of no bulk degradation.

Principal Result 4 implies that an instability of a steady-state for (1.3) and (1.4) as parameters are varied can only occur via a Hopf bifurcation, for which $\lambda = i\lambda_I$ with $\lambda_I > 0$, or at bifurcation points for the NAS (3.12) and (3.8). Based our the analysis in §2 of the Lux ODE dynamics for an isolated cell, where no Hopf bifurcations can occur (cf. [36]), we expect that zero-eigenvalue crossings for the GCEP will be associated with saddle-node bifurcation points of the NAS (3.12).

Next, we observe that the eigenvalues λ of the GCEP in (3.18) are $\mathcal{O}(\nu)$ close to those of the cell Jacobians J_j, for $j = 1, \ldots, m$. To show this, it is convenient to define the matrices $\mathcal{S}(\lambda)$ and $\hat{\mathcal{M}}(\lambda)$ by

$$\begin{aligned} \mathcal{S}(\lambda) &\equiv \operatorname{diag}\left(\det(\lambda I - J_1), \ldots, \det(\lambda I - J_m)\right) , \\ \hat{\mathcal{M}}(\lambda) &\equiv \mathcal{S}(\lambda)\mathcal{M}(\lambda) = \mathcal{S}(\lambda)\left(I + \nu D\mathcal{D}_1 + 2\pi\nu\mathcal{G}_\lambda\right) + 2\pi D\nu\mathcal{D}_{21}\mathcal{M}_{11}(\lambda) , \end{aligned} \tag{3.22}$$

where $\mathcal{M}_{11} \equiv \operatorname{diag}(M_{1,11}, \ldots, M_{m,11})$ with $M_{j,11}$ as defined in (3.18c). We observe that $\det \mathcal{M}$ and $\det \hat{\mathcal{M}}$ have exactly the same zeros since the zeros of $\det \mathcal{S}$, corresponding to the eigenvalues of J_j, are not zeros of $\det \hat{\mathcal{M}}$. Moreover, $\det \hat{\mathcal{M}}$ has no poles, which we will make use of below in §4.3. If we neglect the $\mathcal{O}(\nu)$ terms of $\hat{\mathcal{M}}$, including those in the Jacobian arising from $\mathcal{O}(\nu)$ perturbations of the steady-state, then to leading order in ν we have $\det \hat{\mathcal{M}} \sim \det \mathcal{S}$. Therefore, to leading order in ν any eigenvalue of J_j (evaluated at an unperturbed steady-state), is also an eigenvalue of the GCEP. We emphasize that this does not, in general, hold to all orders in ν. However, for the special case where there is no bulk degradation, for which $\gamma = \kappa = 0$, we can establish the following stronger result for a collection of identical cells.

Lemma 3.1. *Suppose there is no bulk degradation and that $\mathbf{u}_e$ is a steady-state of the common ODE reaction kinetics $d\mathbf{u}/dt = \mathbf{F}(\mathbf{u})$ within each cell when it is uncoupled from the bulk, i.e. $\mathbf{F}(\mathbf{u}_e) = 0$. Assume that the Jacobian $J_e \equiv \mathbf{F}_\mathbf{u}(\mathbf{u}_e)$ is singular with a one-dimensional nullspace spanned by $\mathbf{w}_\star$. Then, the GCEP associated with linearization around the $\mathbf{S} \equiv \mathbf{0}$ solution of the NAS (3.8) admits a zero-eigenvalue, which is valid to all orders in ν. The corresponding eigenfunction for (3.15) is $\mathbf{w}_j = \mathbf{w}_\star$ for $j = 1, \ldots, m$ and $\eta = (d_2/d_1)w_{1\star}$, where $w_{1\star}$ is the first component of $\mathbf{w}_\star$.*

Proof. For the identical cell case, we have along the $\mathbf{S} = \mathbf{0}$ solution branch of the NAS (3.8) that $\mathbf{u}_j = \mathbf{u}_e$ for all $j = 1, \ldots, m$, so that the Jacobians J_j are simply the Jacobians of the isolated cells, i.e. $J_j = J_e \equiv \mathbf{F}_\mathbf{u}(\mathbf{u}_e)$ for each $j = 1, \ldots, m$. Thus, to establish that $\lambda = 0$ is an eigenvalue of the cell-bulk problem, it suffices to show the existence of a nontrivial solution to (3.20) when $\mathcal{D}_1 = d_1^{-1}I$, $\mathcal{D}_{21} = (d_2/d_1)I$, where $\mathbf{w}_j$ satisfies $J_e\mathbf{w}_j = -2\pi Dc_j\mathbf{e}_1$ for all $j = 1, \ldots, m$. This solution is given by $c_j = 0$ and $\mathbf{w}_j = \mathbf{w}_\star$, for $j = 1, \ldots, m$, and $\eta = (d_2/d_1)w_{1,\star}$, where $w_{1,\star}$ is the first component of $\mathbf{w}_\star$. ∎

With no bulk degradation, this result establishes that a zero-eigenvalue crossing for the linearization of the ODE reaction kinetics for a collection of identical, but isolated cells, also occurs to all orders in ν for the linearization (3.15) of the coupled cell-bulk model.

3.3. Perturbation theory in ν for bistable kinetics. As we have shown in §2, the Lux ODE kinetics (2.1) for an isolated cell exhibit bistable behavior. In order to gain analytical insight into how this bistable behavior is perturbed by the cell-bulk coupling, we now consider the case of identical cells with an arbitrary bistable reaction kinetics $\mathbf{F}(\mathbf{u})$ and develop an explicit two-term perturbation expansion in ν for the steady-state solutions for the cell-bulk system, as characterized by the NAS in (3.12) and (3.8) with and without bulk degradation, respectively. For these solutions, a two-term expansion in ν for the GCEP (3.18) will explicitly characterize the linear stability properties of these steady-states.

We assume that the common ODE reaction kinetics $d\mathbf{u}/dt = \mathbf{F}(\mathbf{u})$ within an isolated cell has two steady-states; an "on" or "upregulated" state" denoted by $\mathbf{u}_+$ and an "off" or "downregulated" state labeled by $\mathbf{u}_-$, so that $\mathbf{F}(\mathbf{u}_\pm) = \mathbf{0}$. When the cells are isolated from the bulk, we assume that there are $m_+ \geq 0$ cells in the on state $\mathbf{u}_+$, with cell indices $j = 1, \ldots, m_+$, and $m_- \geq 0$ cells in the off state $\mathbf{u}_-$, corresponding to the cell indices $j = m_+ + 1, \ldots, m$, where $m_- + m_+ = m$. We assume below that the cell Jacobians $\hat{J}_\pm \equiv \mathbf{F}_\mathbf{u}(\mathbf{u}_\pm)$ are non-singular, so that we are not at a zero-eigenvalue crossing for the linearization of the reaction-kinetics at the two possible steady-states $\mathbf{u}_\pm$ of an isolated cell.

With cell-bulk coupling, and assuming no bulk degradation, we observe from the NAS in (3.8) that for $\nu \ll 1$ we have $\mathbf{S} = \mathcal{O}(\nu)$, $\mathbf{u}_j = \mathbf{u}_+ + \mathcal{O}(\nu)$ for $j = 1, \ldots, m_+$, and $\mathbf{u}_j = \mathbf{u}_- + \mathcal{O}(\nu)$ for $j = m_+ + 1, \ldots, m$. By expanding the solution to the NAS (3.8) in powers of ν, we obtain after some algebra that

$$\mathbf{u}_j = \begin{cases} \mathbf{u}_+ + 2\pi D\nu \frac{d_2}{d_1}\left(u_{1+} - u_{1-}\right)\frac{m_-}{m}\hat{J}_+^{-1}\mathbf{e}_1 + \mathcal{O}(\nu^2)\,, & j = 1, \ldots, m_+\,, \\ \mathbf{u}_- - 2\pi D\nu \frac{d_2}{d_1}\left(u_{1+} - u_{1-}\right)\frac{m_+}{m}\hat{J}_-^{-1}\mathbf{e}_1 + \mathcal{O}(\nu^2)\,, & j = m_+ + 1, \ldots, m\,, \end{cases} \tag{3.23a}$$

$$\mathbf{S} = -\nu\frac{d_2}{d_1}(I - E)\left[I - \nu\left(\frac{D}{d_1}I + 2\pi D\frac{d_2}{d_1}\mathcal{K}_0 + 2\pi\mathcal{G}_N\right)(I - E)\right]\hat{\mathbf{u}}^1 + \mathcal{O}(\nu^3)\,, \tag{3.23b}$$

where $E \equiv m^{-1}\mathbf{e}\mathbf{e}^T$ and

$$\mathcal{K}_0 \equiv -\mathrm{diag}\left(\mathbf{e}_1^T\hat{J}_1^{-1}\mathbf{e}_1, \ldots, \mathbf{e}_1^T\hat{J}_m^{-1}\mathbf{e}_1\right)\,, \qquad \hat{\mathbf{u}}^1 \equiv (u_{11}, \ldots, u_{1m})^T\,. \tag{3.23c}$$

In (3.23c), $\hat{J}_j^{-1} \equiv \hat{J}_+^{-1}$ and $u_{1j} = u_{1+}$ for $j = 1, \ldots, m_+$, while $\hat{J}_j^{-1} \equiv \hat{J}_-^{-1}$ and $u_{1j} = u_{1-}$ for $j = m_+ + 1, \ldots, m$. Here $\hat{J}_\pm \equiv \mathbf{F}_\mathbf{u}(\mathbf{u}_\pm)$ are the cell Jacobians and $u_{1\pm}$ is the first component of $\mathbf{u}_\pm$.

We observe from (3.23b) that $\mathbf{e}^T\mathbf{S} = 0$ as required by the solvability condition in (3.6) when there is no bulk loss. Moreover, we observe from the presence of the Neumann Green's matrix $\mathcal{G}_N$ in (3.23b) that the cell locations have only an $\mathcal{O}(\nu^2)$ influence on the source strengths $\mathbf{S}$.

A two-term asymptotic result, similar to that in (3.23), can be derived from the NAS (3.12) when there is bulk degradation. In terms of the Neumann Green's matrix $\mathcal{G}$, we obtain that

$$\mathbf{u}_j = \begin{cases} \mathbf{u}_+ + 2\pi D\nu\frac{d_2}{d_1}(u_{1+})\hat{J}_+^{-1}\mathbf{e}_1 + \mathcal{O}(\nu^2)\,, & j = 1, \ldots, m_+\,, \\ \mathbf{u}_- + 2\pi D\nu\frac{d_2}{d_1}(u_{1-})\hat{J}_-^{-1}\mathbf{e}_1 + \mathcal{O}(\nu^2)\,, & j = m_+ + 1, \ldots, m\,, \end{cases} \tag{3.24a}$$

$$\mathbf{S} = -\nu\frac{d_2}{d_1}\left[I - \nu\left(\frac{D}{d_1}I + 2\pi D\frac{d_2}{d_1}\mathcal{K}_0 + 2\pi\mathcal{G}\right)\right]\hat{\mathbf{u}}^1 + \mathcal{O}(\nu^3)\,. \tag{3.24b}$$

Next, we gain analytical insight into the linear stability of these steady-states by calculating a two-term expansion in ν for the eigenvalues of λ of the GCEP (3.18). For $\nu \ll 1$, we observe from (3.18) that $\mathcal{M}(\lambda) = I + \mathcal{O}(\nu)$, unless λ is $\mathcal{O}(\nu)$ close to an eigenvalue of the cell Jacobian J_j, in which case we have $\nu\mathcal{K} = \mathcal{O}(1)$ in (3.18). As a result, for $\nu \ll 1$, an eigenvalue of the GCEP, which satisfies $\det\mathcal{M}(\lambda) = 0$, must be $\mathcal{O}(\nu) \ll 1$ close an eigenvalue of J_j. With bistable reaction kinetics, we how derive a two-term expansion

for the eigenvalues λ of the GCEP (3.18) that are $\mathcal{O}(\nu)$ close to simple eigenvalues $\sigma_\pm$ of the cell Jacobians $\hat{J}_\pm$ for an isolated cell. In the GCEP matrix in (3.18a), the Jacobians J_j in $\mathcal{K}(\lambda)$, as defined in (3.18c), are to be evaluated at the solutions of the NAS (3.12) and (3.8) that, to all orders in ν, characterize the steady-states of the coupled cell-bulk model. Therefore for $\nu \ll 1$, we must expand

$$J_j = \begin{cases} \hat{J}_+ + \mathcal{O}(\nu)\,, & j = 1, \ldots, m_+\,, \\ \hat{J}_- + \mathcal{O}(\nu)\,, & j = m_+ + 1, \ldots, m\,, \end{cases} \tag{3.25}$$

so that, to leading order in ν, $\mathcal{K}(\lambda)$ in (3.18c) reduces to

$$\mathcal{K}(\lambda) \sim \hat{\mathcal{K}}(\lambda) \equiv \text{diag}\left(\mathbf{e}_1^T \left(\lambda I - \hat{J}_+\right)^{-1} \mathbf{e}_1, \ldots, \mathbf{e}_1^T \left(\lambda I - \hat{J}_-\right)^{-1} \mathbf{e}_1 \right)\,, \tag{3.26}$$

where the first m_+ elements involve $\hat{J}_+$ and the remaining involve $\hat{J}_-$. From (3.26), we conclude that $\nu\mathcal{K}(\lambda) = \mathcal{O}(1)$ when $\lambda = \sigma_\pm + \mathcal{O}(\nu)$, where $\sigma_\pm$ are simple eigenvalues of $\hat{J}_\pm$. As a result, when $\lambda = \sigma_\pm + \mathcal{O}(\nu)$, the GCEP matrix in (3.18a) can be approximated by

$$\mathcal{M}(\lambda)\mathbf{c} = \mathbf{0}\,, \qquad \text{where} \quad \mathcal{M}(\lambda) \sim I + 2\pi D\nu(d_2/d_1)\hat{\mathcal{K}}(\lambda) + \mathcal{O}(\nu)\,. \tag{3.27}$$

To analyze this limiting problem more precisely, we introduce the resolvent $R_\pm(z)$ of $\hat{J}_\pm$, which is singular at each eigenvalue of $\hat{J}_\pm$. Near a simple eigenvalue $\sigma_\pm$ of $\hat{J}_\pm$, $R_\pm(z)$ has the Laurent expansion

$$R_\pm(z) \equiv \left(zI - \hat{J}_\pm\right)^{-1} = \frac{P_{-1}^\pm}{z - \sigma_\pm} + \sum_{i=0}^{\infty} (z - \sigma_\pm)^i \, P_i^\pm\,, \qquad \text{as} \quad z \to \sigma_\pm\,, \tag{3.28}$$

which is defined in terms of certain matrices $P_i^\pm$ that, in principle, can be calculated explicitly (cf. [22]).

We first consider the eigenvalue σ_+ of $\hat{J}_+$, and we assume that σ_+ is not also an eigenvalue of $\hat{J}_-$. Then, by setting $z = \lambda$ in (3.28), we let $\lambda \to \sigma_+$ to obtain from (3.28) and (3.26) that

$$\hat{\mathcal{K}}(\lambda) \sim \frac{\mathbf{e}_1^T P_{-1}^+ \mathbf{e}_1}{\lambda - \sigma_+} I_+ + \cdots\,, \qquad \text{with} \quad I_+ \equiv \text{diag}(\underbrace{1, 1, \ldots, 1, 1}_{\leftarrow m_+ \text{ terms} \rightarrow}, 0, 0 \ldots, 0, 0)\,. \tag{3.29}$$

Then, by substituting $\lambda \sim \sigma_+ + \nu\sigma_1 + \ldots$ in (3.29), we obtain that the limiting GCEP (3.27) becomes

$$\left(I + 2\pi D \frac{d_2}{d_1} \frac{\mathbf{e}_1^T P_{-1}^+ \mathbf{e}_1}{\sigma_1} I_+ + \mathcal{O}(\nu) \right) \mathbf{c} = \mathbf{0}\,, \tag{3.30}$$

which has the eigenvector $\mathbf{c} = (\mathbf{c}_+, \mathbf{0})^T$, with $\mathbf{c}_+ \in \mathbb{R}^{m_+}$, if and only if $\sigma_1 = -2\pi D(d_2/d_1)\mathbf{e}_1^T P_{-1}^+ \mathbf{e}_1$. A similar result holds for an eigenvalue σ_- of $\hat{J}_-$. This yields a two-term expansion for the eigenvalues of the GCEP, and the associated eigenvector, that are $\mathcal{O}(\nu)$ close to simple eigenvalues $\sigma_\pm$ of $\hat{J}_\pm$:

$$\lambda \sim \sigma_\pm - 2\pi\nu D \frac{d_2}{d_1} \mathbf{e}_1^T P_{-1}^\pm \mathbf{e}_1 + \ldots\,; \quad \mathbf{c} = (\mathbf{c}_+, \mathbf{0})^T\,, \quad \mathbf{c}_+ \in \mathbb{R}^{m_+}\,, \quad \mathbf{c} = (\mathbf{0}, \mathbf{c}_-)^T\,, \quad \mathbf{c}_- \in \mathbb{R}^{m_-}\,. \tag{3.31}$$

In view of the analysis above we say that the jth cell is *stable* if all of the eigenvalues of the cell Jacobian $\hat{J}_j$, which are evaluated at the unperturbed steady-state, lie in the left half-plane. Similarly, we say that the jth cell is *unstable* if $\hat{J}_j$ has an eigenvalue in the right half-plane. By our assumption of the bistability

of $\mathbf{F}$, we conclude that $\text{Re}(\sigma_\pm) < 0$ for any eigenvalue of $\hat{J}_\pm$, and so all the cells are stable. From (3.31), it follows that if ν is sufficiently small, all of the eigenvalues of the GCEP will satisfy $\text{Re}(\lambda) < 0$, so that the constructed steady-states of the full cell-bulk system are linearly stable.

The two-term expansion above for the GCEP eigenvalues also applies for the case where a cell is unstable, such as when one or both of $\sigma_\pm$ have $\text{Re}(\sigma_\pm) > 0$. In this case, for $\nu \ll 1$, we conclude from (3.31) that the GCEP for the linearization of the steady-states (3.24) will have at least one eigenvalue with $\text{Re}(\lambda) > 0$. In this way, for $\nu \ll 1$ we conclude that a steady-state of the full cell-bulk problem is linearly stable if and only if it is constructed such that all of the cells are stable. A single unstable cell destabilizes the entire system. Moreover, the number of unstable eigenvalues of the GCEP is larger when more of the cells are unstable. This qualitative conclusion holds both with and without bulk degradation. From the form of the eigenvectors in (3.31), it follows that those cells that are unstable generate spatially localized instabilities within the cells, while those cells that are stable remain (essentially) in a quiescent state. A more detailed characterization of spatial aspects of this instability is given in [36].

4. Application of the $D = \mathcal{O}(1)$ theory to Lux kinetics.

We now apply the steady-state and linear stability theory developed in §3 to the Lux reaction kinetics given in (1.5) with and without the effect of bulk degradation. We show that QS behavior can occur with bulk degradation and we derive explicit criteria in terms of the population size m that characterizes the switch between upregulated and downregulated states. The theoretical predictions based on our asymptotic analysis are compared with FlexPDE numerical results [12] computed for the cell-bulk system (1.3)–(1.5).

4.1. Lux Kinetics without Bulk Loss.

With no bulk degradation, the NAS for the steady-state construction is given by (3.8), where the Lux kinetics $\mathbf{F}_j$ are as defined in (1.5). Cell heterogeneity is introduced via the parameter κ_{2Aj} in (1.5). In view of the analysis in §2 for an isolated cell, we obtain that (3.8b) of the NAS is satisfied by simply replacing c with $c + 2\pi D S_j$ in (2.2). Then, by solving for u_{1j} in terms of u_{3j} and S_j, as in (2.2), we substitute the resulting expression into (3.8a) to reduce the NAS (3.8) to a lower dimensional nonlinear algebraic system. The result is as follows:

Principal Result 5. *With Lux kinetics and no bulk degradation, the NAS (3.8), characterizing the steady-states of the cell-bulk model (1.3) and (1.5), reduces to a $2m$ dimensional nonlinear system for $\mathbf{S} \equiv (S_1, \ldots, S_m)^T$ and $\mathbf{u}^3 \equiv (u_{31}, \ldots, u_{3m})^T$, given by*

$$\mathcal{A}\mathbf{S} = -\nu(I - E)\mathcal{D}_{21}\left(c\mathcal{P}\mathbf{e} + \kappa_{1A}\mathcal{P}\mathbf{b}\right) , \tag{4.1a}$$

$$Q_j(u_{3j}, S_j) \equiv \frac{1}{\kappa_{2A_j}\kappa_{2R}\kappa_5}\left[c + 2\pi D S_j + \frac{\kappa_{1A}u_{3j}^2}{\kappa_A + u_{3j}^2}\right]\left[1 + \frac{\kappa_{1R}u_{3j}^2}{\kappa_R + u_{3j}^2}\right] - u_{3j} = 0 , \quad j = 1, \ldots, m . \tag{4.1b}$$

Here the matrix $\mathcal{A}$, the diagonal matrix $\mathcal{P}$, and the vector $\mathbf{b} = \mathbf{b}(\mathbf{u}^3)$ are defined by

$$A \equiv I + \nu D(I - E)(\mathcal{D}_1 + 2\pi\mathcal{D}_{21}\mathcal{P}) + 2\pi\nu(I - E)\mathcal{G}_N , \qquad E = \frac{1}{m}\mathbf{e}\mathbf{e}^T , \quad \mathbf{e} = (1, \ldots, 1)^T , \tag{4.1c}$$

$$\mathcal{P} \equiv \text{diag}\left(\frac{1}{\kappa_{2A_1}}, \ldots, \frac{1}{\kappa_{2A_m}}\right) , \qquad \mathbf{b}(\mathbf{u}^3) \equiv \left(\frac{u_{31}^2}{\kappa_A + u_{31}^2}, \ldots, \frac{u_{3m}^2}{\kappa_A + u_{3m}^2}\right)^T , \tag{4.1d}$$

where $\mathcal{G}_N$ is the Neumann Green's matrix and the diagonal matrices $\mathcal{D}_1$ and $\mathcal{D}_{21}$ were given in (3.7b). In terms of solutions to (4.1a) and (4.1b), the other steady-state intracellular species for $j = 1, \ldots, m$ are

$$u_{1j} = \frac{1}{\kappa_{2A_j}}\left(c + 2\pi D S_j + \frac{\kappa_{1A}u_{3j}^2}{\kappa_A + u_{3j}^2}\right) , \quad u_{2j} = \frac{1}{\kappa_{2R}}\left(1 + \frac{\kappa_{1R}u_{3j}^2}{\kappa_R + u_{3j}^2}\right) , \quad u_{4j} = \frac{\kappa_3}{\kappa_4}u_{3j}^2 . \tag{4.1e}$$

In (4.1b), we observe that $Q_j(u_3, 0) = q(u_3)$, where q is defined in (2.3). As a result, the effect of the bulk coupling on the jth cell is contained entirely in the S_j term, which depends on the spatial configuration of the cells through the Neumann Green's matrix $\mathcal{G}_N$ in (4.1c).

Next, we simplify (4.1) assuming identical cellular kinetics ($\kappa_{2Aj} = \kappa_{2A}$) and cell-independent permeabilities ($d_{1j} = d_1$, $d_{2j} = d_2$). Then, since $\mathcal{D}_1$, $\mathcal{D}_{21}$, and $\mathcal{P}$ are multiples of the identity, and by using $(I - E)\mathbf{e} = \mathbf{0}$, we find that (4.1a) and (4.1c) become

$$\mathcal{A}\mathbf{S} = -\nu \frac{d_2\kappa_{1A}}{d_1\kappa_{2A}}(I - E)\mathbf{b}\,, \quad \text{where} \quad \mathcal{A} = I + \nu\left(\frac{D}{d_1} + \frac{2\pi D d_2}{d_1\kappa_{2A}}\right)(I - E) + 2\pi\nu(I - E)\mathcal{G}_N\,. \tag{4.2}$$

From (4.2), we observe that if $u_{3j} = u_{3c}$ for all j, then $\mathbf{b} = b_c\mathbf{e}$ with $b_c = u_{3c}^2/(\kappa_A + u_{3c}^2)$. As a result, since $(I - E)\mathbf{b} = 0$ we obtain that $\mathbf{S} = \mathbf{0}$ from (4.2). This special solution, which satisfies $q(u_{3c}) = 0$ in (2.3), is the common steady-state solution that exists for the intracellular kinetics with no bulk coupling.

We can further simplify (4.2) and (4.1b) for a ring pattern of cells where the centers $\mathbf{x}_k$, for $k = 1, \ldots, m$, of the cells are equally-spaced on a ring concentric within the unit disk Ω. For such a ring pattern of cells, $\mathcal{G}_N$ is a cyclic and symmetric matrix. As shown in §6 of [15], and summarized in Appendix B, the normalized matrix spectrum of $\mathcal{G}_N$, labeled by $\mathcal{G}_N\mathbf{v}_j = g_{N,j}\mathbf{v}_j$ for $j = 1, \ldots, m$, is

$$\begin{aligned} g_{N,1} &= R_{N1} + \sum_{k=2}^{m} G_N(\mathbf{x}_1; \mathbf{x}_k)\,, \qquad \mathbf{v}_1 = \frac{1}{\sqrt{m}}\mathbf{e}\,, \\ g_{N,j} &= R_{N1} + \sum_{k=2}^{m} G_N(\mathbf{x}_1; \mathbf{x}_k)\cos\left(\theta_j(k-1)\right)\,, \qquad \theta_j \equiv \frac{2\pi(j-1)}{m}\,, \\ \mathbf{v}_j &= \sqrt{\frac{2}{m}}\left(1, \cos\left(\theta_j\right), \ldots, \cos\left(\theta_j(m-1)\right)\right)^T\,, \quad \mathbf{v}_{m+2-j} = \sqrt{\frac{2}{m}}\left(0, \sin\left(\theta_j\right), \ldots, \sin\left(\theta_j(m-1)\right)\right)^T\,, \end{aligned} \tag{4.3}$$

for $j = 2, \ldots, \lceil m/2 \rceil$. Here the ceiling function $\lceil x \rceil$ is defined as the smallest integer not less than x. When m is even, there is an additional eigenvector $\mathbf{v}_{\frac{m}{2}+1} = m^{-1/2}(1, -1, \ldots, -1)^T$. Since $(I - E)\mathbf{v}_1 = \mathbf{0}$, while the other eigenvectors satisfy $(I - E)\mathbf{v}_j = \mathbf{v}_j$ owing to $\mathbf{v}_j^T\mathbf{e} = 0$ for $j = 2, \ldots, m$, it follows that the eigenspace of $\mathcal{G}_N$ simultaneously diagonalizes the matrix $I - E$. In Appendix B, we give an explicit formula for the Neumann Green's function in the unit disk, which determines $g_{N,j}$ analytically from (4.3).

By diagonalizing $\mathcal{A}$ as $\mathcal{A} = \mathcal{Q}\Lambda\mathcal{Q}^T$, where $\mathcal{Q}$ is the orthogonal matrix whose columns are the normalized eigenvectors $\mathbf{v}_j$ of $\mathcal{G}_N$, with eigenvalues

$$\Lambda \equiv \text{diag}(a_1, \ldots, a_m)\,, \quad \text{where} \quad a_1 = 1\,, \quad a_j = 1 + \nu\left(\frac{D}{d_1} + \frac{2\pi D d_2}{d_1\kappa_{2A}} + 2\pi g_{N,j}\right)\,, \quad j = 2, \ldots, m\,, \tag{4.4}$$

we can readily invert $\mathcal{A}$ in (4.2). In this way, and by using $\mathbf{e}^T(I - E) = \mathbf{0}$ and $\mathbf{v}_j^T(I - E) = \mathbf{v}_j^T$, we can calculate $\mathbf{S}$ in terms of $\mathbf{u}^3$ explicitly in (4.2) as

$$\mathbf{S} = -\nu\left(\frac{d_2\kappa_{1A}}{d_1\kappa_{2A}}\right)\mathcal{Q}\Lambda^{-1}\mathcal{Q}^T(I - E)\mathbf{b} = -\nu\left(\frac{d_2\kappa_{1A}}{d_1\kappa_{2A}}\right)\sum_{k=2}^{m}\frac{1}{a_k}\mathbf{v}_k\mathbf{v}_k^T\mathbf{b}\,. \tag{4.5}$$

Here $a_2, \ldots, a_m$ are the eigenvalues of $\mathcal{A}$ given in (4.4) and $\mathbf{b} = \mathbf{b}(\mathbf{u}^3)$ is defined in (4.1d). Finally, upon substituting the components of $\mathbf{S}$ from (4.5) into $Q(u_{3j}, S_j) = 0$, as given in (4.1b), we obtain a nonlinear algebraic system only for u_{3j}, for $j = 1, \ldots, m$. For the examples in §4.4, this lower dimensional nonlinear algebraic system is solved numerically using the continuation software MATCONT [8] in which κ_{2A} is the bifurcation parameter. The initial guess for MATCONT is the two-term asymptotics in (3.23).

4.2. Lux Kinetics with Bulk Loss Terms. In this subsection we apply the steady-state theory of §3.1 to Lux kinetics when there is bulk degradation. The key difference between the analysis here and in §4.1 is the presence of QS behavior. We will assume for simplicity that the cells have identical paramaters.

Principal Result 6. *With Lux kinetics and with bulk degradation, so that γ and κ are not both zero, the NAS (3.13) characterizing the steady-states of the cell-bulk model (1.3) and (1.5) reduces to a nonlinear system for $\mathbf{S}$ and $\mathbf{u}^3$ given by*

$$\mathcal{A}\mathbf{S} = -\frac{\nu d_2}{d_1\kappa_{2A}}\left(c\mathbf{e} + \kappa_{1A}\mathbf{b}\right), \qquad \text{where} \qquad \mathcal{A} \equiv \left(1 + \nu\frac{D}{d_1} + \frac{2\pi d_2 D\nu}{d_1\kappa_{2A}}\right) I + 2\pi\nu\mathcal{G}\,, \tag{4.6a}$$

$$Q(u_{3j}, S_j) = 0\,, \qquad j = 1, \ldots, m\,. \tag{4.6b}$$

Here Q is defined in (4.1b) with the cell index j suppressed, while $\mathbf{b}$ is defined in (4.1d). The other components of $\mathbf{u}_j$ are given in terms of u_{3j} by (4.1e) with $\kappa_{2Aj} = \kappa_{2A}$ for $j = 1, \ldots, m$. When the cells are equally-spaced on a ring concentric in the unit disk, there exists a solution branch of (4.6) with $\mathbf{S} = \nu S_c\mathbf{e}$ and $u_{3j} = u_3$ for all $j = 1, \ldots, m$, for which

$$S_c = -\frac{d_2}{d_1\kappa_{2A}}\left(c + \frac{\kappa_{1A}u_3^2}{\kappa_A + u_3^2}\right)\left(1 + \nu\frac{D}{d_1} + \frac{2\pi d_2 D\nu}{d_1\kappa_{2A}} + 2\pi\nu g_1(m)\right)^{-1}. \tag{4.7}$$

On this solution branch, (4.6b) reduces to the single algebraic equation $q_{ring}(u_3) = 0$ defined by

$$q_{ring}(u_3) \equiv \frac{1}{\kappa_{ring}(m)\kappa_{2R}\kappa_5}\left(c + \frac{\kappa_{1A}u_3^2}{\kappa_A + u_3^2}\right)\left(1 + \frac{\kappa_{1R}u_3^2}{\kappa_R + u_3^2}\right) - u_3\,, \tag{4.8}$$

where the effective bifurcation parameter κ_{ring} is given by

$$\kappa_{ring}(m) \equiv \kappa_{2A} + \frac{2\pi D\nu d_2/d_1}{1 + \nu\frac{D}{d_1} + 2\pi\nu g_1(m)}\,. \tag{4.9}$$

Here $g_1(m)$ is the eigenvalue of the (cyclic) Green's matrix $\mathcal{G}$ corresponding to the eigenvector $\mathbf{e} \equiv (1, \ldots, 1)^T$. The steady-state solutions here are accurate to all orders of $\nu \equiv -1/\log\varepsilon$.

Proof. The derivation of (4.6) from the NAS (3.13) is similar to that for the case of no bulk degradation and is omitted. To derive (4.7) for a ring pattern, we use the fact that $\mathcal{G}$ is cyclic so that $\mathbf{e}$ is an eigenvector of $\mathcal{A}$ in (4.6a). As such, by setting $\mathbf{S} = \nu S_c\mathbf{e}$ and $\mathbf{u}^3 = u_3\mathbf{e}$ in (4.6a), we obtain (4.7) for S_c. Finally, we substitute S_c into $Q(u_3, S_c) = 0$ in (4.6b) to readily derive (4.8) and (4.9). ■

Principal Result 6 shows that, with bulk degradation, QS behavior can occur on the branch of equilibria with $\mathbf{S} = \nu S_c\mathbf{e}$ and $\mathbf{u}_j = \mathbf{u}$, for $j = 1, \ldots, m$. The algebraic equation in (4.8) has exactly the same form as that for the equilibria of the uncoupled system $q(u_3) = 0$, except that $\kappa_{\text{ring}}(m)$ replaces κ_{2A} in the definition of q given in (2.3). Therefore, changes in the population size m effectively changes the value of κ_{2A} according to (4.9) and can result in a passage beyond the saddle-node point in the bifurcation diagram of u_3 versus κ_{2A}, as computed in §2 (see Fig. 2.1). In this way, changes in the population size can result in a QS transition between equilibria, i.e. between downregulated and upregulated states or vice versa. In contrast, recall from our analysis in §4.1, that the branch of equilibria with $\mathbf{u}_j = \mathbf{u}$, for $j = 1, \ldots, m$, is biologically uninteresting in terms of QS behavior.

The critical population m_c required for a QS transition from a downregulated to an upregulated steady-state for a ring pattern in the unit disk is easily computed numerically. To do so, we first use (B.2) of

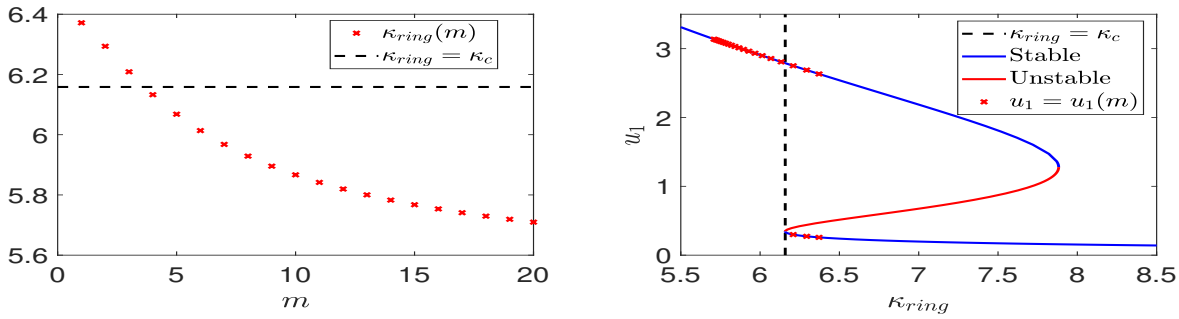

(a) κ_{ring} versus m

(b) u_1 versus κ_{ring}

Figure 4.1: QS behavior for a ring pattern in the unit disk with parameters in (4.10) and Table 1. Left panel: κ_{ring} versus m from (4.9). The dashed line is the saddle-node point κ_c of κ_{ring} for (4.8). Right panel: Steady-state bifurcation diagram of u_1 from Principal Result 6 with $\kappa_{\text{ring}} = \kappa_c$ shown (vertical dashed line). The equilibria for the computed values of κ_{ring} for $m \geq 1$ shown in the left panel are indicated. When m increases beyond the critical population size $m_c = 4$, the lower stable branch ceases to exist and there is a transition to the upregulated state.

Appendix B to calculate the matrix entries of $\mathcal{G}$, which yields $g_1(m)$ from (B.3). Next, the saddle-node value κ_c of κ_{2A} is calculated by simultaneously solving $q(u_3) = q'(u_3) = 0$ for u_3 and κ_c, with q defined in (2.3). For a given κ_{2A}, the critical population threshold m_c is the minimum value of m (if it exists) for which κ_{ring} in (4.9) satisfies $\kappa_{\text{ring}} < \kappa_c$. Here we use the fact that κ_{ring} is a decreasing function of m (see Fig. 4.1a). For this critical population m_c, the asymptotic theory predicts that there is a transition to the upregulated state. A similar argument applies for calculating the critical population threshold for a transition from the upregulated state to the downregulated state as m decreases.

We illustrate Principal Result 6 for a ring pattern of identical cells in the unit disk for the parameters

$$D = 1\,, \quad \varepsilon = 0.01\,, \quad d_1 = d_2 = 0.5\,, \quad r_0 = 0.5\,, \quad \kappa = 0.5 \quad \gamma = 1\,, \quad \kappa_{2A} = 5.5\,, \quad \kappa_{DR} = 0.0125\,, \tag{4.10}$$

with the other parameters as in Table 1. In Fig. 4.1b we plot the bifurcation diagram of the steady-state u_1 versus κ_{ring}, as obtained by first solving (4.8) for u_3 and then using (2.2) to relate u_1 to u_3. This plot is identical to Fig. 2.1e but where the horizontal axis is now κ_{ring}. The saddle-node value $\kappa_c \approx 6.16$, characterizing the non-existence of the downregulated state, is shown by the vertical dashed line. In Fig. 4.1a we use (4.9) to plot κ_{ring} for discrete values of $m \geq 1$, and we mark the corresponding steady-state as $u_1 = u_1(m)$ in the bifurcation diagram in Fig. 4.1b. We observe that κ_{ring} dips below κ_c when $m = 4$, which leads to a QS transition from the downregulated to the upregulated steady-states. In addition, the hysteresis structure in Fig. 4.1b implies that the transition back to a downregulated state will not occur as m decreases for this parameter set. The linear stability properties of these steady-states, as obtained from the GCEP (3.18) using the methodology described below in §4.3, is shown in Fig. 4.1b.

Finally, we remark that (4.7)–(4.9) can be used not just for a ring pattern, but for *any* spatial configuration $\{\mathbf{x}_1, \ldots, \mathbf{x}_m\}$ of cells in a 2-D domain Ω for which $\mathbf{e} \equiv (1, \ldots, 1)^T$ is an eigenvector of $\mathcal{G}$. It is an open problem to identify such symmetric patterns of cells in an arbitrary 2-D domain Ω.

4.3. Linear stability theory with Lux kinetics. To implement the linear stability theory based on the GCEP (3.18) for the Lux kinetics, we must calculate the number, N, of zeroes of $\det \mathcal{M}(\lambda) = 0$ in $\text{Re}(\lambda) > 0$ along the solution branches of the NAS, as given by (4.1) or (4.6) with or without bulk degradation,

respectively. To do so, we use a line-sweep method along the positive real axis $\lambda > 0$ to count the number of unstable real eigenvalues. We also use a winding-number algorithm to detect *all* unstable eigenvalues in $\mathrm{Re}(\lambda) > 0$. For cell patterns in the unit disk, the eigenvalue-dependent Green's matrix $\mathcal{G}_\lambda$, as needed in the GCEP matrix $\mathcal{M}(\lambda)$ in (3.18a), is determined analytically by (B.2) of Appendix B.

In the line-sweep approach, we look for sign changes of $\det \hat{\mathcal{M}}(\lambda)$ over the segment $\lambda \in (0, \mathcal{R}]$ of the positive real axis, for some $\mathcal{R} \gg 1$. Here, $\hat{\mathcal{M}}(\lambda)$, as defined in (3.22), is the diagonal scaling of the GCEP matrix $\mathcal{M}(\lambda)$ in (3.18a). In contrast to using $\det \mathcal{M}(\lambda)$, which has poles at the eigenvalues of the cell Jacobians, $\det \hat{\mathcal{M}}(\lambda)$ is continuous on $\lambda \in (0, \mathcal{R}]$. For the special case of a ring pattern of cells in the unit disk, where mode degeneracy occurs, $\det \hat{\mathcal{M}}(\lambda)$ will have a double root at certain positive real eigenvalues, and so $\det \hat{\mathcal{M}}(\lambda)$ will not change sign at these points. The required modification of the line-sweep strategy to identify unstable real eigenvalues for such ring patterns is discussed below.

To detect instabilities associated with complex eigenvalues, we use the winding-number approach of [15] and [19]. In the complex λ plane, we let $\Gamma_\mathcal{R} \subset \mathbb{C}$, with $\mathcal{R} > 0$, denote the counterclockwise-oriented closed curve consisting of the union of the line segment $-i\mathcal{R} \leq \lambda \leq i\mathcal{R}$ and the semi-circular arc $\lambda = \mathcal{R}e^{i\omega}$, with $-\pi/2 \leq \omega \leq \pi/2$. From the argument principle of complex analysis, and by letting $\mathcal{R} \to \infty$, the number of roots N of $\det \mathcal{M}(\lambda) = 0$ in $\mathrm{Re}(\lambda) > 0$ is

$$N = \lim_{\mathcal{R}\to\infty} W^{\Gamma_\mathcal{R}} + P\,. \tag{4.11}$$

Here $W^{\Gamma_\mathcal{R}}$ is the winding number of $\det \mathcal{M}(\lambda)$ over $\Gamma_\mathcal{R}$, which is calculated numerically using a line-sweep over the contour together with the algorithm in [2]. In (4.11), P is the number of poles of $\det \mathcal{M}(\lambda)$ in $\lambda > 0$, which is easily calculated since these poles can only occur at the eigenvalues of the cell Jacobians.

The line-sweep and winding-number approaches to detect instabilities applies with and without bulk degradation. However, since with no bulk loss, where $\gamma = \kappa = 0$, the Green's matrix $\mathcal{G}_\lambda$ in $\mathcal{M}$ does not exist when $\lambda = 0$, we must avoid evaluating $\det \hat{\mathcal{M}}$ and $\det \mathcal{M}$ at $\lambda = 0$. For the winding-number approach, this issue is circumvented by simply shifting the entire contour very slightly to the right. As shown in Principal Result 4, since $\lambda = 0$ crossings can only occur at bifurcation points of the NAS (4.1) and (4.6), these crossings are readily detected from a numerical solution of the NAS.

For the special case of a ring pattern of identical cells concentric within the unit disk, and with bulk degradation, we can simplify the implementation of the linear stability theory for symmetric solutions of the NAS (4.6), where $\mathbf{S} = \nu S_c \mathbf{e}$ as given in (4.7). For such a ring pattern, $\mathcal{M}(\lambda)$ in (3.18a) reduces to

$$\mathcal{M}(\lambda) = \left(1 + \nu\frac{D}{d_1} + 2\pi D\nu \frac{d_2}{d_1}\frac{M_{11}}{\det(\lambda I - J)}\right) I + 2\pi\nu\mathcal{G}_\lambda\,, \tag{4.12}$$

where M_{11}, as defined in (3.18c), is independent of j. Since $\mathcal{G}_\lambda$ is cyclic and symmetric, its matrix spectrum is given explicitly in (B.3) of Appendix B. As a result, the condition $\det \mathcal{M}(\lambda) = 0$, is reduced to the following scalar root-finding problems $\mathcal{F}_j(\lambda) = 0$, for $j = 1\ldots, m$, based on the eigenvalues of $\mathcal{M}(\lambda)$:

$$\mathcal{F}_j(\lambda) \equiv g_{\lambda,j} + \frac{1}{2\pi\nu}\left(1 + \nu\frac{D}{d_1}\right) + \frac{Dd_2}{d_1}\frac{M_{11}}{\det(\lambda I - J)}\,, \quad j = 1, \ldots, m \tag{4.13}$$

Here $g_{\lambda,j}$ is the eigenvalue of $\mathcal{G}_\lambda$ with corresponding eigenvector $\mathbf{v}_j$ (see (B.3) of Appendix B).

Any root of $\mathcal{F}_1 = 0$ is an eigenvalue of the GCEP for the synchronous mode $\mathbf{v}_1 = \mathbf{e}$. In contrast, roots of $\mathcal{F}_j = 0$, for $j = 2, \ldots, m$, are eigenvalues for the asynchronous modes associated with the $(m-1)$-dimensional orthogonal subspace to $\mathbf{e}$. As shown in Appendix B, when m is odd, the eigenvalues of $\mathcal{G}_\lambda$ for the asynchronous modes have a geometric multiplicity of two. However, when m is even, there is an additional eigenvalue of

multiplicity one associated with an asynchronous mode with eigenvector $\mathbf{v}_{m/2+1} = (1, -1, 1, \ldots, -1)^T$. In summary, for a symmetric ring pattern, for a root-finding problem based on (4.13) we need only consider the synchronous $j = 1$ mode and $\lceil m/2 \rceil$ distinct asynchronous modes, while ensuring that unstable eigenvalues of the asynchronous modes are counted with the correct multiplicity.

For a symmetric ring pattern, the line-sweep procedure outlined above is modified to seek sign changes of $\hat{\mathcal{F}}_j(\lambda) \equiv \mathcal{F}_j(\lambda) \det(\lambda I - J)$, which is continuous on $0 < \lambda \leq \mathcal{R}$. Since $\det \hat{\mathcal{M}}$ may not change sign near some of its roots as λ is swept across the real axis for a symmetric ring pattern, by instead using $\hat{\mathcal{F}}_j$ in the line-sweep procedure we will have simple zero-crossings at unstable eigenvalues of the GCEP. The linear stability properties of the steady-states shown in Fig. 4.1b were deduced from this approach.

4.4. Illustration and validation of the theory with no bulk loss. With no bulk degradation, we now illustrate the steady-state and linear stability theory in §4.1 and §4.3 for a ring pattern, with ring radius r_0, of m identical cells in the unit disk for the parameter set

$$D = 1\,, \quad \gamma = \kappa = 0\,, \quad \varepsilon = 0.05\,, \quad d_1 = d_2 = 0.1\,, \quad r_0 = 0.25\,, \quad \kappa_{DR} = 0.0125\,, \tag{4.14}$$

with the other parameters as in Table 1. Recall from the lower row of Fig. 2.1 that with $\kappa_{DR} = 0.0125$ the Lux ODE system for an isolated cell has at most three steady-states. From using MATCONT [8] on the NAS obtained by substituting $\mathbf{S}$ from (4.5) into (4.1b), we obtain the steady-state bifurcation diagram in Fig. 4.2 of u_{11} versus κ_{2A} for $m = 2$ and $m = 3$, as obtained from (4.1e). The results are shown only for $m = 2, 3$, as the bifurcation structure of equilibria becomes increasingly complex for larger m. However, the main branch of equilibria, where $\mathbf{u}^3 = u_c\mathbf{e}$ and $\mathbf{S} = \mathbf{0}$, is independent of m and is easy to compute.

For each point in the bifurcation diagram shown in Fig. 4.2, we use the line-sweep and winding-number algorithms, described in §4.3, to determine the linear stability properties of the steady-state. With this methodology, the different line styles in Fig. 4.2 indicate the number of unstable eigenvalues in $\mathrm{Re}(\lambda) > 0$ of the GCEP (3.18). As predicted by Lemma 3.1, we observe for $m = 2$ and $m = 3$ that along the main branch of equilibria in Fig. 4.2, where $\mathbf{u}^3 = u_c\mathbf{e}$ and $\mathbf{S} = \mathbf{0}$, stability is lost at the saddle-node points associated with the uncoupled Lux ODE kinetics. This zero-eigenvalue crossing corresponds to the synchronous mode $\mathbf{v}_1$ in (4.3). A little further along the unstable branch, the asynchronous mode goes unstable, which for $m = 3$ corresponds to a zero-eigenvalue crossing of multiplicity of two. The bifurcating branches for $m = 2$, which form a closed loop, undergo two additional bifurcations where stability is gained and then lost as the curve is traversed counter-clockwise. The key observation from the bifurcation diagram in Fig. 4.2a when $m = 2$ is that there is a parameter range of κ_{2A} where there exists a linearly stable steady-state solution in which the two cells have different intracellular concentrations (yellow stars in Fig. 4.2a).

The bifurcation structure for $m = 3$ is more intricate. Along the main branch with $\mathbf{S} = 0$, there are four additional branches that bifurcate from the zero-eigenvalue crossing for the degenerate asynchronous modes $\mathbf{v}_2$ and $\mathbf{v}_3$ in (4.3), forming two pairs of solution branches. Each pair forms a closed loop similar to the one shown for $m = 2$. On each loop, two of the three cells have identical intracellular concentrations. On one of the loops, there is an additional bifurcating branch on which all three cells have different concentrations. This branch appears to cross the main branch at around $\kappa_{2A} \approx 7.6$; however, the apparent intersection is not a bifurcation, but is due to projecting the equilibria onto the u_{11} versus κ_{2A} plane. There is no zero-eigenvalue crossing for the GCEP at the apparent intersection. There are also apparent intersections of the two loop structures which, for the same reason, do no correspond to bifurcations.

Next, we discuss the bifurcation structure in Fig. 4.2 with regards to the predictions from the two-term asymptotic theory in §3.3 for bistable intracellular kinetics. The stable branches not belonging to the main branch in Fig. 4.2 correspond to steady-states constructed from 'stable' cells. Recall from §3.3 that a cell is termed 'stable' if its intracellular concentrations are associated with a stable steady-state in the uncoupled

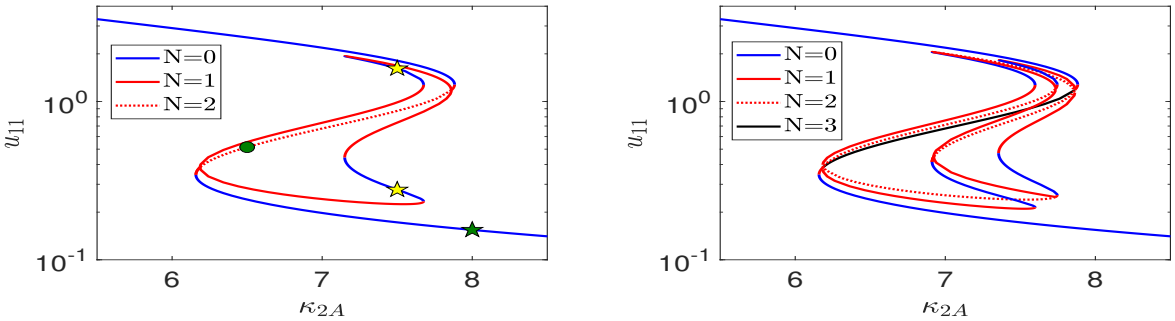

(a) u_{11} for $m = 2$ (b) u_{11} for $m = 3$

Figure 4.2: Bifurcation diagrams of u_{11} when $m = 2$ (left) or $m = 3$ (right) cells for a ring pattern in the unit disk with no bulk degradation. The main branch with $\mathbf{S} = 0$ is the one that passes through the green star and the green circle in the left panel. Line styles are labeled by N, the number of unstable eigenvalues of the GCEP in $\mathrm{Re}(\lambda) > 0$. Blue branches indicate linearly stable steady-states while all others are unstable. Points marked with stars indicate where FlexPDE [12] numerical solutions of the cell-bulk model are performed. The green circle denotes a point where the line-sweep and winding-number methods are shown in Fig. 4.3. Parameters as in (4.14) and Table 1.

problem. For example, consider the branch with $m = 2$ cells where one of the cells is 'on' and the other is 'off'. Observe that this branch is stable and loses stability when one of the cells becomes associated with an unstable part of the main branch. Similar reasoning applies to the $m = 3$ case.

To verify that the line-sweep method yields the correct number of eigenvalues in $\mathrm{Re}(\lambda) > 0$, we now compare the results from this method with those obtained from the winding-number algorithm described in §4.3. We give one illustration of this in Fig. 4.3 for the steady-state indicated by the green circle on the main branch shown in Fig. 4.2a where $m = 2$. For the asynchronous mode $j = 2$, in Fig. 4.3a we show that $\hat{\mathcal{F}}_2(\lambda) \equiv \mathcal{F}_2(\lambda)\det(\lambda I - J)$, where $\mathcal{F}_2(\lambda)$ is defined in (4.13), has a unique positive root in $\lambda > 0$. In Fig. 4.3b, where we plot the real and imaginary parts of $\mathcal{F}_2$ over the closed contour $\Gamma_{\mathcal{R}}$ as defined in the winding-number algorithm in §4.3, we observe that the winding number of $\mathcal{F}_2$ over this contour is zero. Moreover, since the green circle is on the main branch in Fig. 4.2a, where $\mathbf{S} = 0$, the steady-states are identical to those of an isolated cell. Since the cell Jacobian has a single positive eigenvalue, then $\mathcal{F}_2$ has a simple pole in $\mathrm{Re}(\lambda) > 0$. Therefore, by applying (4.11) to $\mathcal{F}_2$ we get $P = 1$ and $\lim_{\mathcal{R}\to\infty} W^{\Gamma_{\mathcal{R}}} = 0$, so that $N = 1$. We deduce from the winding-number method that there is a unique unstable eigenvalue for the asynchronous $j = 2$ mode, in agreement with the conclusion in Fig. 4.3a from the line-sweep method. Similarly, at the green circle in Fig. 4.2a, the line-sweep and winding-number methods applied to $\mathcal{F}_1(\lambda)$ yields that $N = 1$ for the synchronous $j = 1$ mode. In this way, at the green circle in Fig. 4.2a there are a total of two unstable eigenvalues in $\mathrm{Re}(\lambda) > 0$ for the GCEP (3.18).

While the additional branches that bifurcate from the main branch in Fig. 4.2 are intricate, most of them are unstable and do not play a role in QS. It is unclear whether or not QS behavior can occur in the few such branches that are stable. The fact that QS behavior is not present on the main branch of equilibria, which corresponds essentially to the case of m isolated cells, indicates that there can be no *collective* response without the presence of bulk loss terms. The model of [27] exhibits QS behavior because the Dirichlet condition on the domain boundary $\partial\Omega$ is a source of bulk loss.

To confirm the predictions of the asymptotic theory we used FlexPDE [12] to compute numerical solutions

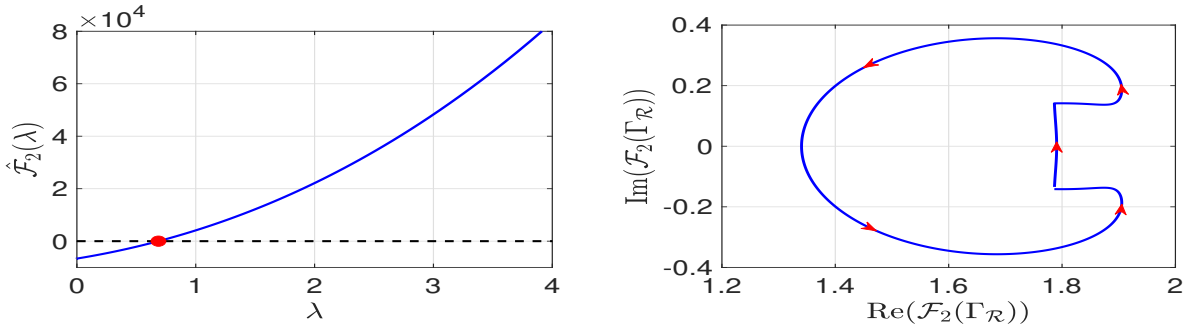

(a) line-sweep: $\hat{\mathcal{F}}_2(\lambda)$ on $\lambda > 0$

(b) winding-number: $\hat{\mathcal{F}}_2(\lambda)$ on $\Gamma_{\mathcal{R}}$

Figure 4.3: Line-sweep and winding number computation for the roots of $\mathcal{F}_2(\lambda) = 0$ from the GCEP, as defined in (4.13) for the asynchronous $j = 2$ mode, at the steady-state marked with a green circle in Fig. 4.2a where $m = 2$ and $\kappa_{2A} = 6.5$. Left panel: $\hat{\mathcal{F}}_2(\lambda) \equiv \mathcal{F}_2(\lambda)\det(\lambda I - J)$ on the positive real axis $\lambda > 0$ showing a unique positive root at $\lambda \approx 0.7$. Right panel: $\mathcal{F}_2(\lambda)$ in the complex plane over the semi-circular contour $\Gamma_{\mathcal{R}}$ in $\mathrm{Re}(\lambda) > 0$ with $\mathcal{R} = 50$, showing a zero winding number.

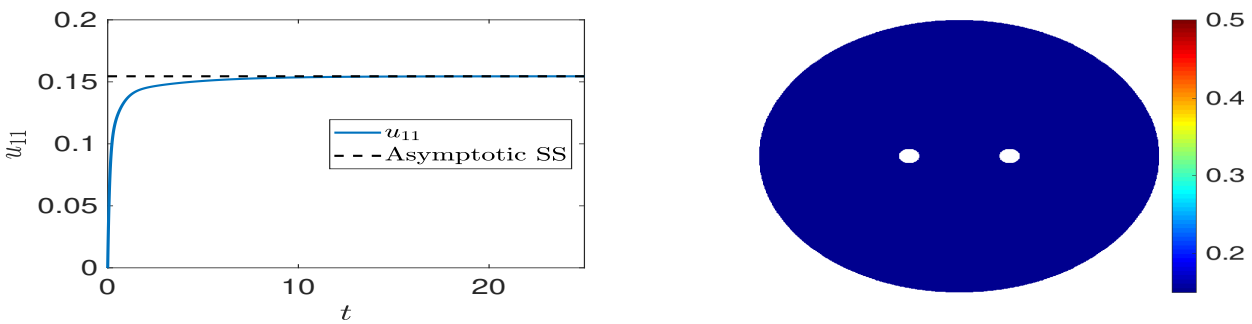

Figure 4.4: Left panel: FlexPDE [12] numerical solution for u_{1j} versus t from the cell-bulk system (1.3) and (1.5) for the parameter set in (4.14) and Table 1, with $\kappa_{2A} = 8$ and $m = 2$. The steady-state predicted from the asymptotic theory, marked with a green star in Fig. 4.2a, is indicated by the dashed line in the left panel. Right panel: snapshot of the nearly spatially uniform bulk solution at a time near the steady-state showing two downregulated cells.

of the cell-bulk model in (1.3) and (1.5) at the starred points shown in Fig. 4.2a with $m = 2$ for the parameters in (4.14) and Table 1. In the FlexPDE computations, the relative error tolerances were selected as 5×10^{-5}, while the meshing of the unit disk was done automatically and was adaptively refined to achieve the desired accuracy. The BDF2 method was used for the time-stepping.

Fig. 4.4 shows the FlexPDE [12] numerical solution for $m = 2$ and $\kappa_{2A} = 8$, which corresponds to the monostable regime where only the downregulated steady-state exists. The initial conditions were are all chosen to be zero. The unique steady-state has $\mathbf{u}_j = \mathbf{u}$ for $j = 1, 2$. Since the FlexPDE results for the intracellular concentrations for each component of $\mathbf{u}_j$ are nearly identical throughout the computation, only the u_{11} component is shown in the left panel of Fig. 4.4. In this figure, we also plot the steady-state predicted from the asymptotic theory, denoted by the green star in Fig. 4.2a. The numerically computed bulk solution near the steady-state is shown in the right panel of Fig. 4.4.

In Fig. 4.5 we show FlexPDE [12] results for $m = 2$ and $\kappa_{2A} = 7.5$, which corresponds to the bistable

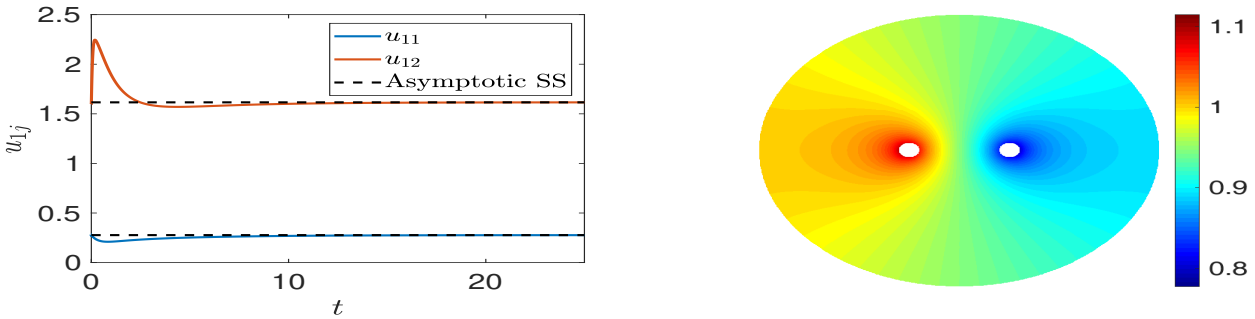

Figure 4.5: Left panel: FlexPDE [12] numerical solution for u_{1j} versus t from the cell-bulk system (1.3) and (1.5) for the parameter set in (4.14) and Table 1, with $\kappa_{2A} = 7.5$ and $m = 2$. The steady-state predicted from the asymptotic theory, marked by the two yellow stars in Fig. 4.2a, is indicated by the dashed lines in the left panel. Right panel: snapshot of the bulk solution near equilibrium showing one downregulated and one upregulated cell.

regime where one of the cells is upregulated while the other is downregulated. The predicted steady-states from the asymptotic theory, as denoted by the yellow stars in Fig. 4.2a, are also plotted. The initial conditions for the numerical calculations were chosen near the predicted steady-state. The numerically computed spatially non-uniform bulk solution near the steady-state is shown in the right panel of Fig. 4.5. We observe that one of the cells is acting as a sink of AI, with positive flux into the cell, while the other acts as a source of AI, with an equal amount of flux out of the cell.

4.5. Illustration and validation of the theory with bulk loss. With bulk degradation, we first illustrate our asymptotic prediction in Principal Result 6 for a QS transition for a ring pattern in the unit disk when

$$D = 1\,, \quad \gamma = 1\,, \quad \kappa = 0\,, \quad \varepsilon = 0.05\,, \quad d_1 = d_2 = 0.5\,, \quad r_0 = 0.25\,, \qquad \kappa_{DR} = 0.0125\,, \tag{4.15}$$

with the remaining parameters as in Table 1. For these parameters in the Lux kinetics, which correspond to the lower row in Fig. 2.1, the saddle-node point on the solution branch of $q_{\text{ring}}(u_3) = 0$ in (4.8) is at $\kappa_{\text{ring}} = \kappa_c \approx 6.16$. Then, by using (4.9) for $\kappa_{\text{ring}}(m)$, we calculate that $\kappa_{\text{ring}}(2) \approx 6.26$ and $\kappa_{\text{ring}}(3) \approx 6.10$. Since $\kappa_{\text{ring}}(3) < \kappa_c$, this predicts that a quorum is achieved at a population of three.

To confirm this QS threshold from the asymptotic theory, in Fig. 4.6 we show FlexPDE [12] simulations of the cell-bulk model (1.3) and (1.5) for $m = 2$ and for $m = 3$, as obtained using the initial conditions

$$\mathbf{u}_j(0) = \left(0.3, 0.3, 3\cdot 10^{-3}, 3\cdot 10^{-7}\right)^T\,, \quad j = 1, \ldots, m\,; \qquad U(\mathbf{x}, 0) = \frac{d_2}{d_1} u_{11}\,. \tag{4.16}$$

These initial conditions are close to the downregulated state for $m = 2$. As predicted by the asymptotic theory, from Fig. 4.6 we observe that when $m = 2$ the FlexPDE numerical solution of the cell-bulk model remains close to the initial condition, with all cells in the downregulated state. In contrast, for the same initial conditions (4.16) but with $m = 3$, the FlexPDE results in Fig. 4.6 confirm that there is a transition to the upregulated steady-state, which suggests that the downregulated steady-state no longer exists. The predicted intracellular steady-states from the asymptotic theory are obtained by first numerically solving $q_{\text{ring}}(u_3) = 0$ in (4.8) for u_3, and then using the common source strength $S_j = \nu S_c$ from (4.7) in (4.1e). The resulting bistable steady-states for u_{11} are shown in the left panel of Fig. 4.6 together with the FlexPDE results for u_{11}. Snapshots of the FlexPDE result for the bulk solution at a time near equilibrium is shown in the middle and right panels of Fig. 4.6 for $m = 2$ and $m = 3$, respectively.

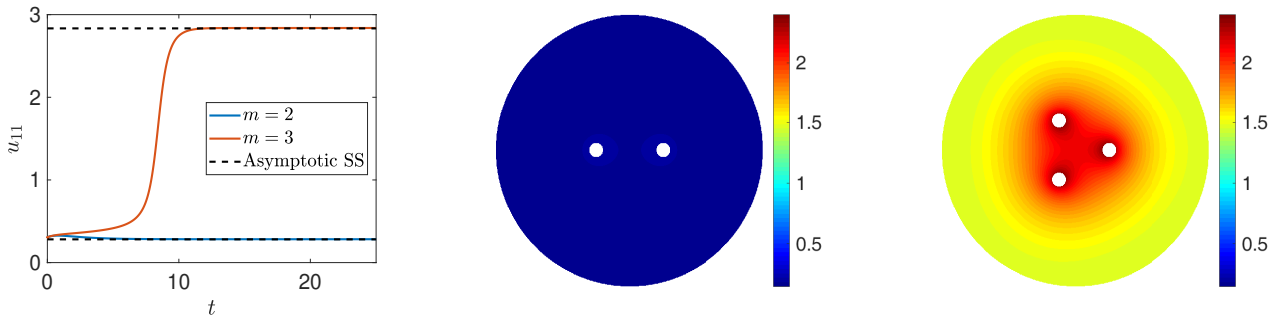

(a) u_{11} versus t for $m = 2, 3$ (b) bulk solution ($m = 2$) (c) bulk solution ($m = 3$)

Figure 4.6: FlexPDE [12] numerical results for the cell-bulk model (1.3) and (1.5) for a ring pattern of $m = 2, 3$ cells. Left panel: u_{11} versus t. The solutions in each cell are identical. The dashed lines are the asymptotic predictions for the bistable states. Middle and right panels: snapshot of the bulk solution near equilibrium for $m = 2$ (middle) and $m = 3$ (right). The bulk solution is spatially non-uniform for both $m = 2$ and $m = 3$. For $m = 3$, the cells are in the upregulated state. Parameters as in (4.15) and Table 1.

Next, we derive a result analogous to that in (4.8) and (4.9) of Principal Result 6, which can be used to predict QS behavior for an arbitrary spatial configuration of identical cells. For an arbitrary cell pattern, the NAS in (4.6) admits a leading-order-in-ν solution of the form $\mathbf{S} \sim \nu S_c \mathbf{e} + \mathcal{O}(\nu^2)$ and $\mathbf{u}_j = u_c \mathbf{e} + \mathcal{O}(\nu)$. However, since the cell locations and cell population m only arise at $\mathcal{O}(\nu^2)$ for $\mathbf{S}$, we must derive a result for $\mathbf{S}$ that is accurate to $\mathcal{O}(\nu^2)$ in order to detect QS behavior. Our result is summarized as follows:

Principal Result 7. *For $\nu \to 0$, on the solution branch where $\mathbf{S} = \nu S_c \mathbf{e} + \mathcal{O}(\nu^2)$, the NAS (4.6) decouples into m scalar nonlinear algebraic equations $q_j(u_{3j}; m) = 0$, for $j = 1, \ldots, m$, where*

$$q_j(u_{3j}; m) \equiv \frac{1}{\kappa_j(m)\kappa_{2R}\kappa_5} \left(c + \frac{\kappa_{1A} u_{3j}^2}{\kappa_A + u_{3j}^2} \right) \left(1 + \frac{\kappa_{1R} u_{3j}^2}{\kappa_R + u_{3j}^2} \right) - u_{3j}. \tag{4.17}$$

In (4.17), the effective parameter, $\kappa_j(m)$, depending on both the cell index j and cell population m, is

$$\kappa_j(m) \equiv \kappa_{2A} + \frac{2\pi D \nu d_2/d_1}{1 + \nu \frac{D}{d_1} + 2\pi\nu \left(\mathcal{G}\mathbf{e}\right)_j}. \tag{4.18}$$

Here $\mathcal{G}$ is the Green's matrix, with matrix entries determined by (3.11), while $(\mathcal{G}\mathbf{e})_j$ denotes the jth component of $\mathcal{G}\mathbf{e}$ with $\mathbf{e} \equiv (1, \ldots, 1)^T$. The steady-states for the intracellular species, as determined from the roots of $q_j = 0$ and together with (4.1e) in which S_j is given by

$$S_j = -\frac{\nu d_2}{d_1 \kappa_{2A}} \left(c + \frac{\kappa_{1A} u_{3j}^2}{\kappa_A + u_{3j}^2} \right) \left(1 + \nu \frac{D}{d_1} + \frac{2\pi d_2 D \nu}{d_1 \kappa_{2A}} + 2\pi\nu \left(\mathcal{G}\mathbf{e}\right)_j \right)^{-1} + \mathcal{O}(\nu^3), \tag{4.19}$$

are accurate up to and including order $\mathcal{O}(\nu^2)$.

Proof. We first determine the jth component S_j of $\mathbf{S}$ accurate to order $\mathcal{O}(\nu^2)$, but without formally expanding it in powers of ν. In component form, the matrix equation in (4.6a) yields

$$S_j \left(1 + \nu \frac{D}{d_1} + \frac{2\pi d_2 D \nu}{d_1 \kappa_{2A}} + 2\pi\nu \frac{(\mathcal{G}\mathbf{S})_j}{S_j} \right) = -\frac{\nu d_2}{d_1 \kappa_{2A}} \left(c + \frac{\kappa_{1A} u_{3j}^2}{\kappa_A + u_{3j}^2} \right), \quad \text{for} \quad j = 1, \ldots, m. \tag{4.20}$$

Since $\mathbf{S} \sim \nu S_c \mathbf{e}$ to leading order in ν, it follows that $(\mathcal{G}\mathbf{S})_j / S_j \sim (\mathcal{G}\mathbf{e})_j + \mathcal{O}(\nu)$. By using this estimate in (4.20) we obtain (4.19) for S_j. Then, by using (4.19) for S_j, we set $Q(u_{3j}, S_j) = 0$ in (4.6b), with Q as defined in (4.1b). This readily yields (4.17) with the effective parameters $\kappa_j(m)$ as given by (4.18). ■

For the special case of a ring pattern in the unit disk, where $(\mathcal{G}\mathbf{e})_j = g_1(m)$, the effective parameter $\kappa_j(m)$ is independent of j and reduces to κ_{ring} in (4.9), with the corresponding result being accurate to all orders in ν. Although less accurate for an arbitrary cell pattern, the effective parameter in (4.18) is a natural generalization of that for the ring pattern. Moreover, we observe from (4.18) that to leading-order in ν we have $\kappa_j = \kappa_{2A} + \mathcal{O}(\nu)$, so that $u_{3j} = u_3 + \mathcal{O}(\nu)$ and $S_j \sim \nu S_c + \mathcal{O}(\nu^2)$, from (4.17) and (4.19).

The prediction of QS behavior for an arbitrary cell pattern using Principal Result 7 is similar to that for a ring pattern based on (4.8) and (4.9). The key difference here for an arbitrary cell pattern is that each cell has its own effective parameter κ_j, which depends on the the cell population m, the spatial configuration $\{\mathbf{x}_1, \ldots, \mathbf{x}_m\}$ of all the cells through the term $(\mathcal{G}\mathbf{e})_j$ in (4.18), and the bulk parameters d_1, d_2, and D. As m increases, we conclude that if κ_j decreases below the saddle-node value κ_c for roots of (4.17), the asymptotic theory predicts that the jth cell will transition to the upregulated steady-state.

To validate the QS transition predicted by (4.17) and (4.18) we use FlexPDE [12] to compute numerical solutions to the cell-bulk model (1.3) and (1.5) for the parameters in (4.15) and Table 1. The centers of either two or three cells are given in the caption of Fig. 4.7. The saddle-node point for (4.17) occurs at $\kappa_j = \kappa_c \approx 6.16$, while from (4.18) the effective parameters $\kappa_j(m)$, for $j = 1, \ldots, m$ with $m = 2, 3$, are

$$\kappa_1(2) \approx 6.30\,, \quad \kappa_2(2) \approx 6.21\,; \qquad \kappa_1(3) \approx 6.13\,, \quad \kappa_2(3) \approx 6.09\,, \quad \kappa_3(3) \approx 6.09\,. \tag{4.21}$$

Since $\kappa_j(2) > \kappa_c$ and $\kappa_j(3) < \kappa_c$ for all $j = 1, \ldots, m$, the asymptotic theory predicts that the critical population for a QS transition to the upregulated state is $m = 3$. This prediction is confirmed in Fig. 4.7 where we plot FlexPDE results for the L^2-norm of $\mathbf{u}^1$ for $m = 2$ and $m = 3$ as well as for each component of $\mathbf{u}_1$ for $m = 3$ only. The steady-states predicted by the asymptotic theory in Principal Result 7 are also shown. Snapshots, near the steady-state, of the FlexPDE computed bulk solution in Fig. 4.7 for $m = 2$ and $m = 3$ further confirm that the QS transition to the upregulated state occurs when $m = 3$.

5. The distinguished limit of large bulk diffusion.

Allowing for bulk degradation, in this section we simplify the steady-state analysis of §4.2 for the large bulk diffusivity regime $D = D_0/\nu$, where $\nu = -1/\log \varepsilon$ and $D_0 = \mathcal{O}(1)$. For this distinguished limit of D, the cell locations have only a weak effect on the overall behavior, while the number of cells have an $\mathcal{O}(1)$ effect on the steady-states. In §5.1, a simplified version of Principal Result 6 is derived that provides an explicit analytical criterion characterizing transitions between bistable steady-states for an arbitrary cell pattern. A similar, but more accurate result, is derived for a ring pattern in the unit disk. In §5.2 we asymptotically reduce the full ODE-PDE cell-bulk model (1.3)–(1.5) to a simpler ODE-DAE system that involves D_0, and includes weak $\mathcal{O}(\nu)$ effects resulting from the spatial configuration of cells. Results from this ODE-DAE system that predict QS behavior are compared with FlexPDE [12] computed from the cell-bulk model.

5.1. Steady-State Solutions.

To analyze the steady-state problem in the regime where $D = D_0/\nu$, with $\nu \ll 1$, we first must approximate the Green's function $G(\mathbf{x}, \mathbf{x}_i)$ in (3.11), which satisfies

$$\Delta G - \nu \frac{\gamma}{D_0} G = -\delta(\mathbf{x} - \mathbf{x}_i)\,, \quad \mathbf{x} \in \Omega\,; \qquad D_0 \partial_n G + \nu \kappa G = 0\,, \quad \mathbf{x} \in \partial\Omega\,, \tag{5.1a}$$

$$G(\mathbf{x}; \mathbf{x}_i) = -\frac{1}{2\pi} \log|\mathbf{x} - \mathbf{x}_i| + R_i + o(1)\,, \quad \text{as} \quad \mathbf{x} \to \mathbf{x}_i\,. \tag{5.1b}$$

Since (5.1) has no solution when $\nu = 0$, this fact motivates expanding G for $\nu \ll 1$ as

$$G(\mathbf{x}; \mathbf{x}_i) \sim \nu^{-1} G_{-1}(\mathbf{x}; \mathbf{x}_i) + G_0(\mathbf{x}; \mathbf{x}_i) + \nu G_1(\mathbf{x}; \mathbf{x}_i) + \cdots\,, \tag{5.2}$$

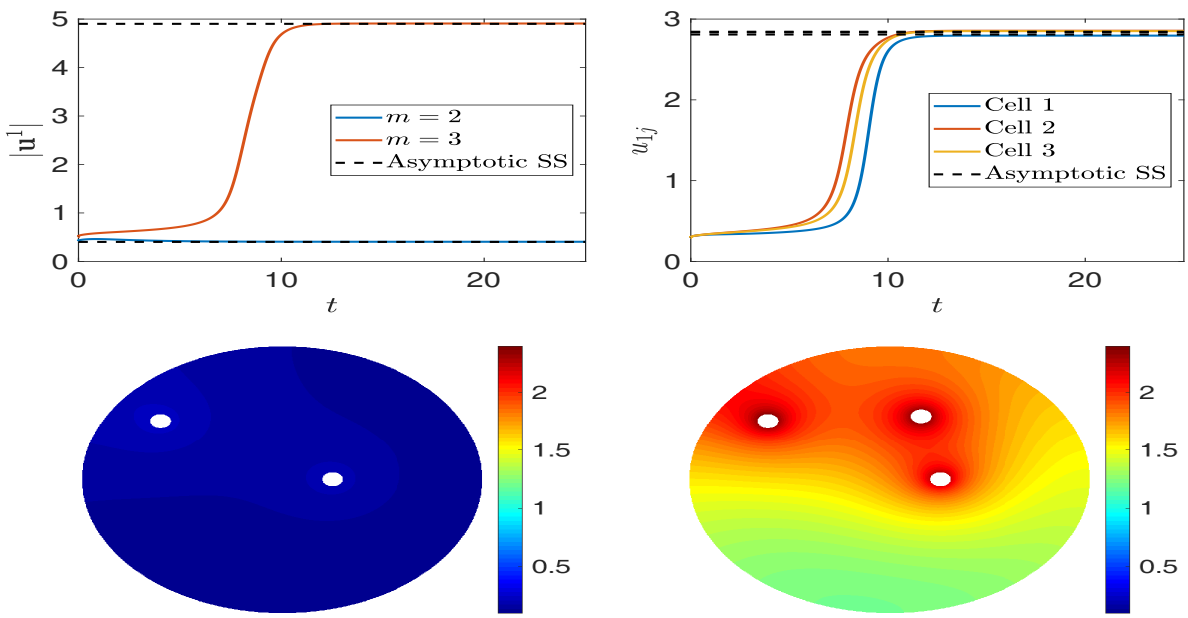

Figure 4.7: FlexPDE [12] numerical results for the cell-bulk system (1.3) and (1.5) for a non-ring pattern of cells. Top row: L^2-norm of $\mathbf{u}^1$ for $m = 2, 3$ (left) as well as its components u_{1j} for $m = 3$ (right) versus t. The steady-states predicted by the asymptotic theory in Principal Result 7 are the dashed lines. Bottom row: snapshot of the bulk solution near equilibrium for $m = 2$ (left) and $m = 3$ (right). The cells are in the upregulated state when $m = 3$. Parameters as in (4.15) and Table 1. Cell locations are $\boldsymbol{x}_1 = (0.25, 0)^T$, $\boldsymbol{x}_2 = 0.75\,(\cos(4\pi/5), \sin(4\pi/5))^T$ and $\boldsymbol{x}_3 = 0.5\,(\cos(2\pi/5), \sin(2\pi/5))^T$.

where G_{-1} is a constant. Upon substituting (5.2) into (5.1), we collect powers of ν to obtain that

$$\Delta G_0 = \frac{\gamma}{D_0} G_{-1} - \delta(\mathbf{x} - \mathbf{x}_i)\,, \quad \mathbf{x} \in \Omega\,; \qquad \partial_n G_0 = -\frac{\kappa}{D_0} G_{-1}\,, \quad \mathbf{x} \in \partial\Omega\,, \tag{5.3a}$$

$$\Delta G_1 = \frac{\gamma}{D_0} G_0\,, \quad \mathbf{x} \in \Omega\,; \qquad \partial_n G_1 = -\frac{\kappa}{D_0} G_0\,, \quad \mathbf{x} \in \partial\Omega\,. \tag{5.3b}$$

By using the divergence theorem on (5.3a), we readily identify the constant G_{-1} as

$$G_{-1} = \frac{D_0}{\beta}\,, \qquad \text{where} \qquad \beta \equiv \gamma|\Omega| + \kappa|\partial\Omega|\,. \tag{5.4}$$

Here $|\Omega|$ and $|\partial\Omega|$ are the area of Ω and the perimeter of $\partial\Omega$, respectively. Similarly, we can use the divergence theorem on (5.3b) to obtain an integral constraint on G_0. By using these constraints, we obtain from (5.3a) that G_0 is the unique solution to

$$\Delta G_0 = \frac{\gamma}{\beta} - \delta(\mathbf{x} - \mathbf{x}_i)\,, \quad \mathbf{x} \in \Omega\,; \qquad \partial_n G_0 = -\frac{\kappa}{\beta}\,, \quad \mathbf{x} \in \partial\Omega\,; \qquad \gamma \int_\Omega G_0\, d\mathbf{x} = -\kappa \int_{\partial\Omega} G_0\, ds_{\mathbf{x}}\,. \tag{5.5}$$

The unique solution to (5.5) is decomposed as

$$G_0(\mathbf{x}; \mathbf{x}_i) = G_N(\mathbf{x}; \mathbf{x}_i) - \frac{\kappa}{\beta} H(\mathbf{x}) + \overline{G}_0\,, \tag{5.6}$$

where G_N is the Neumann Green's function satisfying (3.5), the constant $\overline{G}_0$ is the spatial average of G_0, while $H(\mathbf{x})$ is the unique solution to

$$\Delta H = \frac{|\partial\Omega|}{|\Omega|}\,, \quad \mathbf{x}\in\Omega\,; \qquad \partial_n H = 1\,, \quad \mathbf{x}\in\partial\Omega\,; \qquad \int_\Omega H d\mathbf{x} = 0\,. \tag{5.7}$$

By using Green's second identity, together with the reciprocity of the Green's function, we obtain that

$$H(\mathbf{x}) = \int_{\partial\Omega} G_N(\mathbf{x};\xi)\, ds_\xi = \int_{\partial\Omega} G_N(\xi;\mathbf{x})\, ds_\xi\,. \tag{5.8}$$

In (5.6), the constant $\overline{G}_0$ depends on $\mathbf{x}_i$, and is determined by substituting (5.6) into the integral constraint in (5.5). This yields that

$$\overline{G}_0 = -\frac{\kappa}{\beta} H(\mathbf{x}_i) + \frac{\kappa^2}{\beta^2}|\partial\Omega|\,\overline{H}_{\partial\Omega}\,, \qquad \text{where} \qquad \overline{H}_{\partial\Omega} \equiv \frac{1}{|\partial\Omega|}\int_{\partial\Omega} H\, ds_{\mathbf{x}}\,. \tag{5.9}$$

Then, upon substituting (5.4), (5.6) and (5.9), into (5.2), we obtain the following two-term result for G and the associated Green's matrix $\mathcal{G}$, which is valid for $D = D_0/\nu \gg 1$:

Lemma 5.1. *For $D = D_0/\nu \gg 1$, we have for $\nu \ll 1$ that the Green's function in (5.1) satisfies*

$$G(\mathbf{x};\mathbf{x}_i) \sim \frac{D_0}{\nu\beta} + G_N(\mathbf{x};\mathbf{x}_i) - \frac{\kappa}{\beta}\left(H(\mathbf{x}) + H(\mathbf{x}_i)\right) + \frac{\kappa^2}{\beta^2}|\partial\Omega|\,\overline{H}_{\partial\Omega} + \mathcal{O}(\nu)\,, \tag{5.10}$$

where G_N is the Neumann Green's function, $H(\mathbf{x})$ is given in (5.8), and $\beta = \gamma|\Omega| + \kappa|\partial\Omega|$. The corresponding Green's matrix $\mathcal{G}$, with matrix entries $(\mathcal{G})_{ji} = (\mathcal{G})_{ij} = G(\mathbf{x}_j;\mathbf{x}_i)$ for $i \neq j$ and $(\mathcal{G})_{ii} = R_i$, has the two-term asymptotics

$$\mathcal{G} = \frac{mD_0}{\nu\beta} E + \mathcal{G}_N - \frac{\kappa}{\beta}\left(\mathbf{H}\mathbf{e}^T + \mathbf{e}\mathbf{H}^T\right) + \frac{m\kappa^2}{\beta^2}|\partial\Omega|\,\overline{H}_{\partial\Omega}\, E + \mathcal{O}(\nu)\,, \tag{5.11}$$

where $\mathcal{G}_N$ is the Neumann Green's matrix, $\mathbf{H} \equiv (H(\mathbf{x}_1),\ldots,H(\mathbf{x}_m))^T$, $E \equiv m^{-1}\mathbf{e}\mathbf{e}^T$, and $\mathbf{e} \equiv (1,\ldots,1)^T$.

By using (5.11) in (4.6), we obtain the following main result characterizing QS behavior for the cell-bulk model (1.3) and (1.5) with a collection of identical cells in the $D = D_0/\nu \gg 1$ regime:

Principal Result 8. *Let $\varepsilon \to 0$ and assume that $D = D_0/\nu \gg 1$ where $\nu \equiv -1/\log\varepsilon$. Then, for a collection of m identical cells and with Lux ODE kinetics (1.5), the NAS (4.6) in Principal Result 6 for the source strengths $\mathbf{S}$ and the intracellular components $\mathbf{u}^3$ reduces to*

$$\left[\left(1 + \frac{D_0}{d_1} + \frac{2\pi d_2 D_0}{d_1\kappa_{2A}}\right) I + \frac{2\pi m D_0}{\beta} E + 2\pi\nu\mathcal{J} + \mathcal{O}(\nu^2)\right]\mathbf{S} = -\frac{\nu d_2}{d_1\kappa_{2A}}(c\mathbf{e} + \kappa_{1A}\mathbf{b})\,, \tag{5.12a}$$

$$Q(u_{3j}, S_j) \equiv \frac{1}{\kappa_{2A}\kappa_{2R}\kappa_5}\left[c + \frac{2\pi D_0}{\nu} S_j + \frac{\kappa_{1A} u_{3j}^2}{\kappa_A + u_{3j}^2}\right]\left[1 + \frac{\kappa_{1R} u_{3j}^2}{\kappa_R + u_{3j}^2}\right] - u_{3j} = 0\,, \quad j = 1,\ldots,m\,, \tag{5.12b}$$

where $\mathbf{b} = \mathbf{b}(\mathbf{u}^3)$ is defined in (4.1d), while $\mathcal{J}$ is defined by

$$\mathcal{J} \equiv \mathcal{G}_N - \frac{\kappa}{\beta}\left(\mathbf{H}\mathbf{e}^T + \mathbf{e}\mathbf{H}^T\right) + \frac{m\kappa^2}{\beta^2}|\partial\Omega|\,\overline{H}_{\partial\Omega}\, E\,. \tag{5.13}$$

The steady-state bulk concentration in the outer region, U, and the other steady-state components of $\mathbf{u}_j$, for $j = 1, \ldots, m$, are determined in terms of $\mathbf{S}$ and $\mathbf{u}^3$ as

$$U = -2\pi \sum_{i=1}^{m} S_i G(\mathbf{x}; \mathbf{x}_i) = -\frac{2\pi D_0}{\nu\beta} \sum_{i=1}^{m} S_i + \mathcal{O}(1)\,, \tag{5.14a}$$

$$u_{1j} = \frac{1}{\kappa_{2A_j}} \left(c + \frac{2\pi D_0}{\nu} S_j + \frac{\kappa_{1A} u_{3j}^2}{\kappa_A + u_{3j}^2} \right), \quad u_{2j} = \frac{1}{\kappa_{2R}} \left(1 + \frac{\kappa_{1R} u_{3j}^2}{\kappa_R + u_{3j}^2} \right), \quad u_{4j} = \frac{\kappa_3}{\kappa_4} u_{3j}^2\,. \tag{5.14b}$$

Moreover, by neglecting $\mathcal{J}$ in (5.12a), we conclude, for any spatial configuration of cells, that there is a branch of solutions of (5.12) for which $\mathbf{S} = \nu S_c \mathbf{e} + \mathcal{O}(\nu^2)$ and $u_{3j} = u_3 + \mathcal{O}(\nu)$ for all $j = 1, \ldots, m$, where

$$S_c = -\frac{d_2}{d_1 \kappa_{2A}} \left(c + \frac{\kappa_{1A} u_3^2}{\kappa_A + u_3^2} \right) \left(1 + \frac{D_0}{d_1} + \frac{2\pi d_2 D_0}{d_1 \kappa_{2A}} + \frac{2\pi m D_0}{\beta} \right)^{-1}. \tag{5.15}$$

On this branch, (5.12) simplifies to a single algebraic equation for u_3, given by $q_{\mathit{eff}}(u_3) = 0$, where

$$q_{\mathit{eff}}(u_3) \equiv \frac{1}{\kappa_{\mathit{eff}}(m) \kappa_{2R} \kappa_5} \left[c + \frac{\kappa_{1A} u_3^2}{\kappa_A + u_3^2} \right] \left[1 + \frac{\kappa_{1R} u_3^2}{\kappa_R + u_3^2} \right] - u_3\,, \tag{5.16}$$

with

$$\kappa_{\mathit{eff}}(m) \equiv \kappa_{2A} + \frac{2\pi D_0 d_2/d_1}{1 + \frac{D_0}{d_1} + \left(\frac{2\pi D_0}{\beta} \right) m}\,. \tag{5.17}$$

In addition, if $q_{\mathit{eff}}(u_3)$ has saddle-node bifurcation points at $\kappa_{\mathit{eff}} = \kappa_c$ such that locally there are no equilibria for $\kappa_{\mathit{eff}} < \kappa_c$ ($\kappa_{\mathit{eff}} > \kappa_c$), then a transition to the upregulated (downregulated) state occurs at the critical cell population $m = m_c$, given in terms of the ceiling $\lceil \cdot \rceil$ and floor $\lfloor \cdot \rfloor$ functions by

$$m_c = \left\lceil \frac{\beta}{d_1} \left(\frac{d_2}{\kappa_c - \kappa_{2A}} - \frac{d_1}{2\pi D_0} - \frac{1}{2\pi} \right) \right\rceil, \qquad \left(m_c = \left\lfloor \frac{\beta}{d_1} \left(\frac{d_2}{\kappa_c - \kappa_{2A}} - \frac{d_1}{2\pi D_0} - \frac{1}{2\pi} \right) \right\rfloor \right). \tag{5.18}$$

Proof. First, we substitute the large D expansion (5.10) into the NAS (4.6) to obtain (5.12) and (5.13). Upon neglecting $\mathcal{J}$ in (5.12), (5.12) admits a solution of the form $\mathbf{S} = \nu S_c \mathbf{e}$ and $\mathbf{u}^3 = u_3 \mathbf{e} + \mathcal{O}(\nu)$, where S_c is given in (5.15), for any spatial configuration of cells. Upon substituting $S_j = S_c$ and $u_{3j} = u_3$ into (5.12b), we obtain (5.16) and (5.17). Since $q_{\text{eff}}(u_3)$ has the same form as $q(u_3)$, as defined in (2.3), but with κ_{2A} replaced by $\kappa_{\text{eff}}(m)$, it follows from §2 (see Fig. 2.1) that the solution branches of $q_{\text{eff}}(u_3) = 0$ exhibit saddle-node bifurcations at critical thresholds κ_c of the parameter κ_{eff}. Since m is an integer and κ_{eff} is a decreasing function of m, we obtain (5.18) after isolating m in (5.17). ∎

Our main result in (5.18) characterizes the leading-order critical population level for QS behavior, which is independent of the spatial configuration of cells. In (5.18), the saddle-node bifurcation point, κ_c, can be computed numerically by solving $q(u_3) = 0$ and $q'(u_3) = 0$ simultaneously for u_3 and κ_c. We remark that the two sources of AI loss, specifically the bulk decay and loss through the boundary, are indistinguishable processes to leading order. The loss coefficients γ and κ associated with the bulk degradation are contained in an aggregate loss parameter $\beta \equiv \gamma|\Omega| + \kappa|\partial\Omega|$. Observe from (5.17) that $\kappa_{\text{eff}} \to \kappa_{2A}$ as $\beta \to 0$, which indicates that bulk loss is required for QS behavior. We remark that an $\mathcal{O}(\nu)$ correction term to this leading-order QS threshold in (5.18), which would depend on the spatial pattern of cells, can in principle be calculated by including the matrix $\mathcal{J}$ in (5.12a). Our next result provides this higher order characterization of the QS threshold for a ring pattern in the unit disk.

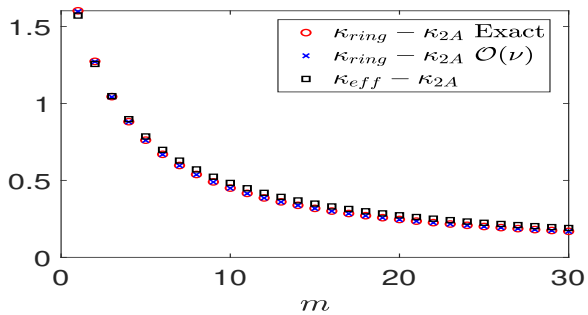

Figure 5.1: Comparison of $\kappa_{\rm ring}(m) - \kappa_{2A}$ and the leading-order result $\kappa_{\rm eff}(m) - \kappa_{2A}$, as given in (4.9) and (5.17), respectively. The exact $\kappa_{\rm ring} - \kappa_{2A}$, indicated by the red circles, is computed using the exact eigenvalue g_1 of $\mathcal{G}$. The blue crosses denote $\kappa_{\rm ring} - \kappa_{2A}$ using the two-term result for g_1 in (5.19). The values of $\kappa_{\rm ring} - \kappa_{2A}$ depend on the cell locations through the ring radius r_0, while $\kappa_{\rm eff} - \kappa_{2A}$, denoted by the black squares, is independent of the cell locations. Parameters are $D = \nu^{-1}$, $\nu = -1/\log\varepsilon$, $\varepsilon = 0.01$, $\gamma = 1$, $\kappa = 0.5$, $d_1 = d_2 = 0.5$, and $r_0 = 0.3$.

Principal Result 9. *Let $\varepsilon \to 0$ and $D = D_0/\nu \gg 1$ where $\nu \equiv -1/\log\varepsilon$. Consider a ring pattern of m identical cells equally-spaced on a ring of radius r_0 concentric within the unit disk. Then, the eigenvalue $g_1(m)$ of the Green's matrix $\mathcal{G}$ for the effective parameter κ_{ring} in (4.9) has the two-term expansion*

$$g_1(m) = \frac{mD_0}{\nu\beta} + g_{N1}(m) - \frac{m\kappa}{\beta}\left(r_0^2 - \frac{1}{2}\right) + \frac{m\pi\kappa^2}{2\beta^2} + \mathcal{O}(\nu)\,, \quad \text{where} \quad \beta \equiv \gamma|\Omega| + \kappa|\partial\Omega|\,. \tag{5.19a}$$

Here g_{N1} is the eigenvalue $\mathcal{G}_N\mathbf{e} = g_{N1}\mathbf{e}$ of the Neumann Green's matrix $\mathcal{G}_N$, given by (see (5.4) of [23])

$$g_{N1}(m) = \frac{1}{2\pi}\left(-m\log\left(mr_0^{m-1}\right) - \log\left(1 - r_0^{2m}\right) + mr_0^2 - \frac{3m}{4}\right)\,. \tag{5.19b}$$

Proof. Since $\kappa_{\rm ring}$, as given in (4.9) of Principal Result 6 for a ring pattern, is accurate to all orders in ν for any $D > 0$, it remains valid when $D = D_0/\nu$. This effective parameter depends on $g_1(m)$, as given by $\mathcal{G}\mathbf{e} = g_1\mathbf{e}$. To derive (5.19) for $g_1(m)$, we use (5.11) to obtain a two-term expansion for $\mathcal{G}$ for a ring pattern. For the unit disk, we calculate from (5.7) and (5.9) that

$$H(\mathbf{x}) = \frac{1}{2}|\mathbf{x}|^2 - \frac{1}{4}\,, \qquad \overline{H}_{\partial\Omega} = \frac{1}{4}\,, \qquad H(\mathbf{x}_i) = \frac{1}{2}r_0^2 - \frac{1}{4}\,, \quad \text{for} \quad i = 1, \ldots, m\,. \tag{5.20}$$

By using (5.20) and $|\partial\Omega| = 2\pi$ in (5.11), we obtain for a ring pattern that

$$\mathcal{G} = \frac{mD_0}{\nu\beta}E + \mathcal{G}_N - \frac{m\kappa}{\beta}\left(r_0^2 - \frac{1}{2}\right)E + \frac{m\pi\kappa^2}{2\beta^2}E + \mathcal{O}(\nu)\,. \tag{5.21}$$

Finally, to obtain (5.19) for $g_1(m)$, we simply calculate $\mathcal{G}\mathbf{e}$ using (5.21), $\mathcal{G}_N\mathbf{e} = g_{N1}\mathbf{e}$, and $E\mathbf{e} = \mathbf{e}$. ■

For the $D = D_0/\nu \gg 1$ regime, the effective parameter $\kappa_{\rm ring}$ in (4.9) for a ring pattern, which depends on $g_1(m)$ from (5.19), shows that QS behavior can be triggered by both increasing the population, m, as well as by changing the cell locations by varying the ring radius r_0. The critical population, m_c, is reached when $\kappa_{\rm ring}$ crosses the saddle-node bifurcation point at κ_c.

In Fig. 5.1 we compare values of $\kappa_{\rm ring}(m) - \kappa_{2A}$ from (4.9) as calculated by using either the two-term result (5.19) for g_1 or the exact result for the eigenvalue of $\mathcal{G}$, as obtained by using (B.2) of Appendix B to

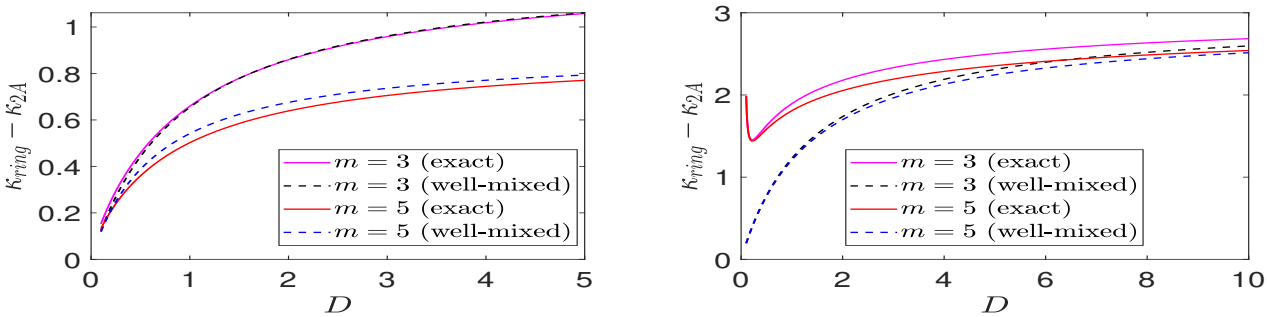

(a) $\varepsilon = 0.01$, $\kappa = 0.5$, $\gamma = 1$

(b) $\varepsilon = 0.05$, $\kappa = 5$, $\gamma = 40$

Figure 5.2: Comparison of $\kappa_{\text{ring}}(m) - \kappa_{2A}$ versus D, as given in (4.9), for a ring pattern with either $m = 3$ or $m = 5$ cells, and the corresponding result for the well-mixed $D = D_0/\nu$ regime, where the two-term result for g_1 in (5.19) is used. As D increases, the two results agree as expected. Parameters are $d_1 = d_2 = 0.5$, and ring radius $r_0 = 0.3$. Left panel: $\kappa_{\text{ring}}(m) - \kappa_{2A}$ is monotone increasing in D when $\varepsilon = 0.01$, $\kappa = 0.5$, and $\gamma = 1$. Right panel: $\kappa_{\text{ring}}(m) - \kappa_{2A}$ is no longer monotone in D with a stronger bulk loss where $\varepsilon = 0.05$, $\kappa = 5$, and $\gamma = 40$.

calculate the matrix entries of $\mathcal{G}$. The parameter values used are in the caption of Fig. 5.1. The excellent agreement observed in Fig. 5.1 shows that the expansion (5.19) for g_1 is a reasonable approximation in the distinguished limit. In Fig. 5.1, we also plot the leading-order result $\kappa_{\text{eff}}(m) - \kappa_{2A}$ in (5.17) for the same parameters. Since with $\varepsilon = 0.01$ we get $\nu \approx 0.217$, which is not very small, we observe from Fig. 5.1, as expected, that κ_{eff} provides only a moderately good prediction for κ_{ring}.

For a ring pattern with either $m = 3$ or $m = 5$ cells, in Fig. 5.2a we compare $\kappa_{\text{ring}}(m) - \kappa_{2A}$ versus D, as given in (4.9), with the corresponding result for the $D = D_0/\nu \gg 1$ regime, where the two-term result for g_1 in (5.19) is used. The parameter values are the same as in the caption of Fig. 5.1. We observe, as expected, that the two results agree more closely as D increases. Moreover, since $\kappa_{\text{ring}}(m) - \kappa_{2A}$ is monotone increasing in D for both $m = 3$ and $m = 5$, we conclude that the QS transition is harder to achieve as D decreases. However, as observed in Fig. 5.2b, when the bulk loss is stronger, then $\kappa_{\text{ring}}(m) - \kappa_{2A}$ is no longer monotone on the $D = \mathcal{O}(1)$ regime. This implies that there an optimal value of D, corresponding to where $\kappa_{\text{ring}}(m) - \kappa_{2A}$ is minimized, for obtaining a QS transition. For D larger than this critical value, the bulk signal that provides the inter-cell communication is quickly degraded, while for D very small, the bulk signal remains confined near each cell and little inter-cellular communication occurs.

To compare our asymptotic results with corresponding full numerical results computed from (1.3) and (1.5), we need to asymptotically calculate the average bulk concentration $\overline{U}$, defined by

$$\overline{U} \equiv \frac{1}{|\Omega \setminus \Omega_\varepsilon|} \int_{\Omega \setminus \Omega_\varepsilon} U \, d\mathbf{x} \,, \qquad \text{where} \qquad \Omega_\varepsilon \equiv \cup_{j=1}^{m} \Omega_{\varepsilon_j} \,. \tag{5.22}$$

Since $|\Omega \setminus \Omega_\varepsilon| = |\Omega| + \mathcal{O}(\varepsilon^2)$, we get $\overline{U} \sim |\Omega|^{-1} \int_\Omega U d\mathbf{x} + \mathcal{O}(\varepsilon^2)$. Then, we use (5.14a), the two-term expansion (5.10) for G, and $\int_\Omega G_N \, d\mathbf{x} = \int_\Omega H \, d\mathbf{x} = 0$, to calculate the steady-state bulk average, $\overline{U}_e$, as

$$\overline{U}_e \sim -2\pi \sum_{i=1}^{m} S_i \left(\frac{D_0}{\nu\beta} - \frac{\kappa}{\beta} H(\mathbf{x}_i) + \frac{\kappa^2}{\beta^2} |\partial\Omega| \, \overline{H}_{\partial\Omega} \right) \,, \quad \text{for} \quad D = D_0/\nu \gg 1 \,, \tag{5.23}$$

which is valid for any spatial arrangement of cells in an arbitrary domain Ω. For a ring pattern in the unit disk, for which there is a branch of equilibria where $\mathbf{S} = \nu S_c \mathbf{e}$, with S_c given in (5.15), we use (5.20) to

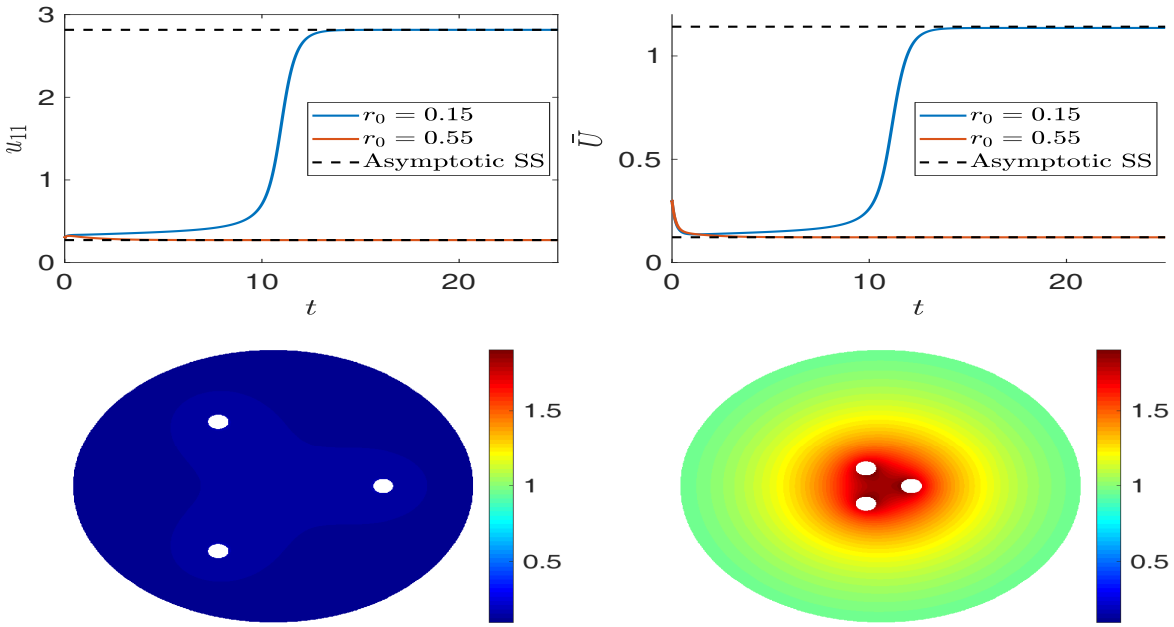

Figure 5.3: FlexPDE [12] numerical solutions of the cell-bulk system (1.3) and (1.5) for $m = 3$ cells equally-spaced on a ring of radius r_0 in the unit disk, with either $r_0 = 0.15$ or $r_0 = 0.55$. The other parameters are given in (5.25) and Table 1. Top row: u_{11} (left) and the bulk average $\overline{U}$ (right) versus t, along with the predicted steady-states from the asymptotic theory (dashed lines). Observe that when $r_0 = 0.15$, where the cells are more clustered, QS behavior occurs as a transition to the upregulated steady-state. Bottom row: snapshot of the bulk solution near steady-state for $r_0 = 0.55$ (left) and $r_0 = 0.15$ (right).

evaluate H and $\overline{H}_{\partial\Omega}$ in (5.23), with the result

$$\overline{U}_e \sim -2\pi m S_c \left[\frac{D_0}{\beta} - \nu \frac{\kappa}{2\beta} \left(r_0^2 - \frac{1}{2} \right) + \nu \frac{\pi \kappa^2}{2\beta^2} \right], \quad \text{for} \quad D = D_0/\nu \gg 1 . \tag{5.24}$$

For a ring pattern in the unit disk, we now compare results from our asymptotic theory with full FlexPDE [12] results computed from the cell-bulk system (1.3) and (1.5). The parameters are chosen as

$$D_0 = 1 , \quad \varepsilon = 0.05 , \quad \gamma = \kappa = 1 , \quad d_1 = d_2 = 0.5 , \quad m = 3 , \quad \kappa_{2A} = 5 , \quad \kappa_{DR} = 0.0125 , \tag{5.25}$$

with the other parameters as in Table 1. For this parameter set, the effective bifurcation parameters are

$$\kappa_{\text{ring}}(3) \approx 6.12 , \quad \text{for} \quad r_0 = 0.15 ; \qquad \kappa_{\text{ring}}(3) \approx 6.30 , \quad \text{for} \quad r_0 = 0.55 . \tag{5.26}$$

Since the fold point occurs at $\kappa_c \approx 6.16$, the asymptotic theory predicts that the downregulated state does not exist when $r_0 = 0.15$, and that a time-dependent transition to the upregulated state should occur for this more clustered arrangement of cells. This theoretical prediction is confirmed in Fig. 5.3 where results from the FlexPDE [12] simulations of (1.3) and (1.5) are shown with $m = 3$ cells for the ring radii $r_0 = 0.15$ and $r_0 = 0.55$. The initial conditions for the FlexPDE simulations were taken to be close to the downregulated state predicted from Principal Results 6, 8, and (9) near the fold point. The steady-states shown in Fig. 5.3 are obtained by solving $q_{\text{eff}} = 0$ numerically and then using (5.24) and (5.14b).

5.2. Asymptotic reduction to an ODE-DAE system. For $D = D_0/\nu \gg 1$, we now use the method of matched asymptotic expansions to reduce the cell-bulk ODE-PDE model (1.3)–(1.5) into an ODE-DAE system for the intracellular species and the average bulk concentration. In our analysis a 'partial summing' technique is used where the leading order term contains the average bulk concentration accurate up to $\mathcal{O}(\nu)$, instead of the usual $\mathcal{O}(1)$. Since a similar analysis was given in §3 of [19] for a Neumann boundary condition on $\partial\Omega$, we only provide highlights of the derivation of the ODE-DAE system.

We begin by deriving an ODE, without approximation, for the average bulk concentration $\overline{U} = \overline{U}(t;\nu)$, defined by (5.22). By integrating the bulk PDE in (1.3a) and using the divergence theorem, we obtain

$$\overline{U}_t + \gamma\overline{U} = -\frac{\kappa}{|\Omega\setminus\Omega_\varepsilon|}\int_{\partial\Omega} U\,ds_{\mathbf{x}} + \frac{2\pi}{|\Omega\setminus\Omega_\varepsilon|}\sum_{j=1}^{m}\left(d_{2j}u_{1j} - \frac{d_{1j}}{2\pi\varepsilon}\int_{\partial\Omega_{\varepsilon_j}} U\,ds_{\mathbf{x}}\right). \tag{5.27}$$

In the analysis below, the goal is to estimate U on $\partial\Omega$ as well as on each cell boundary $\partial\Omega_{\varepsilon_j}$.

In the inner region near each cell we introduce the local variables $\mathbf{y}_j \equiv \varepsilon^{-1}(\mathbf{x}-\mathbf{x}_j)$ and $U_j(\mathbf{y}_j,t;\nu) = U(\mathbf{x}_j+\varepsilon\mathbf{y}_j,t;\nu)$. It is readily seen that the leading order inner problem for the jth cell is the steady-state problem $\Delta_{\mathbf{y}_j}U_j = 0$ for $\rho = |\mathbf{y}_j| \geq 1$, subject to $D_0\partial_\rho U_j = \nu(d_{1j}U_j - d_{2j}u_{1j})$ on $\rho = 1$. The radially symmetric solution to this problem is written in terms of an unknown constant p_j as

$$U_j = \nu p_j \log\rho + U_j^0\,, \qquad \text{with} \qquad U_j^0 = \frac{D_0}{d_{1j}}p_j + \frac{d_{2j}}{d_{1j}}u_{1j}\,, \quad \text{for} \quad j = 1,\ldots,m\,, \tag{5.28}$$

where $U_j = U_j^0$ on $\rho = 1$. By substituting (5.28) into (1.4) and (5.27), and by using $|\Omega\backslash\Omega_\varepsilon| = |\Omega| + \mathcal{O}(\varepsilon^2)$, we obtain in terms of $\mathbf{p} \equiv (p_1,\ldots,p_m)^T$ that the intracellular species and the bulk average satisfies

$$\frac{d\mathbf{u}_j}{dt} \sim \mathbf{F}_j(\mathbf{u}_j) + 2\pi D_0 p_j\mathbf{e}_1\,, \quad j = 1,\ldots,m\,; \qquad \overline{U}_t + \gamma\overline{U} \sim -\frac{\kappa}{|\Omega|}\int_{\partial\Omega} U\,ds_{\mathbf{x}} - \frac{2\pi D_0}{|\Omega|}\mathbf{e}^T\mathbf{p}\,. \tag{5.29}$$

From (1.3a), together with the far-field behavior of U_j in (5.28) when written in the outer variable, we obtain that the bulk solution in the outer region satisfies

$$U_t = \frac{D_0}{\nu}\Delta_{\mathbf{x}}U - \gamma U\,, \quad \mathbf{x}\in\Omega\setminus\{\mathbf{x}_1,\ldots,\mathbf{x}_m\}\,; \qquad D_0\partial_n U = -\kappa\nu U\,, \quad \mathbf{x}\in\partial\Omega\,, \tag{5.30a}$$

$$U \sim \nu p_j\log|\mathbf{x}-\mathbf{x}_j| + p_j\left(1+\frac{D_0}{d_{1j}}\right) + \frac{d_{2j}}{d_{1j}}u_{1j}\,, \quad \text{as} \quad \mathbf{x}\to\mathbf{x}_j\,, \quad j = 1,\ldots,m\,. \tag{5.30b}$$

We now introduce our first approximation in ν by expanding this outer solution as

$$U(\mathbf{x},t) = \overline{U}(t;\nu) + \frac{\nu}{D_0}U_1(\mathbf{x},t;\nu) + \ldots\,. \tag{5.31}$$

We allow the terms in this series to depend on ν but enforce that $\overline{U}$ and U_1 are $\mathcal{O}(1)$ so that the series is not disordered. In the analysis below, we will determine $\overline{U}$ accurate to $\mathcal{O}(\nu)$, instead of the usual $\mathcal{O}(1)$, by employing a 'partial summing' technique. It is important here to clarify that $\overline{U}$ in the series above is the same $\overline{U}$ as in (5.27), which is accurate to *all* powers of ν. As such we impose $\overline{U}_1 \equiv |\Omega|^{-1}\int_\Omega U_1\,d\mathbf{x} = 0$ for (5.31). However, in the analysis below we will truncate the approximation during the matching process, resulting in U_j^0 (or equivalently p_j) being accurate to $\mathcal{O}(\nu)$. In this way, the first term in (5.31) will approximate U to $\mathcal{O}(1)$ as usual, but the average will have an improved accuracy to order $\mathcal{O}(\nu)$.

Upon substituting (5.31) into (5.30) we obtain that U_1 satisfies:

$$\Delta_{\mathbf{x}} U_1 = \overline{U}_t + \gamma \overline{U}\,, \qquad \mathbf{x} \in \Omega \setminus \{\mathbf{x}_1, \ldots, \mathbf{x}_m\}\,; \qquad \partial_n U_1 = -\kappa \overline{U} - \frac{\kappa}{D_0} \nu U_1\,, \quad \mathbf{x} \in \partial\Omega\,, \tag{5.32a}$$

$$U_1 \sim D_0 p_j \log|\mathbf{x} - \mathbf{x}_j| + \frac{D_0}{\nu}\left[p_j\left(1 + \frac{D_0}{d_{1j}}\right) + \frac{d_{2j}}{d_{1j}} u_{1j}\right] - \frac{D_0}{\nu} U\,, \quad \text{as} \quad \mathbf{x} \to \mathbf{x}_j\,, \quad j = 1, \ldots, m\,. \tag{5.32b}$$

By using the divergence theorem on (5.32) we recover (5.29) for $\overline{U}$. Next, we neglect the $\mathcal{O}(\nu)$ term in the boundary condition in (5.32a), and then decompose the solution to (5.32) as

$$U_1 = -2\pi D_0 \sum_{i=1}^{m} p_i G_N(\mathbf{x}; \mathbf{x}_i) - \kappa \overline{U} H(\mathbf{x}) + \mathcal{O}(\nu)\,, \tag{5.33}$$

where G_N is the Neumann Green's function satisfying (3.5), while $H(\mathbf{x})$ is the unique solution to (5.7), as given by (5.8). By expanding U_1 as $\mathbf{x} \to \mathbf{x}_j$, and comparing with the required behavior in (5.32b), we obtain a linear algebraic system for $\mathbf{p}$, which we write in matrix form as

$$\left(I + D_0 \mathcal{D}_1 + 2\pi\nu \mathcal{G}_N\right) \mathbf{p} = \overline{U}\mathbf{e} - \mathcal{D}_{21}\mathbf{u}^1 - \frac{\kappa}{D_0}\nu \overline{U}\mathbf{H} + \mathcal{O}(\nu^2)\,, \tag{5.34}$$

where $\mathbf{u}^1 \equiv (u_{11}, \ldots, u_{1m})^T$. Here $\mathcal{G}_N$ is the Neumann Green's matrix, $\mathcal{D}_1$ and $\mathcal{D}_{12}$ are the diagonal matrices defined in (3.7b), while $\mathbf{H} \equiv (H(\mathbf{x}_1), \ldots, H(\mathbf{x}_m))^T$. By neglecting the $\mathcal{O}(\nu^2)$ term in (5.34), we obtain $\mathbf{p}$, accurate to $\mathcal{O}(\nu)$, as needed in (5.29). Finally, we use $U \sim \overline{U} + \nu U_1/D_0$, with U_1 given in (5.33), to estimate the term $\int_{\partial\Omega} U\, dS_{\mathbf{x}}$ in (5.29) as

$$\int_{\partial\Omega} U\, ds_{\mathbf{x}} \sim \overline{U}|\partial\Omega| - 2\pi\nu \mathbf{H}^T \mathbf{p} - \frac{\kappa}{D_0}\nu \overline{U}|\partial\Omega|\, \overline{H}_{\partial\Omega}\,, \qquad \text{where} \qquad \overline{H}_{\partial\Omega} \equiv \frac{1}{|\partial\Omega|}\int_{\partial\Omega} H\, ds_{\mathbf{x}}\,. \tag{5.35}$$

The ODE-DAE system, obtained by substituting (5.34) and (5.35) in (5.29), is summarized as follows:

Principal Result 10. *For $D = D_0/\nu \gg 1$, the cell-bulk model (1.3) and (1.4) reduces to a finite-dimensional ODE-DAE system, which is accurate up to and including terms of order $\mathcal{O}(\nu)$, given by*

$$\overline{U}_t + \left(\frac{\beta}{|\Omega|} - \nu\frac{\kappa^2}{D_0}\frac{|\partial\Omega|}{|\Omega|}\overline{H}_{\partial\Omega}\right)\overline{U} = -\frac{2\pi D_0}{|\Omega|}\mathbf{e}^T\mathbf{p} + \frac{2\pi\kappa}{|\Omega|}\nu \mathbf{H}^T\mathbf{p}\,, \tag{5.36a}$$

$$\frac{d\mathbf{u}_j}{dt} = \mathbf{F}_j(\mathbf{u}_j) + 2\pi D_0 \mathbf{e}_1 p_j\,, \qquad j = 1, \ldots, m\,, \tag{5.36b}$$

$$\left(I + D_0\mathcal{D}_1 + 2\pi\nu\mathcal{G}_N\right)\mathbf{p} = \overline{U}\mathbf{e} - \mathcal{D}_{21}\mathbf{u}^1 - \frac{\kappa}{D_0}\nu\overline{U}\mathbf{H}\,, \tag{5.36c}$$

where $\beta \equiv \gamma|\Omega| + \kappa|\partial\Omega|$ is the aggregate bulk loss parameter. Here $\mathbf{H} \equiv (H(\mathbf{x}_1), \ldots, H(\mathbf{x}_m))^T$ is defined by (5.7) and (5.8), while the boundary average $\overline{H}_{\partial\Omega}$ is given by (5.9). For $\nu \ll 1$, (5.36c) yields

$$\boldsymbol{p} \approx \frac{1}{D_0}\mathcal{C}\left(\overline{U}\boldsymbol{e} - \mathcal{D}_{21}\mathbf{u}^1 - \frac{\kappa}{D_0}\nu\overline{U}\mathbf{H}\right) + \mathcal{O}(\nu^2)\,, \tag{5.37a}$$

$$\mathcal{C} \equiv \left(I - \frac{2\pi\nu}{D_0}\tilde{\mathcal{D}}_1^{-1}\mathcal{G}_N\right)\tilde{\mathcal{D}}_1^{-1}\,, \quad \textit{where} \quad \tilde{\mathcal{D}}_1 \equiv \operatorname{diag}\left(\frac{1}{\tilde{d}_{11}}, \ldots, \frac{1}{\tilde{d}_{1m}}\right), \qquad \tilde{d}_{1j} \equiv \frac{D_0 d_{1j}}{D_0 + d_{1j}}\,. \tag{5.37b}$$

For the unit disk, $\mathcal{G}_N$ is evaluated using (B.1) of Appendix B, while (5.20) determines $\mathbf{H}$ and $\overline{H}_{\partial\Omega}$.

The result (5.37a) follows by first multiplying both sides of (5.36c) by $(I + D_0\mathcal{D}_1)^{-1}$ to get

$$\left(I + \frac{2\pi\nu}{D_0}\tilde{\mathcal{D}}_1^{-1}\mathcal{G}_N\right)\mathbf{p} = \frac{1}{D_0}\tilde{\mathcal{D}}_1^{-1}\left(\overline{U}\mathbf{e} - \mathcal{D}_{21}\mathbf{u}^1\right). \tag{5.38}$$

Then, upon using $(I + \nu\mathcal{A})^{-1} \approx I - \nu\mathcal{A}$ on the left side of (5.38) we obtain the two-term result (5.37a).

For the special case where there is no boundary loss, i.e. $\kappa = 0$, we can use the leading order approximation $\mathcal{C} = \tilde{\mathcal{D}}_1^{-1} + \mathcal{O}(\nu)$ in (5.37a), to obtain from (5.36a) and (5.36b) that

$$\overline{U}_t = -\gamma\overline{U} - \frac{2\pi}{|\Omega|}\sum_{j=1}^{m}\left(\tilde{d}_{1j}\overline{U} - \tilde{d}_{2j}u_{1j}\right); \quad \frac{d\mathbf{u}_j}{dt} = \mathbf{F}_j(\mathbf{u}_j) + 2\pi\mathbf{e}_1\left(\tilde{d}_{1j}\overline{U} - \tilde{d}_{2j}u_{1j}\right), \quad j = 1, \ldots, m, \tag{5.39a}$$

where $\tilde{d}_{1j} \equiv D_0 d_{1j}/(D_0 + d_{1j})$ and $\tilde{d}_{2j} \equiv D_0 d_{2j}/(D_0 + d_{1j})$. However, with this leading-order approximation, the effect of the spatial configuration of the cells is lost. The classical ODEs in the well-mixed regime $D_0 \to \infty$ are readily obtained after noting that $\tilde{d}_{1j} \to d_{1j}$ and $\tilde{d}_{2j} \to d_{2j}$ when $D_0 \to \infty$.

The ODE-DAE system (5.36), in which $\mathbf{p}$ is determined either by inverting the linear system in (5.36c) or by using the explicit approximation (5.37a), characterizes how the intracellular species are globally coupled through the spatial average of the bulk field. This system depends on the scaled diffusivity parameter D_0, it accounts for both sources of bulk degradation, and it includes the weak effect of the spatial configuration $\boldsymbol{x}_1, \ldots, \boldsymbol{x}_m$ of the cells through the Neumann Green's matrix $\mathcal{G}_N$. As a result, this ODE system can be used to study quorum-sensing behavior and the effect of varying the cell locations.

5.3. Comparison of the reduced ODE-DAE dynamics with ODE-PDE simulations. For the unit disk that contains a collection of identical cells, in this subsection we compare numerical solutions of the ODE system in (5.36) with corresponding FlexPDE [12] results computed from the cell-bulk model (1.3) with Lux kinetics (1.5). The ODE system was solved using the MATLAB [26] routine `ode45`. In the comparisons below, all initial conditions for the ODE-PDE system as well as the limiting ODE dynamics were set to zero unless otherwise stated. For the case where nonzero initial conditions were used, $\overline{U}(0)$ in the ODEs (5.36) was chosen as the spatial average of $U(\mathbf{x}, 0)$ for consistency.

We first consider a ring pattern of $m = 3$ cells with ring radius r_0, where the bulk parameters are

$$\varepsilon = 0.05, \quad D_0 = 1, \quad \gamma = 1, \quad \kappa = 0, \quad d_1 = 0.5, \quad d_2 = 0.5, \quad r_0 = 0.25. \tag{5.40}$$

In addition, the Lux ODE parameters are given in Table 1, with the following two exceptions:

$$\kappa_{DR} = 0.0125, \qquad \text{and} \qquad \kappa_{2A} = 5. \tag{5.41}$$

From (4.9) and (5.19), we calculate that $\kappa_{\text{ring}}(3) \approx 5.71$, so that only the upregulated steady-state exists. The nearest bifurcation point to κ_{eff} is at $\kappa_c \approx 6.17$, which is the fold point for the downregulated steady-state. In Fig. 5.4 the intracellular dynamics and the bulk average, as computed from the ODE system (5.36) both with and without the $\mathcal{O}(\nu)$ correction term, are seen to compare very favorably with the FlexPDE [12] results. These results confirm the predicted transition to the upregulated steady-state.

Next, we consider the effect of the spatial configuration of three cells, which arises in the ODEs (5.36) from the Neumann Green's matrix $\mathcal{G}_N$. In this example, we take the parameters as in (5.40), (5.41), and Table 1, while fixing the cell centers as $\mathbf{x}_1 = (0.5, 0)^T$, $\mathbf{x}_2 = (0.23, 0.67)^T$, and $\mathbf{x}_3 = (0.41, 0.3)^T$. In Fig. 5.5, we show a favorable comparison between the ODE and FlexPDE results for both the bulk average as well as the dynamics of the L^2-norm of $\mathbf{u}^1, \ldots, \mathbf{u}^4$, where $\mathbf{u}^i = (u_{i1}, u_{i2}, u_{i3})^T$. Although this figure shows that the

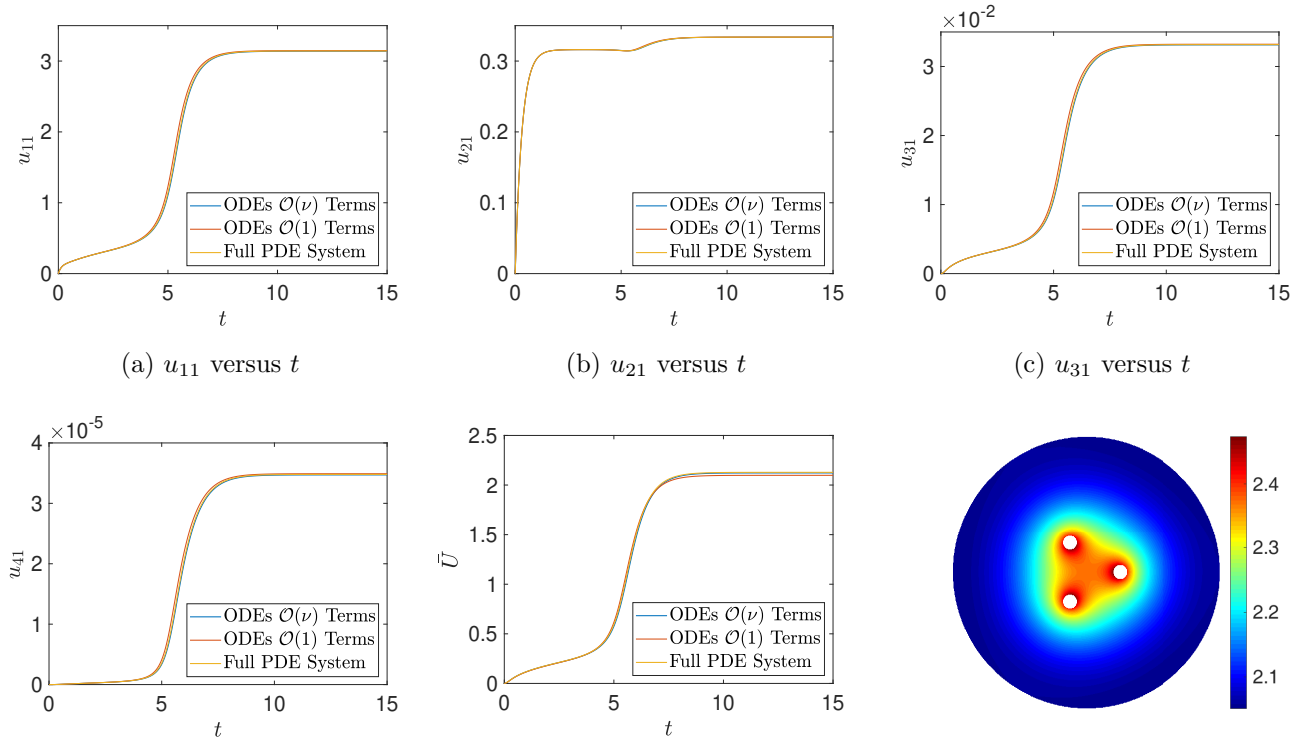

(a) u_{11} versus t (b) u_{21} versus t (c) u_{31} versus t

(d) u_{41} versus t (e) $\overline{U}$ versus t (f) Bulk solution

Figure 5.4: Comparison between the intracellular components and the bulk average, as computed from the ODE system (5.36), with and without the $\mathcal{O}(\nu)$ terms, and the FlexPDE [12] results computed from (1.3) and (1.5) for a ring pattern of three cells. The solution of the ODE-PDE model is nearly indistinguishable from both solutions of the ODEs, but there is better agreement when the $\mathcal{O}(\nu)$ terms are included. Due to symmetry, the solutions in the other two cells are identical. Parameter values in (5.40), (5.41), and Table 1.

cell locations do have an impact on the spatial profile of the bulk solution (bottom right panel of Fig. 5.5), for this example we observe that the effect of the cell locations on the intracellular dynamics or on the bulk average is not so significant. This is further evidenced by superimposing in Fig. 5.5 the corresponding leading-order ODE results for the ring pattern of Fig. 5.4.

Although not shown here, the ODE system (5.36) has been solved for a number of distinct arrangements of three cells. We remark that the $\mathcal{O}(\nu)$ terms in (5.36c) are more significant when the cells are placed closer together or near the domain boundary (respecting the assumption of well-separated cells). This behavior is due to the logarithmic singularity in the Neumann Green's function as well as the fact that cells near the domain boundary see an image cell centered at their inverse point to the disk.

Unfortunately, it is not computational practical to drastically increase the number of cells in the FlexPDE computations of the full cell-bulk model (1.3) and (1.5) owing to the large computation time required. In contrast, the limiting ODE system (5.36) can still be solved relatively quickly for much larger m. Our detailed validation of the ODE dynamics with FlexPDE results for small m suggests that the ODEs (5.36) would still give accurate results for the full cell-bulk model even as m increases.

For our next example, we use the ODEs (5.36) to study the effect of two distinct spatial arrangements of

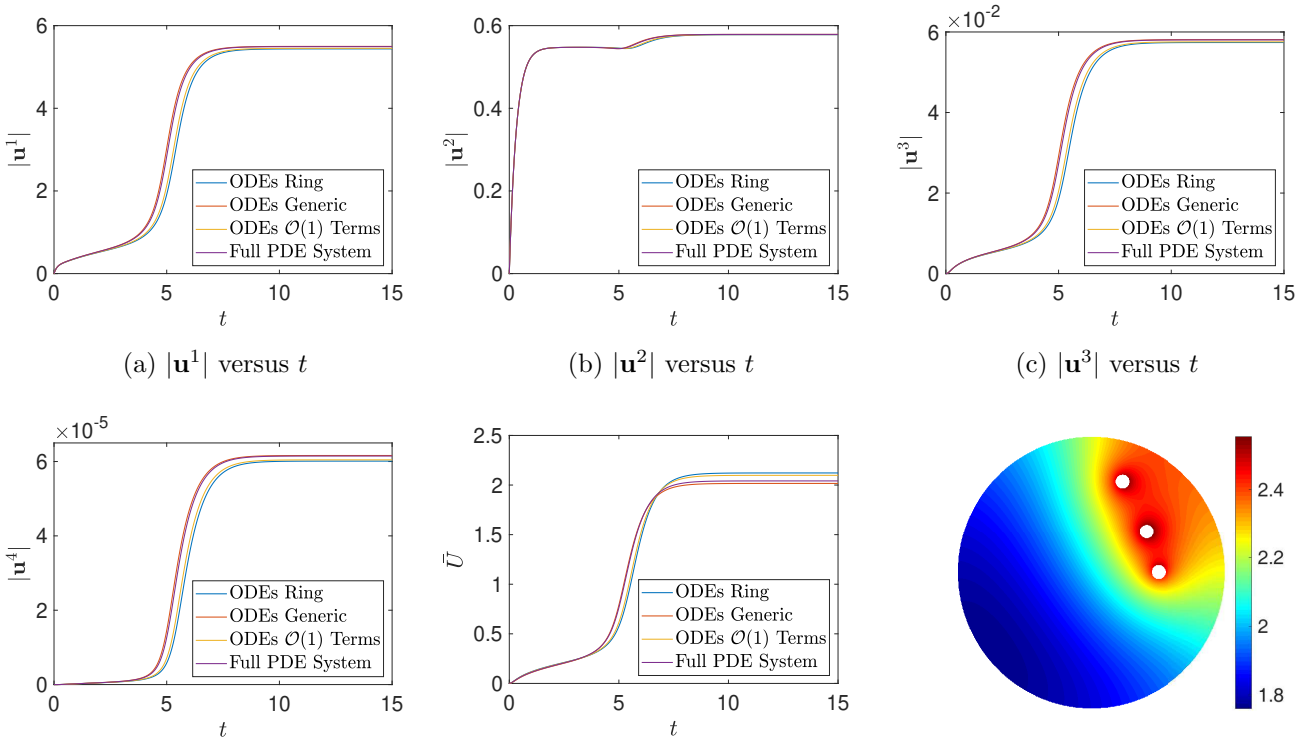

(a) $|\mathbf{u}^1|$ versus t (b) $|\mathbf{u}^2|$ versus t (c) $|\mathbf{u}^3|$ versus t

(d) $|\mathbf{u}^4|$ versus t (e) $\overline{U}$ versus t (f) Bulk solution

Figure 5.5: Comparison between the intracellular norms $|\mathbf{u}^k|$, for $k = 1, \ldots, 4$, and the bulk average $\overline{U}$, as computed from either the ODEs (5.36) or from the cell-bulk model (1.3) and (1.5) using FlexPDE [12]. ODE results for the generic pattern, with the cell centers $\mathbf{x}_1 = (0.5, 0)^T$, $\mathbf{x}_2 = (0.23, 0.67)^T$, and $\mathbf{x}_3 = (0.41, 0.3)^T$, are also compared with those for a ring pattern with ring radius $r_0 = 0.25$. Parameter values in (5.40), (5.41), and Table 1.

25 cells in the unit disk. In order to fit 25 well-separated cells in the unit disk, ε is decreased from our usual value of 0.05 to $\varepsilon = 10^{-3}$. The resulting decrease in ν, from roughly 0.33 to $\nu \approx 0.14$, is not substantial enough to preclude a significant effect from the spatial configuration of cells. The other parameters are chosen as in (5.40), (5.41), and Table 1. For the first configuration, the cell centers are selected from a uniform distribution over the entire unit disk, while for the second configuration the cell centers are chosen uniformly over only a half-disk (see the left and middle panels of Fig. 5.6). For both cell patterns, in Fig. 5.6 we plot the average bulk concentration versus time computed from the ODEs (5.36) where the $\mathcal{O}(\nu)$ spatial effects were included. The corresponding ODE result, where the $\mathcal{O}(\nu)$ terms is neglected, is shown in Fig. 5.6 to poorly approximate the bulk average for the second configuration where the cells are more clustered. This example suggests that for a *weakly-clustered* cell configuration, such as in the middle panel of Fig. 5.6, it is essential to include the Neumann Green's matrix in the ODEs (5.36).

Finally, we use the ODE dynamics (5.36) to illustrate the effect of the spatial configuration of cells on QS behavior. For this example, we first consider a ring pattern of cells with a ring radius $r_0 = 0.5$ and with $\kappa_{2A} = 5.9$, where the other parameters are as in (5.40), (5.41), and Table 1. With these parameters, solutions to the ODEs (5.36) are computed for $m = 9, 10, 11$ cells, with the results for the average bulk dynamics shown in Fig. 5.7. The theoretical criterion $\kappa_{\text{ring}} > \kappa_c$ from (4.9) and (5.19) predicts that a

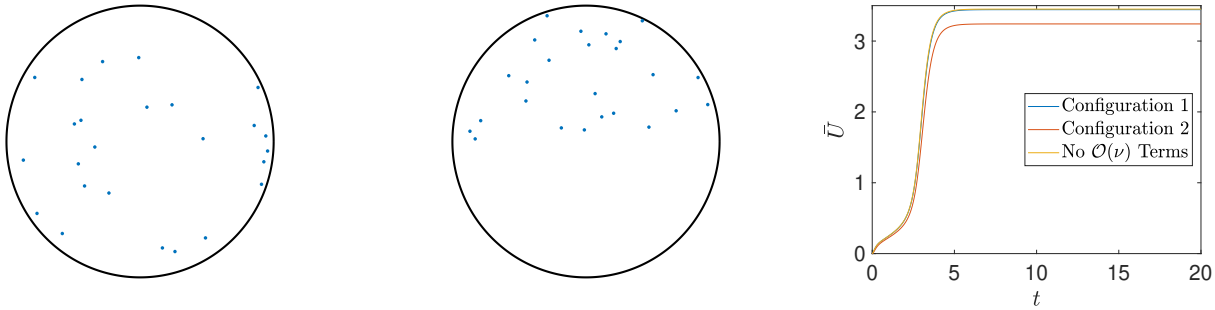

Figure 5.6: Numerical solution (right panel) for $\overline{U}$ from the ODE system (5.36), with and without neglecting $\mathcal{O}(\nu)$ terms, for two distinct 25-cell arrangements consisting of cell centers chosen from a uniform distribution over the entire disk (configuration 1, left) and the half-disk (configuration 2, middle). The cells are not drawn to scale so that they can be seen. Parameter values in (5.40), (5.41), and Table 1.

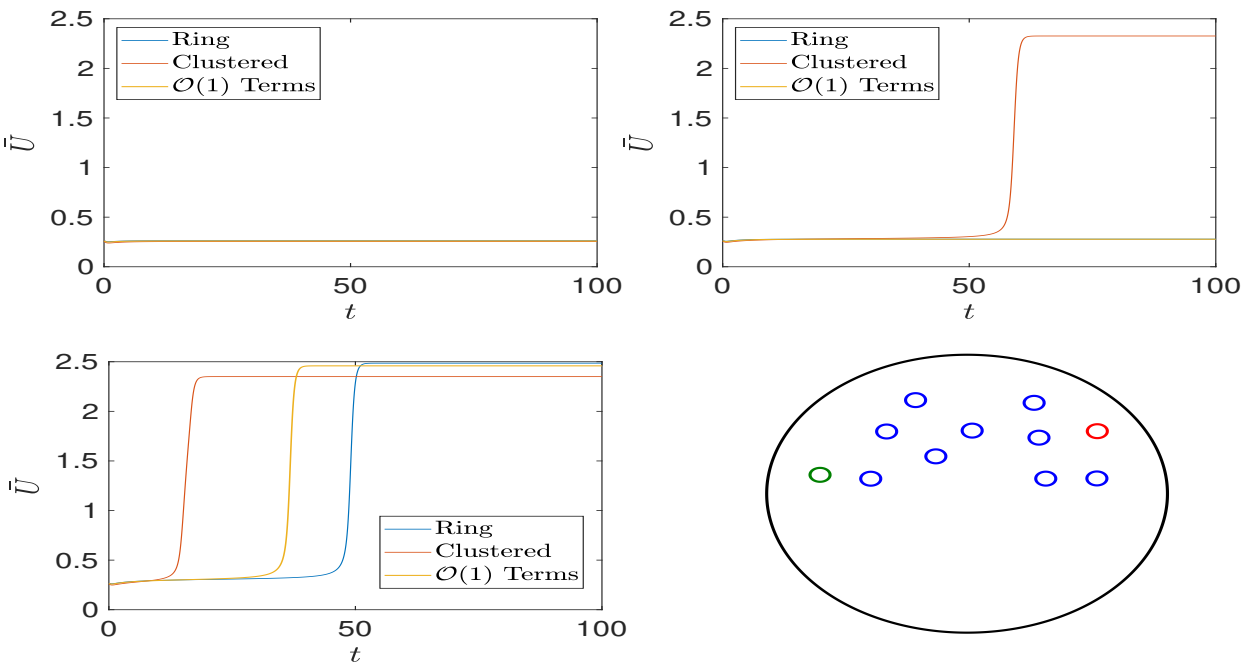

Figure 5.7: Numerical solution of the ODE system (5.36) illustrating QS behavior. The average bulk concentration is shown in the top left, top right, and bottom left panels for 9, 10, and 11 cells, respectively. The corresponding weakly clustered patterns are shown in the bottom right panel, where the cells marked in green and red are the respective 10th and 11th cells. The ring pattern achieves a quorum at 11 cells, while the weakly clustered pattern has a quorum at 10 cells. Parameter values in (5.40), (5.41), and Table 1.

quorum is reached at 11 cells. This predicted transition to an upregulated steady-state for $m = 11$ cells on a ring is confirmed from the ODE results shown in Fig. 5.7. In our computations, initial conditions for 9 cells were chosen to be close to the downregulated steady-state. The same initial conditions were chosen when $m = 10, 11$, with the extra cells having the same initial concentrations as the others.

For the generic non-ring cell pattern shown in the bottom right panel of Fig. 5.7, we observe that a quorum can be achieved at a slightly smaller population than predicted by the leading order criterion $\kappa_{\text{eff}} > \kappa_c$, based on using (5.17) in Principal Result 8. For the generic pattern, we use a configuration of 9 cells drawn from a uniform distribution over the upper half-disk. The 10th and 11th cells are added to this configuration as in the bottom right panel of Fig. 5.7. We use the same initial conditions and parameters as for the ring pattern, with the numerical results from the ODE system (5.36) shown in Fig. 5.7. Although the cells in the ring pattern are observed to transition to the upregulated state at 11 cells, as expected from the asymptotic theory, we observe from the top right panel of Fig. 5.7 that the weak-clustering of cells results in an early quorum at 10 cells. The solutions to the ODE system (5.36) without the $\mathcal{O}(\nu)$ effect of the cell configuration, is shown in Fig. 5.7 for comparison. We observe that the inclusion of these terms can cause the transition to be delayed or advanced by an $\mathcal{O}(1)$ time interval. In our ODE computations using (5.36), the solutions for $m = 9, 10$ cells were computed out to $t = 1000$ to ensure that all transitions to an upregulated steady-state would be detected.

6. Discussion. Based on the analysis of the cell-bulk ODE-PDE model (1.3)–(1.5), we developed a hybrid asymptotic-numerical theory in a 2-D bounded domain to predict QS transitions between bistable steady-states for a collection of bacterial cells with intracellular kinetics given by the LuxI/LuxR circuit of [27]. In this framework, the cell-cell communication is mediated by an autoinducer PDE diffuson field, where the AI molecule of interest is N-(3-oxohexanoyl)-homoserine lactone (cf. [28]). Moreover, experimentally measured cell permeabilities and reaction kinetic parameters based on biological experiments are readily incorporated into the model (cf. [27]). Our cell-bulk model provides a simplified, but analytically tractable, conceptual reformulation of the large-scale ODE model of [27] that employed a discretized bulk diffusion process, but which incorporated other factors such as cell division and inter-cell mechanical forces. Our asymptotic analysis of the cell-bulk system relied on modeling the bacterial cells as circular disks with a radius that is much smaller than the length-scale of the confining domain. Our analysis of QS behavior is distinct from that in [15] and [19] where a similar cell-bulk model was formulated, but with Sel'kov intracellular kinetics. For this latter model, the main focus was to analyze QS transitions due to a Hopf bifurcation that triggers the switch-like emergence of intracellular oscillations at a critical population density.

With a bulk degradation process, one of our main results is a set of criteria that characterize QS transitions between steady-states of the cell-bulk model, as summarized in Principal Results 6, 7, and 8. More specifically, when $D = \mathcal{O}(1)$, in Principal Result 6 we analyzed a ring pattern of cells in the unit disk, and obtained a criterion for QS transitions that is accurate to all orders of $\nu \equiv -1/\log\varepsilon$, where $\varepsilon << 1$ is the (dimensionless) cell radius. For an arbitrary cell pattern, a similar criterion accurate up to and including $\mathcal{O}(\nu^2)$ terms was derived in Principal Result 7, and was found to agree reasonably well with full numerical results. With bulk degradation, these results show analytically that the effect of coupling identical bacterial cells to the autoinducer diffusion field is to create an effective bifurcation parameter for κ_{2A}, the intracellular AI decay coefficient, that depends on the population of the colony, the bulk diffusivity, the membrane permeabilities, and the cell radius. The asymptotic theory predicts that QS transitions occur when this effective parameter passes through a saddle-node bifurcation point of the Lux ODE kinetics for an isolated cell. As such, the calculation of the critical population size for a QS transition for the full ODE-PDE cell-bulk model reduces to a simple algebraic computation of the effective bifurcation parameter and the saddle-node points in the Lux ODE system. This effective bifurcation parameter depends on all bulk parameters, and so changing any one of them can trigger a QS transition. For instance, varying the diffusion coefficient for a fixed population size can result in a QS transition, which we can interpret as diffusion sensing behavior. The dependence of this effective parameter on the population size for certain cell patterns in the unit disk was shown in Fig. 4.1 and Fig. 5.1, while its dependence on the bulk diffusivity for

a fixed population size was shown in Fig. 5.2.

For the $D = \mathcal{O}(1)$ parameter regime, we used a winding number argument to numerically implement the linear stability theory based on the GCEP (3.18). In addition, we developed a simple line-sweep method to detect unstable positive real eigenvalues of the GCEP that commonly occur in our cell-bulk model. With no bulk degradation, we showed that there are solution branches for a ring pattern of cells where only some of the cells are upregulated (see Fig. 4.2 and Fig. 4.5). However, most of these branches are unstable as was shown for a small number of cells. It remains an open problem to determine whether QS behavior can occur on these solution branches.

We conjectured that QS behavior in the cell-bulk model with Lux kinetics must be associated with a degradation process of AI in the bulk medium. Our analysis in §3 and computations in §4.4 suggest that this is not unique to the Lux system. Without any bulk loss terms, the main branch of steady-state solutions is completely uncoupled from the bulk medium and the cells behave as though they are isolated (see Fig. 4.2). Qualitatively, this result for the main steady-state branch can be interpreted as a balance between production and decay of AI. In an isolated cell, a steady-state is achieved when intracellular production and decay are balanced. The bulk coupling can be viewed as introducing additional AI degradation in the model, but only when loss terms are present. Therefore, without bulk loss, balance is achieved at the same intracellular concentrations as in the uncoupled system. The bulk loss terms may arise as either a bulk decay or a nonzero flux of AI, modeled by a Robin condition, through the domain boundary. It is sufficient to have only one of these factors present to observe QS behavior. In a scenario where the bulk decay rate is small, the effect of a non-reflecting boundary condition may be significant, which is consistent with previous experimental results (cf. [37, 25]). In summary, our analysis strongly suggests that the presence of bulk loss terms is a necessary ingredient for mathematical models of QS behavior that involve spatial coupling.

In the distinguished limit $D = D_0/\nu \gg 1$, we showed that solutions to the cell-bulk ODE-PDE model (1.3)–(1.5) can be approximated up to and including $\mathcal{O}(\nu)$ terms by the ODE-DAE system in (5.36). This reduced system includes the effect of cell locations in the $\mathcal{O}(\nu)$ terms. For a small number of cells, we showed that the solutions of the ODE-DAE system, as well as the criterion for QS transitions, agree very well with full FlexPDE simululations of (1.3)–(1.5) even when D is not that large (in our case $D \approx 3$). By using the ODE-DAE system, we investigated the role of cell location on QS behavior and showed that it can have a very significant effect near the critical population size for a QS transition. In particular, a *weak clustering* of cells can cause a quorum to be achieved at a smaller population. We also derived simplified QS criteria for branch transitions in which the critical population size can be estimated explicitly (to leading order) using the simple formula in (5.18). As a remark, by using Fig. 3 in [27], we estimate for the parameter set P1 in [27] that $\varepsilon \approx 0.05$ and $D \approx 6$, which lies is in the parameter regime for our simplified large D theory.

There are several directions for future work. For our specific cell-bulk model (1.3)–(1.5), in the $D = \mathcal{O}(\nu^{-1}) \gg 1$ regime it would be interesting to construct mixed-state equilibria, accurate to all orders in ν, in which only some fraction of the cells are in the upregulated state. Another open issue is to identify cell configurations $\{\boldsymbol{x}_1, \ldots, \boldsymbol{x}_m\}$ in Ω for which $\boldsymbol{e} = (1, \ldots, 1)^T$ is an eigenvector of the Green's matrix $\mathcal{G}$. Recall that for such a cell pattern the effective bifurcation parameter in Principal Result 6 characterizing QS transitions can be calculated to all orders in ν. A spatial configuration where the cells are centered at the lattice points of a 2-D Bravais lattice, and which is constrained to fit within Ω, is a candidate for such a symmetric cell pattern. As an extension to our model, it would be worthwhile to incorporate bacterial cell movement induced by chemical signaling gradients and mechanical forces and to model a cell division process, as was done in [27]. Within our theoretical framework, but allowing for circular bacterial cells of different radii, this can be done in a quasi-static limit by imposing a law of motion for the cell centers together with an ODE for an expanding cell radius that triggers a cell division process once the cell radius

exceeds a critical threshold. Finally, it would be worthwhile to extend our analysis to a 3-D setting. The challenge with the 3-D case is that owing to the fast $1/r$ decay of the autoinducer field away from the cells, the cell-cell communication will be weaker than in 2-D unless the bulk diffusivity is sufficiently large.

Appendices

A. Non-Dimensionalization. We non-dimensionalize the cell-bulk model (1.1) and (1.2) and the Lux ODE system of [27]. Our dimensional model assumes units of concentration for the extracellular AI and intracellular chemical species whereas the dimensional model in [15] uses both mass and concentration units. At the end of this appendix, we give the units for all of the quantities. In Table 1 we list the parameter values for parameter set P1 in [27], along with their dimensionless counterparts given in (A.3).

We begin by non-dimensionalizing the Lux ODE kinetics for an isolated cell. In dimensional quantities and without bulk coupling, the system given in [27] is

$$\begin{aligned} \frac{\mathrm{d}v_1}{\mathrm{d}T} &= c_1 + \frac{k_{1A}v_4}{k_{DA}+v_4} - k_{2A}v_1 - k_5 v_1 v_2 + k_6 v_3\,, \qquad & \frac{\mathrm{d}v_3}{\mathrm{d}T} &= k_5 v_1 v_2 - k_6 v_3 - 2k_3 v_3^2 + 2k_4 v_4\,, \\ \frac{\mathrm{d}v_2}{\mathrm{d}T} &= c_2 + \frac{k_{1R}v_4}{k_{DR}+v_4} - k_{2R}v_2 - k_5 v_1 v_2 + k_6 v_3\,, \qquad & \frac{\mathrm{d}v_4}{\mathrm{d}T} &= k_3 v_3^2 - k_4 v_4\,. \end{aligned} \tag{A.1}$$

In our non-dimensionalization we eliminate as many parameters as possible, while ensuring that the ODE dynamics reaches its steady-state on an $\mathcal{O}(1)$ timescale. To this end, and with $\mathbf{v} \equiv (v_1, \ldots, v_4)^T$, we introduce the non-dimensional variables $\mathbf{u}$ and t as

$$\mathbf{v} \equiv v_c \mathbf{u}\,, \qquad t \equiv k_R T\,, \qquad \text{where} \qquad v_c \equiv \sqrt{\frac{c_2}{k_5}}\,, \quad k_R \equiv \sqrt{k_5 c_2}\,. \tag{A.2}$$

This choice eliminates κ_5 and c_2. New dimensionless ODE parameters are then defined as

$$\begin{aligned} &\kappa_{1A} \equiv \frac{k_{1A}}{c_2}\,, \quad \kappa_{DA} \equiv k_{DA}\sqrt{\frac{k_5}{c_2}}\,, \quad \kappa_{2A} \equiv \frac{k_{2A}}{\sqrt{k_5 c_2}}\,, \quad \kappa_{1R} \equiv \frac{k_{1R}}{c_2}\,, \quad \kappa_{DR} \equiv k_{DR}\sqrt{\frac{k_5}{c_2}}\,, \\ &\kappa_{2R} \equiv \frac{k_{2R}}{\sqrt{k_5 c_2}}\,, \quad k_3 \equiv \frac{k_3}{k_5}\,, \quad \kappa_4 \equiv \frac{k_4}{\sqrt{k_5 c_2}}\,, \quad \kappa_5 \equiv \frac{k_6}{\sqrt{k_5 c_2}}\,, \quad c \equiv \frac{c_1}{c_2}\,. \end{aligned} \tag{A.3}$$

By using (A.2) and (A.3) in (A.1), we obtain the dimensionless system for the reaction kinetics in (1.5).

The full ODE-PDE system is made dimensionless in a slightly different way than in [15]. In (1.1) and (1.2) both $\mathcal{U}$ and $\mathbf{v}_j$ have units of concentration (moles/length^2), while in [15], $\mathbf{v}_j$ is measured in total amount (moles). With this in mind, we define the dimensionless quantities $\mathbf{x}$ and $U(\mathbf{x}, t)$ by $\mathbf{x} \equiv \mathbf{X}/L$ and $U \equiv \mathcal{U}/v_c$. Upon substituting this into (1.1), we readily obtain (1.3) after defining the dimensionless bulk constants D, γ, and κ and the dimensionless cell permeabilities d_{1j} and d_{2j} as

$$D \equiv \frac{D_B}{k_R L^2}\,, \quad \gamma \equiv \frac{\gamma_B}{k_R}\,, \quad \kappa \equiv \frac{\kappa_B}{k_R}\,, \quad p_{1j} \equiv L k_R \frac{d_{1j}}{\varepsilon}\,, \quad p_{2j} \equiv L k_R \frac{d_{2j}}{\varepsilon}\,. \tag{A.4}$$

The requirement for the ε-dependent scaling in the permeabilities is so that there is an $\mathcal{O}(1)$ effect of the coupling of the cells to the bulk. Moreover, if $\mathbf{X} \in \Omega_L$, where Ω_L has a characteristic length scale of L, then $\mathbf{x} \in \Omega_1 \equiv \Omega$. The dimensionless kinetics in (1.4) follows from the definitions in (A.2) and (A.4).

Dimensional Parameter	Value [27]	Dimensionless Parameter	Value
c_1	10^{-4}	c	1
c_2	10^{-4}	-	-
k_{1A}	0.002	κ_{1A}	20
k_{1R}	0.002	κ_{1R}	20
k_{2A}	0.01	κ_{2A}	$\sqrt{10}$
k_{2R}	0.01	κ_{2R}	$\sqrt{10}$
k_{DA}	$2 \cdot 10^{-7}$	κ_{DA}	$2 \cdot 10^{-11/2}$
k_{DR}	10^{-4}	κ_{DR}	$10^{-5/2}$
k_3	0.1	κ_3	1
k_4	0.1	κ_4	$10^{3/2}$
k_5	0.1	κ_5	$10^{3/2}$
k_6	0.1	-	-

Table 1: List of parameter values from the parameter set P1 in [27] along with the rescaled dimensionless parameters defined in (A.3).

Denoting $[x]$ to be the units of x, the units of the Lux and bulk parameters are as follows:

$$
\begin{aligned}
&[\mathcal{U}] = [\mathbf{v}_j] = [v_c] = \frac{\text{moles}}{\text{length}^2}\,, \quad [D_B] = \frac{\text{length}^2}{\text{time}}\,, \quad [\kappa_B] = [p_{1j}] = [p_{2j}] = \frac{\text{length}}{\text{time}}\,, \\
&[\gamma_B] = \frac{1}{\text{time}}\,, \quad [c_1] = [c_2] = [k_{1A}] = [k_{1R}] = \frac{\text{moles}}{\text{length}^2 \times \text{time}}\,, \quad [k_3] = [k_5] = \frac{\text{length}^2}{\text{moles} \times \text{time}}\,, \\
&[k_R] = [k_{2A}] = [k_{2R}] = [k_4] = [k_6] = \frac{1}{\text{length}^2 \times \text{time}}\,, \qquad [k_{DA}] = [k_{DR}] = \frac{\text{moles}}{\text{length}^2}\,.
\end{aligned}
\tag{A.5}
$$

B. Green's functions for the unit disk. To implement our steady-state and linear stability theory for the unit disk, two different Green's functions are required. The Neumann Green's function, satisfying, (3.5) is needed in §3 for the steady-state analysis with no bulk loss, and in §5 to analyze the large $D = \mathcal{O}(\nu^{-1})$ limiting regime. In the GCEP analysis in §3.2 for the $D = \mathcal{O}(1)$ regime, the eigenvalue-dependent Green's function G_λ satisfying (3.17) is required. Setting $\lambda = 0$ in (3.17) yields the reduced-wave Green's function in (3.11), which is required in §3 for the steady-state analysis with bulk degradation.

In the unit disk, the Neumann Green's function and its regular part are (see equation (4.3) of [23]):

$$
G_N(\mathbf{x};\mathbf{x}_i) = -\frac{1}{2\pi}\log|\mathbf{x}-\mathbf{x}_i| - \frac{1}{4\pi}\log\left(|\mathbf{x}|^2|\mathbf{x}_i|^2 + 1 - 2\mathbf{x}\cdot\mathbf{x}_i\right) + \frac{(|\mathbf{x}|^2 + |\mathbf{x}_i|^2)}{4\pi} - \frac{3}{8\pi}, \tag{B.1a}
$$

$$
R_{Ni} = -\frac{1}{2\pi}\log\left(1 - |\mathbf{x}_i|^2\right) + \frac{|\mathbf{x}_i|^2}{2\pi} - \frac{3}{8\pi}\,. \tag{B.1b}
$$

Next, by extending the analysis in Appendix A.1 of [4] to allow for a Robin boundary condition, the Green's

function G_λ and its regular part R_λ, satisfying (3.17), are calculated for the unit disk as

(B.2a)
$$G_\lambda(\mathbf{x};\mathbf{x}_i) = \frac{1}{2\pi}K_0(\theta_\lambda|\mathbf{x}-\mathbf{x}_i|) - \frac{1}{2\pi}\sum_{n=0}^{\infty}\sigma_n\left(\frac{\theta_\lambda K_n'(\theta_\lambda)+\frac{\kappa}{D}K_n(\theta_\lambda)}{\theta_\lambda I_n'(\theta_\lambda)+\frac{\kappa}{D}I_n(\theta_\lambda)}\right)I_n(\theta_\lambda|\mathbf{x}_i|)I_n(\theta_\lambda|\mathbf{x}|)\cos\left[n(\phi-\phi_i)\right] ,$$

(B.2b)
$$R_{\lambda i} = \frac{1}{2\pi}\left(\ln 2-\gamma_e-\log\theta_\lambda\right) - \frac{1}{2\pi}\sum_{n=0}^{\infty}\sigma_n\left(\frac{\theta_\lambda K_n'(\theta_\lambda)+\frac{\kappa}{D}K_n(\theta_\lambda)}{\theta_\lambda I_n'(\theta_\lambda)+\frac{\kappa}{D}I_n(\theta_\lambda)}\right)\left[I_n(\theta_\lambda|\mathbf{x}_i|)\right]^2 ,$$

where $\mathbf{x} = |\mathbf{x}|(\cos\phi,\sin\phi)^T$ and $\mathbf{x}_i = |\mathbf{x}_i|(\cos\phi_i,\sin\phi_i)^T$. Here $\sigma_0 \equiv 1$, $\sigma_n \equiv 2$ for $n \geq 2$, and $\gamma_e = 0.57721\ldots$ is the Euler-Mascheroni constant. The functions K_n and I_n are the nth-order modified Bessel functions of the first and second kind, respectively. Here, $\theta_\lambda \equiv \sqrt{(\gamma+\lambda)/D}$, where the principle branch of the square root is taken when the argument is complex. Setting $\lambda = 0$ in (B.2) yields the result for the reduced-wave Green's function and its regular part in (3.11).

When the centers $\mathbf{x}_k$, for $k = 1,\ldots,m$, of the cells are equally-spaced on a ring concentric within the unit disk, the Green's matrices $\mathcal{G}_N$, $\mathcal{G}$, and $\mathcal{G}_\lambda$ as needed in the steady-state and linear stability analysis in §3 are cyclic and symmetric matrices. As such, their matrix spectrum is available analytically.

For an $m \times m$ cyclic matrix $\mathcal{A}$, with possibly complex-valued matrix entries, its complex-valued eigenvectors $\tilde{\mathbf{v}}_j$ and eigenvalues α_j are $\alpha_j = \sum_{k=1}^{m}\mathcal{A}_{1k}\omega_j^{k-1}$ and $\tilde{\mathbf{v}}_j = \left(1,\omega_j,...,\omega_j^{m-1}\right)^T$, for $j = 1,\ldots,m$. Here $\omega_j \equiv \exp\left(\frac{2\pi i(j-1)}{m}\right)$ and $\mathcal{A}_{1k}$, for $k = 1,\ldots,m$, are the elements of the first row of $\mathcal{A}$. Since $\mathcal{A}$ is also a symmetric matrix, we have $\mathcal{A}_{1,j} = \mathcal{A}_{1,m+2-j}$, for $j = 2,\ldots,\lceil m/2\rceil$, where the ceiling function $\lceil x\rceil$ is defined as the smallest integer not less than x. Consequently, $\alpha_j = \alpha_{m+2-j}$, for $j = 2,\ldots,\lceil m/2\rceil$, so that there are $m-1$ eigenvalues with a multiplicity of two when m is odd, and $m-2$ such eigenvalues when m is even. As a result, it follows that $\frac{1}{2}\left[\tilde{\mathbf{v}}_j+\tilde{\mathbf{v}}_{m+2-j}\right]$ and $\frac{1}{2i}\left[\tilde{\mathbf{v}}_j-\tilde{\mathbf{v}}_{m+2-j}\right]$ are two independent real-valued eigenvectors of $\mathcal{A}$, corresponding to the eigenvalues of multiplicity two. In this way, the matrix spectrum of a cyclic and symmetric matrix $\mathcal{A}$, with the normalized eigenvectors $\mathbf{v}_j^T\mathbf{v}_j = 1$, is

(B.3)
$$\alpha_j = \sum_{k=1}^{m}\mathcal{A}_{1k}\cos\left(\theta_j(k-1)\right) , \quad j = 1,\ldots,m ; \qquad \theta_j \equiv \frac{2\pi(j-1)}{m} ; \qquad \mathbf{v}_1 = \frac{1}{\sqrt{m}}\mathbf{e} ,$$
$$\mathbf{v}_j = \sqrt{\frac{2}{m}}\left(1,\cos\left(\theta_j\right),\ldots,\cos\left(\theta_j(m-1)\right)\right)^T , \quad \mathbf{v}_{m+2-j} = \sqrt{\frac{2}{m}}\left(0,\sin\left(\theta_j\right),\ldots,\sin\left(\theta_j(m-1)\right)\right)^T ,$$

for $j = 2,\ldots,\lceil m/2\rceil$, where $\theta_j \equiv 2\pi(j-1)/m$. When m is even, there is an additional normalized eigenvector of multiplicity one given by $\mathbf{v}_{m/2+1} = m^{-1/2}(1,-1,1,\ldots,-1)^T$.

REFERENCES

[1] R. G. Abisado, S. Benomar, J. R. Klaus, A. A. Dandekar, and J. R. Chandler. Bacterial quorum sensing and microbial community interactions. *mBio*, 9(3):e02331–17, 2018.

[2] D. G. Alciatore and R. Miranda. A winding number and point-in-polygon algorithm. *Glaxo Virtual Anatomy Project Research Report, Department of Mechanical Engineering, Colorado State University*, 1995.

[3] T. Betcke, N. G. Highan, V. Mehrmann, C. Schröder, and T. F. NLEVP: A collection of nonlinear eigenvalue problems. *ACM Trans. Math. Software*, 39(2):7.1–7.28, 2013.

[4] W. Chen and M. J. Ward. The stability and dynamics of localized spot patterns in the two-dimensional Gray–Scott model. *SIAM J. Appl. Dyn. Syst.*, 10(2):582–666, 2011.

[5] S. Danø, M. F. Madsen, and P. G. Sørensen. Quantitative characterization of cell synchronization in yeast. *Proc. Natl. Acad. Sci.*, 104(31):12732–12736, 2007.

[6] S. Danø, P. G. Sørensen, and F. Hynne. Sustained oscillations in living cells. *Nature*, 402(6759):320–322, 1999.
[7] S. De Monte, F. d'Ovidio, S. Danø, and P. G. Sørensen. Dynamical quorum sensing: Population density encoded in cellular dynamics. *Proc. Natl. Acad. Sci.*, 104(47):18377–18381, 2007.
[8] A. Dhooge, W. Govaerts, Y. A. Kuznetsov, H. G. E. Meijer, and B. Sautois. New features of the software MatCont for bifurcation analysis of dynamical systems. *Math. Comput. Model. Dyn. Syst.*, 14(2):147–175, 2008.
[9] J. D. Dockery and J. P. Keener. A mathematical model for quorum sensing in *Pseudomonas aeruginosa*. *Bull. Math. Biol.*, 63(1):95–116, 2001.
[10] M. G. Fagerlind, S. A. Rice, P. Nilsson, M. Harlén, S. James, T. Charlton, and S. Kjelleberg. The role of regulators in the expression of quorum-sensing signals in *Pseudomonas aeruginosa*. *J. Mol. Microbiol. Biotechnol.*, 6(2):88–100, 2003.
[11] G. Fan and P. Bressloff. Modeling the role of feedback in the adaptive response of bacterial quorum sensing. *Bull. Math. Bio.*, 81(5):1479–1505, 2019.
[12] FlexPDE. *PDE Solutions inc*, 2015. Available at http://www.pdesolutions.com.
[13] W. C. Fuqua, S. C. Winans, and E. P. Greenberg. Quorum sensing in bacteria: the LuxR-LuxI family of cell density-responsive transcriptional regulators. *J. Bacteriol.*, 176(2):269–275, 1994.
[14] A. Goldbeter. *Biochemical Oscillations and Cellular Rhythms: The molecular bases of periodic and chaotic behaviour*. Cambridge Univ. Press, 1996.
[15] J. Gou and M. J. Ward. An asymptotic analysis of a 2-D model of dynamically active compartments coupled by bulk diffusion. *J. Nonlinear Sci.*, 26(4):979–1029, 2016.
[16] T. Gregor, K. Fujimoto, N. Masaki, and S. Sawai. The onset of collective behavior in social amoebae. *Science*, 328(5981):1021–1025, 2010.
[17] S. Güttel and F. Tisseur. The nonlinear eigenvalue problem. *Acta Numerica*, 26(1):1–94, 2017.
[18] S.-H. Hou. Classroom note: A simple proof of the Leverrier–Faddeev characteristic polynomial algorithm. *SIAM Rev.*, 40(3):706–709, 1998.
[19] S. Iyaniwura and M. J. Ward. Synchrony and oscillatory dynamics for a 2-D PDE-ODE model of diffusion-sensing with small signaling compartments. *submitted, SIAM J. Appl. Dyn. Sys., (40 pages)*, 2020.
[20] S. James, P. Nilsson, G. James, S. Kjelleberg, and T. Fagerström. Luminescence control in the marine bacterium *Vibrio fischeri*: An analysis of the dynamics of *lux* regulation. *J. Mol. Biol.*, 296(4):1127–1137, 2000.
[21] H. B. Kaplan and E. Greenberg. Diffusion of autoinducer is involved in regulation of the *Vibrio fischeri* luminescence system. *J. Bacteriol.*, 163(3):1210–1214, 1985.
[22] T. Kato. *Perturbation Theory for Linear Operators*, volume 132. Springer, Berlin, corrected printing of the second edition, 1995.
[23] T. Kolokolnikov, M. S. Titcombe, and M. J. Ward. Optimizing the fundamental Neumann eigenvalue for the Laplacian in a domain with small traps. *Eur. J. Appl. Math.*, 16(2):161–200, 2005.
[24] P. Mandel and T. Erneux. The slow passage through a steady bifurcation: Delay and memory effects. *J. Stat. Phys.*, 48(5-6):1059–1070, 1987.
[25] M. Marenda, M. Zanardo, A. Trovato, F. Seno, and A. Squartini. Modeling quorum sensing trade-offs between bacterial cell density and system extension from open boundaries. *Sci. Rep.*, 6:39142, 2016.
[26] The Mathworks, Inc., Natick, Massachusetts. *MATLAB version 9.4.0.813654 (R2018a)*, 2018.
[27] P. Melke, P. Sahlin, A. Levchenko, and H. Jönsson. A cell-based model for quorum sensing in heterogeneous bacterial colonies. *PLoS Comput. Biol.*, 6(6):e1000819, 2010.
[28] M. B. Miller and B. L. Bassler. Quorum sensing in bacteria. *Annu. Rev. Microbiol.*, 55(1):165–199, 2001.
[29] J. Müller, C. Kuttler, B. A. Hense, M. Rothballer, and A. Hartmann. Cell–cell communication by quorum sensing and dimension-reduction. *J. Math. Biol.*, 53(4):672–702, 2006.
[30] J. Müller and H. Uecker. Approximating the dynamics of communicating cells in a diffusive medium by ODEs homogenization with localization. *J. Math. Biol.*, 67(5):1023–1065, 2013.
[31] V. Nanjundiah. Cyclic AMP oscillations in *Dictyostelium discoideum*: models and observations. *Biophys. Chem.*, 72(1-2):1–8, 1998.
[32] K. H. Nealson, T. Platt, and J. W. Hastings. Cellular control of the synthesis and activity of the bacterial luminescent system. *J. Bacteriol.*, 104(1):313–322, 1970.
[33] K. Papenfort and B. L. Bassler. Quorum sensing signal–response systems in gram-negative bacteria. *Nat. Rev. Microbiol.*, 14(9):576–588, 2016.
[34] J. P. Pearson, C. Van Delden, and B. H. Iglewski. Active efflux and diffusion are involved in transport of *Pseudomonas aeruginosa* cell-to-cell signals. *J. Bacteriol.*, 181(4):1203–1210, 1999.
[35] J. Pérez-Velázquez, M. Gölgeli, and R. García-Contreras. Mathematical modelling of bacterial quorum sensing: A review. *Bull. Math. Biol.*, 78(8):1585–1639, 2016.
[36] W. Ridgway. Analysis of a 2D model of quorum sensing characterized by a transition from bistability in spatially coupled

signalling compartments. Master's thesis, The University of British Columbia, Vancouver, Canada, 2020.
[37] A. Trovato, F. Seno, M. Zanardo, S. Alberghini, A. Tondello, and A. Squartini. Quorum vs. diffusion sensing: a quantitative analysis of the relevance of absorbing or reflecting boundaries. *FEMS Microbiol. Lett.*, 352(2):198–203, 2014.
[38] C. Van Delden and B. H. Iglewski. Cell-to-cell signaling and *Pseudomonas aeruginosa* infections. *Emerg. Infect. Dis.*, 4(4):551–560, 1998.
[39] C. M. Waters and B. L. Bassler. Quorum sensing: Cell-to-cell communication in bacteria. *Annu. Rev. Cell Dev. Biol.*, 21:319–346, 2005.
[40] J. W. Williams, X. Cui, A. Levchenko, and A. M. Stevens. Robust and sensitive control of a quorum-sensing circuit by two interlocked feedback loops. *Mol. Syst. Biol.*, 4:234, 2008.